


Università degli Studi di Napoli Federico II
Ph.D. Program in
Information Technology and Electrical Engineering
XXXVI Cycle

Thesis for the Degree of Doctor of Philosophy

Engineering SERS-active substrates: design and characterization of advanced structures and innovative materials

by
Maria Alessandra Cutolo

Advisor: Prof. Giovanni Breglio

Co-advisor: Prof. Andrea Cusano, Prof. Marco Pisco

Scuola Politecnica e delle Scienze di Base
Dipartimento di Ingegneria Elettrica e delle Tecnologie dell'Informazione

To my mother.

Engineering SERS-active substrates: design and characterization of advanced structures and innovative materials

Ph.D. Thesis presented
for the fulfillment of the Degree of Doctor of Philosophy
in Information Technology and Electrical Engineering
by

Maria Alessandra Cutolo

October 2023

Approved as to style and content by

Prof. Giovanni Breglio, Advisor

Prof. Andrea Cusano, Prof. Marco Pisco, Co-advisor

Università degli Studi di Napoli Federico II

Ph.D. Program in Information Technology and Electrical Engineering
XXXVI cycle - Chairman: Prof. Stefano Russo

http://itee.dieti.unina.it

Candidate's declaration

I hereby declare that this thesis submitted to obtain the academic degree of Philosophiæ Doctor (Ph.D.) in Information Technology and Electrical Engineering is my own unaided work, that I have not used other than the sources indicated, and that all direct and indirect sources are acknowledged as references.
Parts of this dissertation is under submission in international journals.

Napoli, December 14, 2023

Maria Alessandra Cutolo

Abstract

In this thesis, I investigated the creation of SERS-active substrates by self-assembling hierarchical structures of plasmonic assisted nanospheres (HSNs). Since most SERS substrates are inherently planar, I demonstrate that a "hierarchical" approach could be systematically exploited to extend the SERS hotspots into the third dimension by improving the hot-spots spatial density and intensity. The proposed hierarchical architecture takes advantage of the classic ordered configuration of hexagonal closed packed array nanospheres (CPA). I used an additional layer of upper nanospheres to generate regular and intense hot spots pattern. I carried out a numerical analysis to predict SERS performance and to identify the most promising configurations, offering design criteria, an overview of the operating mechanisms and conditions that affect the SERS behavior of substrates. Two alternative methods of self-assembly were pursued to achieve gold-HSN, namely co-deposition and sequential deposition. Morphological analysis revealed the formation of well-ordered hierarchical structures with different ratios between bottom and upper nanosphere diameters. Experimental analysis of the SERS response shows that gold-HSN can function as economical SERS substrates with superior performance over CPA configurations. As an alternative approach, I also investigated the use of CMOS-compatible materials, as innovative SERS materials. Silver and gold are commonly preferred materials for plasmonic applications but they are not compatible with CMOS process. In this thesis, I investigated the use of titanium nitride and nickel germanide. After the experimental characterization of the refractive index of these materials, I carried out a numerical analysis to outlines their potential benefits and limitations. The performed preliminary analysis revealed that nickel germanide is a promising candidate for SERS active substrates.

Keywords: Hierarchical structures,SERS, self-assembly, nanolithography.

Sintesi in lingua italiana

In questa tesi ho studiato la creazione di substrati attivi SERS plasmonici auto-assemblati, a gerarchichia assistita da nanosfere (HSN). Poiché la maggior parte dei substrati SERS sono intrinsecamente planari, dimostro come un approccio "gerarchico" potrebbe essere sistematicamente sfruttato per estendere gli hotspot SERS nella terza dimensione, migliorandone la densità e l'intensità spaziale. L'architettura gerarchica proposta sfrutta i vantaggi della classica struttura ordinata di nanosfere chiusa esagonale (CPA). Con un ulteriore strato di nanosfere superiori ottengo un pattern di "hot spots" regolari e intensi. L'analisi numerica effettuata è mirata a prevedere le prestazioni SERS, le configurazioni più promettenti, criteri di progettazione, una panoramica dei meccanismi operativi e le condizioni che influenzano la risposta SERS dei substrati. Due metodi alternativi di auto-assemblaggio,co-deposizione e deposizione sequenziale, sono perseguiti per ottenere oro-HSN. L'analisi morfologica ha rivelato la formazione di strutture gerarchiche ben ordinate con rapporti diversi tra i diametri inferiori e superiori delle nanosfere. L'analisi sperimentale della risposta SERS mostra che l'oro-HSN può funzionare come substrato SERS economico con prestazioni superiori rispetto alle configurazioni CPA. Come approccio alternativo, ho anche studiato l'uso di materiali compatibili CMOS, come materiali SERS innovativi. Argento e oro sono materiali preferiti per le applicazioni plasmoniche, ma non sono compatibili con il processo CMOS. In questa tesi ho studiato l'uso di nitruro di titanio e nichel germanide. Dopo la caratterizzazione sperimentale dell'indice di rifrazione di questi materiali, ho effettuato un'analisi numerica per delinearne i potenziali benefici e limiti. L'analisi preliminare effettuata ha rivelato che il nichel germanide è un candidato promettente per i substrati attivi SERS.
Parole chiave: Nanostrutture gerarchiche, SERS, auto-assemblati, nanolitografia.

Acknowledgements

The research presented in this dissertation has been supported by the collaboration with the CNOS center (Nanophotonics and Optoelectronics Centre for Human Health, BN,Italy), Istituto di Scienze e Tecnologie Chimiche "G. Natta" (SCITEC, Consiglio Nazionale delle Ricerche CNR,Milan, Italy) and Optoelectronic Division Engineering Department, University of Sannio (Benevento, Italy).

The short term scientific research was spent to Ihp (Innovations for High Performance Microelectronics, Frankfurt Oder, Brandenburg, Germany), with the supervision of the Dr. Costanza Manganelli, for the period going from 01-06-2023 to 31-08-2023.

Contents

List of Acronyms

The following acronyms are used throughout the thesis.

AFM Atomic force microscope

SERS Surface-enhanced Raman scattering

TDM Therapeutic drug monitoring

RRMs Raman reporter molecules

CPA Closed packed array

CMOS Complementary metal-oxide semiconductor

BPT Biphenyl-4-thiol

EM Electromagnetic enhancement

EF Enhancement Factor

CE Chemical enhancemenCt

LSPP Localized surface plasmon polariton

LSPRs Localized surface plasmon resonances

THz Terahertz

PVD Physical vapor deposition

FIB Focused ion beam

EBL Electron beam lithography

UV Ultraviolet

NC Nanocubes

NP Nanoparticles

NSL Nanosphere lithography

4-ATP 4-aminothiophenol

R6G Rhodamine 6G

NA Numerical aperture

2PP Two-photon polymerization

HSN Hexagonal packed nano spheres

AVI Average volume integral

MVI Maximum volume integral

VI Volume integral

SEM Scanning electron microscopy

PI Peak intensity

IHP Leibniz Institute for High Performance Microelectronics

List of Figures

List of Tables

List of Symbols

The following symbols are used within the thesis

α	Molecular polarizability
Δ	The phase shift upon reflection
δ	Ratio between Upper spheres and Bottom spheres
ϵ	Permittivity
$\hat{n}$	normal vector
$\hbar$	Plank costant
λ	wavelenght
μ	Induced dipole moment
ν	Stimulation vibrational frequency
ω	Oscillation frequency
Ψ	The amplitude ratio upon reflection
ρ_r	BPT density
σ	Standard deviation

ϑ Angle of incidence

$\vec{G_0}$ Dyadic green function

A_{ex} The exposed area of the substrate

A_{light} The illuminated area of the substrate

A_{uc} The area of the unit cell

Ag Silver

Al_2O_3 Dialuminium trioxide

Au Gold

Cu_2O Copper(I) oxide or cuprous oxide

CuO Copper(II) oxide or cupric oxide

D Power density

D_B Bottom spheres diameter

D_U Upper spheres diameter

E Elettric field

E_0 Incident electric field

E_m Induced electric field

E_TOT Total electric field

E_{DR} Secondary field scattered

$EtOH$ Ethanol

F_{SERS} The ratio of the exposed area with the area of the unit

H_m Induced magnetic field

I_{Raman} Intensity of the Raman signal

I_{SERS} Intensity of the SERS signal

M_{loc} Radiation enhancement of the local field

M_{rad} Radiation enhancement

N_a Avogadro number

N_{Raman} The number of the molecule contributing to the Raman signal

N_{SERS} The number of the molecule contributing to the SERS signal

$N_{U/B}$ Ratio of the number of upper and bottom nanospheres

$NaOH$ Sodium hydroxide

P_{nr} Non-radiated power

P_{rad} Radiated power

P_{tot} The power of the total Raman-scattered radiation

s Separation between the spheres

t_g Thickness of gold layer

TiN Titanium Nitrides

TiO_2 Titanium dioxide or Titanium(IV) oxide

v_b Vibrational state

v_i Virtual states

$V_{U/B}$ Ratio of the volumes of the two solutions

Chapter 1

Introduction

Raman scattering or the Raman effect consists of the inelastic scattering of photons [11]. Typically, a beam of light that affects a sample passes through it unchanged or is absorbed. A small part of the incident beam is spread elastically, with the same frequency (Rayleigh effect). An even lower percentage of light undergoes an inelastic diffusion (Raman effect): that is, it is diffused with a higher or lower frequency than the original one. Since Raman scattering is 1% of the resulting scattering, amplifying the Raman signal would allow you to highlight characteristic peaks.The Surface-enhanced Raman scattering (SERS) is a phenomenon associated with the amplification of the Raman effect caused by the electromagnetic field present near a metallic nano structure, that is due to the plasmonic effect. The local electromagnetic field enhancement is mainly responsible for the Raman signal amplification, and the spatial regions with very intense field enhancement are commonly called as "hot spots". This analytical technique can therefore provide large amounts of structural molecular information on the chemical or biological target that comes into contact with the SERS surface, through the unique characteristics of the molecular fingerprint (SERS) spectrum back spread from the substrate. By suitably functionalizing the surface of these substrates it is possible to detect the presence of tumor markers or other target molecules, illuminating the substrate and analyzing the retro-diffused signal with a Raman spectrometer [12]. The SERS stands out as one of the most remarkably sensitive analytical methods available.

In certain instances, it can produce high-quality SERS spectra primarily derived from the presence of just a single molecule (as demonstrated by Kneipp et al [13]). Consequently, SERS spectroscopy has emerged as an extremely promising candidate for routine analytical procedures applied in medical, biochemical, environmental, and food analyses. Examples of possible application in medical and biological fields of SERS spectroscopy are:

- **Therapeutic drug monitoring (TDM):** is a crucial process that involves assessing the drug concentration in a biological matrix, typically plasma or serum, at a known time following administration. These concentrations are then interpreted in the context of relevant clinical parameters, including the target therapeutic range and the drug's pharmacokinetics (as explained by Jaworska et al. [14]). In TDM experiments, the straightforward approach involves examining the recorded SERS spectra of bodily fluids, such as urine, blood, or blood plasma, containing the drug of interest. The intensity of spectral bands associated with the drug is monitored, (as demonstrated by Markina et al. [15]).

- **Nanosensors:** are an alternative and highly effective application of SERS, containing Raman reporter molecules (RRMs). These RRMs are typically organic dyes with exceptional Raman scattering capabilities, such as rhodamine 6G or malachite green. Instead of relying on the Raman signal of the target substance itself, which can often have a much weaker signal, these RRMs are combined directly with the substance to be detected. This approach significantly enhances sensitivity [16].

- **Cancer diagnosis:** have emerged as SERS application, basing on the detecting via molecular vibrational fingerprints. SERS measurement on blood samples is most commonly used in early cancer detection, due to its high sensitivity,specificity and the ability to detect the compositional differences in biomaterials. Shilian Dong et. al. [17] presented a method for early cancer detection that uses label-free SERS spectroscopy, combined with machine learning.

In recent decades, several SERS nanostructures with controlled size, shape, composition, and arrangement have been proposed as SERS active substrates in the literature. The SERS nanostructures are strictly correlated to the manufacturing method. The SERS design deals with the aim to improve the performance by optimizing the hot spost generation and to guaratee the uniformity, reproducibility and cost-effectiveness. The reproducibility is the ability to obtain consistent results when using SERS-active substrates. Inconsistent or unpredictable SERS results can arise due to variations in the manufacturing process of the current substrates, the presence of impurities or/and defects or/and agglomerates, or the uncontrollable generation of "hot spots" in specific region of the substrate with exceptionally and extremely high Raman signal enhancement. Without reproducibility, it is difficult and not trustworthy to use SERS substrates for quantitative measurements, leading to inaccurate or unreliable data. Uniformity in SERS substrates refers to the consistent distribution of "hot spots" across the substrate's surface. Signal enhancement may be strong in certain areas of a non-uniform substrate, while other areas may have weaker or no enhancement at all. Lack of uniformity can lead to inconsistencies in data collection and prevent SERS from being a reliable tool for quantitative analysis. Optimizing hot spots is a key goal in SERS because it allows for more sensitive and precise Raman measurements. Different approaches and strategies for hot spot optimization are avaible:

- **Nanostructure Design:** the SERS substrate's nanostructures require a physical design that is crucial. It is possible to optimize the size, shape, and arrangement structures to maximize the enhancement effect. For example, sharp-edged nanoparticles, pointed structures, nanogaps, or hierarchical structures are often used to create intense and dense hot spots location.

- **Plasmonic materials:** the choice of plasmonic materials significantly influences hot spot optimization and consequently the performance of the advanced substrate. Noble metals (i.e. gold and silver) are commonly used because theier strong plasmonic properties and low electronic losses in the visible. Tinkering with the shape, size of nanoparticles and the symmetry of the final array can further refine and improve the location, intensity and density of the hot spots.

- **Nanofabrication techniques:** Advanced nanofabrication methods, such as electron beam lithography, nanoimprint lithography, or chemical etching, can be used to precisely obtain SERS nanostructure. The choice of fabrication can be impactful on the determination of the shape of the nanoparticles that form arrays and how they are arranged. The cost and time of fabrication are two aspects that should not be underestimated if you want to carry out research and/or mass fabrication

Over the years, countless advances have been made in the field of nanomanufacturing SERS substrates. It has gone from the creation of single structures with simple geometries to complex structures with double periodicity; such as periodically ordered nanocubes or nanorods covered with nanospheres [18]. Using electron beam and focused ion beam lithography, many SERS-active substrates have been produced. The fabrication of various regular geometries with high spatial resolution can be done using either technique [19]. Despite their significant advantages in accuracy and uniformity of hot-spots, these fabrication techniques are extremely expensive, making them not worth using for mass production. A low-cost production process can produce large and regular nanostructure patterns through bottom-up self-assembly techniques, which is an interesting alternative. Numerous self-assembly approaches have been successfully employed to create well-ordered SERS active substrates [20] [21] . Unlike nanostructures are widely diffused, very little progress has been made on substrates made on the fibre optic tip, in fact there are far fewer references in the literature. There are techniques that employ the use of femto-second lasers with which you can do a grating [22], or create nanopillar via interference lithography [23]. Nanosphere lithography made possible to obtain substrates consisting of an ordered pattern of nanospheres with a high reproducibility, sensitivity [24]. It is a self-assembly technique that compared to the others is low cost and allows direct fabrication on the tip of a fiber optic. This type of manufacturing also allows manufacturing on multiple optical fibers at the same time, drastically reducing both (already low) costs and manufacturing time [25].

The objective of this doctoral thesis was the design and characterization of a SERS substrate, identifying the substrate with the best performance. In particular to realize a substrate through the self-assembly technique (cost-effective, ability to perform uniform substrate), working on the geometry optimization (to create dense and intense hot spot) and to investigate alternative innovative materials. A versatile, adaptable, reproducible substrate with the peculiarity of having a dense spatial distribution (and high in number) of hot spots, consequently a high Enhancement Factor with accessibility and stability, is the objective of this work. In this way, the basic aim is to over come the limits imposed by the classical configuration of the closed packed array SERS substrate (CPA). In fact in the CPA, the hot spots are not accessible to the target molecule and the efficiency is strictly connected to the dimension of the target molecules. In thieir work Manago et al. demostrated [26] that the molecular target size plays a major role in the intensity of the Raman spectrum, by comparing the response of different substrate (including CPA) with different target molecules (Bovine Serum Albumin, BiPhenylThiol and Red blood cells). In this thesis's work will be explored the performance capabilities of a hierarchical nanospheres substrate coated with gold (the most commonly used and the best low-losses material [27]) Specifically, the substrate under analysis is a hierarchical array with hexagonal symmetry of nano spheres consisting of a first layer of spheres and a second layer of small spheres, placed in interstitial sites formed by bottom nano spheres. The spheres are made of polystyrene and covered with a layer of gold. First, an accurate numerical analysis was carried out, varying the diameter in the upper and lower nanospheres. Once the best performing structures were identified, they were manufactured using two different manufacturing techniques: co-deposition and sequential deposition. The first technique allows the substrates to be manufactured in a single step, but it has some constraint on the geometric dimension of the upper spheres. The second technique is two-phase but allows to realize all the structures without limits on geometry. Once the structures were manufactured, they were characterized both from the morphological point of view (in order to verify the geometry) and from the SERS point of view. For the SERS characterization, intensity signals, intensity maps (to highlight the possible homogeneity of hot spots) were acquired and the enhancement factor was calculated.

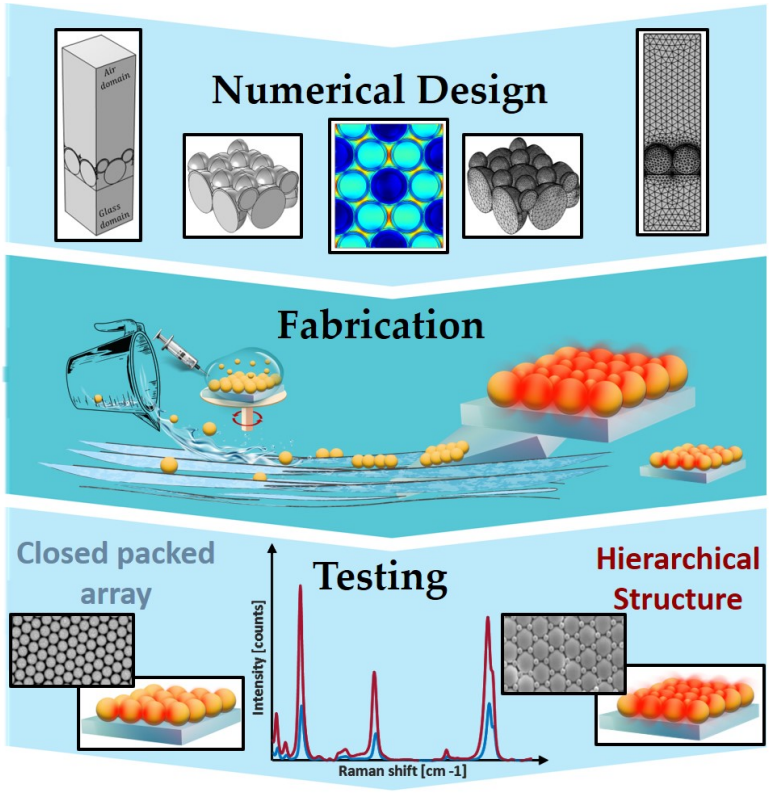

Figure 1.1. Workflow of the PhD project

SERS tests were performed using Biphenyl-4-thiol, which forms a fairly homogeneous layer on the substrate surface. The thesis work was divided following the schematic graphic abstract illustrated in figure 1.1. Simultaneously, the study focused on creating a versatile substrate. Using self-assembly technique, ordered and cost-effective substrates could be manufactured, both on a supporting glass (for planar application as microfluidics [28]) and on optical fiber tips (for examples for implantable biophotonic devices[29]). On the other side the possibility to combine the benefits of CMOS technology with the enhanced analytical capabilities of SERS could open the door to high-precision, high-resolution and mass

fabrication. Unfortunately, the metal (as gold,silver) are not CMOS compatible material. Extensive efforts by researchers have been were made to optimize the optical properties of nitrides, silicides, and germanides to produce materials with low loss. Under this consideration, a study on the capabilities offered by Titanium Nitride and Nickel Germanide, using the same substrate optimized for gold were exploited. The chapter 2 deals briefly with the theory behind the Raman and SERS phenomenon. Below, the chapter 3 deals with the current state of the art of SERS planar substrates (first paragraph) and substrates made directly on the tip of the fiber optic (second paragraph). The chapter 4 deals with the numerical analysis carried out, in particular it has been divided into two parts. The first paragraph deals with the methodology used and the specifications used to carry out the simulations, while the second with the results obtained. The chapter 5 describes the methodology used to manufacture the substrates (chosen following the numerical analysis), to characterize them (from the morphological point of view) and the morphological results. The chapter 6 deals with the SERS characterization, divided in two part: the methodology and the results carried out. The chapter 7 relies on the examination of plasmonic materials that differ from gold, as Titanium Nitride and Nickel Germanide. The two material are simulated using the refractive index (experimentally acquired) and characterized. The choice of the material relies on the possibility to use the CMOS-fabrication technique to realize a a SERS active substrate CMOS compatible for the lab on chip application field. The last chapter 8 deals with conclusions.

Chapter 2

Surfaced enhanced Raman scattering: briefly theory description

"Look at the resplendent colours on the soap bubbles! Why is the sea blue? What makes diamond glitter? Ask the right questions, and nature will open the doors to her secrets."

C.V.Raman

In physics, the scattering phenomenon can be distinguished into two major types, elastic and inelastic. Keeping in mind the kinetic theory of the collision of solid bodies, elastic scattering involves a loss (or gain) of very small energy of the incident electromagnetic radiation. This type of scattering is called Rayleigh scattering and contains no information about the structure of the molecule's vibrational states. On the other hand, inelastic scattering induces a variation in the energy, which lead a shift in the radiation frequency, due to iteration with molecular vibrational states (or modes). Raman scattering is the phenomenon of inelastic scattering of photons with matter [12]. Raman-based spectroscopy is a powerful analytical technique that allows information to be derived from complex molecular structures. This phenomenon is characterized by low cross-sectional dispersion resulting in extremely low signal intensity.

In fact, only one photon in 10^7 undergoes Raman scattering [30]. At the same time, the fluorescence phenomenon can even obscure the emitted Raman signal. These factors have limited the use and applications of conventional Raman spectroscopy over time. In 1973, Martin Fleischman discovered Surface enhanced Raman spectroscopy (SERS) [31], revealing the scientific community's interest in Raman spectroscopy. The Surface enhanced Raman spectroscopy consists in the amplification of the Raman effect coming from molecules, about different orders of magnitude [30]. This chapter aims to understand the basic theory of Raman and SERS scattering .

2.1 Raman scattering

Raman scattering is one of the main pillars of molecular spectroscopy. In 1923, the Indian physicist Chandrasekhara Venkata Raman (to whom the phenomenon owes its name) first discovered the Raman effect, influenced by the work filed by Lord Rayleigh in 1871 [32]. The phenomena has been extensively analyzed and used in different fields of physics (e.g. chemistry, biomedical, materials science, solid physics).In 1930 Raman received the Nobel Prize in Physics following this discovery. He observed that a part of the radiation, spread by some materials, manifested a different energy respect the incident, realizing that this radiation was mainly due to the chemical-physical characteristics of the material analyzed. The Raman effect consists in the inelastic diffusion of the electromagnetic radiation incident on a sample [33]. Raman scattering is a type of secondary radiation. Thanks to Raman spectroscopy it is possible to acquire information about not only the basic structure of the sample (e.g. structural changes, morphological defects, impurities) but also about the chemical composition (e.g. the functional groups present). The Raman signal is unique and represents the fingerprint of a molecule. Some of the fundamental characteristics of this spectroscopic technique are the ability to be non-destructive, non-invasive and at least allows to use even small volumes of the sample (about 1 μm^3) [34]. The phenomenon of Raman scattering, from the classical point of view, provides that when an electric field is applied on a molecule, the incident field will disturb the distribution of the

charge in the molecule, inducing a moment of dipole. The sum of induced dipole moments behaves like a macroscopic polarization, which generates a secondary electric field radiated by molecules. A quantitative and classic description of the matter-field interaction allow to understand how this interaction reveals structural information of the sample. The formula for the induced dipole moment μ, can be written as:

$$\mu = \alpha E \tag{2.1}$$

Where μ is the molecular dipole induced by the incident electric field E (characterized by its amplitude E_0 and its oscillation frequency $\omega = 2\pi\nu$. The incident electric field can be expressed as:

$$E = E_0 cos(2\pi\nu t) \tag{2.2}$$

The term α is the molecular polarizability, represents the proportionality factor between the incident field and the induced dipole moment. It measures how much the incident field is able to disturb the electron density. However, the polarization of a molecule is not a static quantity and can be modulated by the rotations and vibrations of the bond. The variation of polarization due to molecular vibration (i.e. displacement from the equilibrium position) can be expressed as follow:

$$\alpha = \alpha_0 + (r - r_0)\frac{\partial \alpha}{\partial r} \tag{2.3}$$

Here respectively r_0 and r are the bond lengths in equilibrium position and in perturbed position, the polarizability to equilibrium is α_0. The displacement can be represented as simple harmonic, that is:

$$r - r_0 = r_{max} cos(2\pi\nu_i t) \tag{2.4}$$

Where r_{max} is the maximum displacement of the atoms of the molecule from the equilibrium position and ν_i is the vibrational frequency. By replacing the equation 2.4 into the polarizability equation 2.3, gives:

$$\alpha = \alpha_0 + \frac{\partial \alpha}{\partial r} r_{max} cos(2\pi\nu_i t) \tag{2.5}$$

Considering the newly obtained expression for polarizzability (2.5) and replacing it in the dipole equation (2.1), gives:

$$\mu = \alpha_0 E_0 cos(2\pi\nu t) + E_0 r_{max} \frac{\partial \alpha}{\partial r} cos(2\pi\nu_i t) cos(2\pi\nu t) \tag{2.6}$$

Through the properties of cosine , is obtained:

$$\begin{aligned} \mu = & \underbrace{\alpha_0 E_0 + cos(2\pi\nu t)}_{\text{Rayleigh scattering}} + \\ & + \underbrace{\frac{E_0}{2} r_{max} \frac{\partial \alpha}{\partial r} cos[2\pi(\nu - \nu_i)t]}_{\text{Stokes scattering}} + \\ & + \underbrace{\frac{E_0}{2} r_{max} \frac{\partial \alpha}{\partial r} cos[2\pi(\nu + \nu_i)t]}_{\text{Anti Stokes scattering}} \end{aligned} \tag{2.7}$$

In the above equation 2.7 the first term is Rayleigh scattering and occurs when the frequency is equal to the stimulation frequency ν. Responsible for elastic scattered light, Rayleigh scattering does not contain any information on the molecular structure. Respectively, the second and last term are Stokes $\nu - \nu_i$ and Anti-Stokes $\nu + \nu_i$ scattering (occurring at a frequency below or above excitation). In the Stokes scattering, in relation to the excitation frequency, the radiation emitted by the induced dipole moment is red-shifted. This term contains information about the molecular structure and its dependence on frequency, represents the inelastic diffusion of light. The Raman spectrum is usually represented as Stokes scattering. Likewise Stokes scattering, the Anti-Stokes scattering is inelastic and involves a blue-shift, with respect to the excitation frequency. Unlike Stokes scattering, it has a very low intensity (due to the Boltzmann factor describing the population of thermally excited vibrational states). In terms of energy, most radiation has the same energy as incident photons (Rayleigh scattering), while a significantly small fraction has more or less energy than incident photons (Raman scattering). The reason why Raman scattering represents 1% of the resulting scattering. Additionally, the quantum mechanics approach offers the possibility to deeply understand the Raman scattering phenomena, compered to others phenomena like flu-

orescence. In quantum mechanics is possible to describe the interactions between photons and molecules with quantified energy levels [35]. When a monochromatic radiation with stimulation frequency ν interacts with a molecule, it makes an upright transition from the ground state (E_0) to an higher excited state (E_j). According to the energy conservation law:

$$\hbar\nu + E_0 = E_j + \hbar\nu_j \tag{2.8}$$

Ultimately:

$$\Delta E = \hbar(\nu - \nu_j) \tag{2.9}$$

In the Raman scattering, the energy is transferred or held from the molecule, due to the interaction between light and matter. In fluorescence phenomena, due to light absorption, the promotion of the electron to higher energy state is timely long enough to enable the molecule geometry to relax and adapt to the new electronic configuration. However, some energy is lost due to this internal conversion. When the fluorescence lifetime is terminated the molecule descends to the ground state. The fluorescence energy is lower than the excitation energy, as a consequence of this process. The substantial difference between fluorescence and absorption phenomena with Raman scattering rely on the fact that the latter are not based on electronic transitions. For Raman scattering, the absorption of light promotes the electron to a virtual excitation state (which is an intermediate state) instead of energy state. These virtual states (V_i) occur when the excitation energy is not sufficient to promote the molecule to a higher energy level. However, the energy absorbed by the molecule is transformed into a moment of induced dipole and dissipated through scattering. In terms of lifetime, fluorescence hovers around 10^{-9} to 10^{-7} seconds, while Raman scatters around 10^{-13} to 10^{-11} seconds [36]. In figure 2.1 is shown the schematic energy level diagram for Raman scattering and fluorescence. In the Rayleigh scattering, the energy provided to the molecule leading an upright transition. The same energy is emitted, according to equation 2.9 occurs that $\Delta E = 0$ (i.e $\nu = \nu_i$). Similarly, during the process of Stokes scattering, the promotion of the molecule is towards a higher virtual state. Nevertheless, the molecule does not return to the ground state, but decays to a vibrational state (V_b) emitting a photon (red-shifted respect incident light).

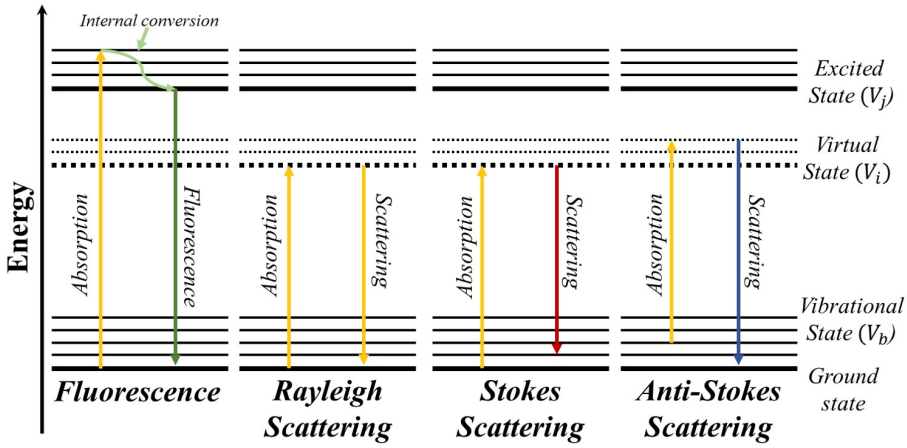

Figure 2.1. Schematic energy level diagram for fluorescence, Rayleigh scattering, Stokes Raman scattering and anti-Stokes Raman scattering

Resulting from vibrational and rotation movement, this vibrational state (V_b) is close to the ground state and the energy difference is pretty low. Studying the red shift of Raman spectrum is possible to characterize the vibrational movement of a molecule. Keeping in mind the equation 2.9 results in $\Delta E < 0$ (i.e $\nu > \nu_i$). In the anti-Stokes Raman scattering, some molecules may already be in a state of excited virtual energy, due to bonding movements. When the incident light is spread over the molecule, it is excited to a higher virtual state (V_i). In this case, at the end of the process a photon is emitted with a blue shift respect to the incident light. The probability that a molecule is in an already excited state, at ambient temperature, is extremely low. This is the reason why this type of scattering occurs much less frequently and with a pretty reduced intensity than Stokes Raman scattering. Considering the equation 2.9, the phenomena results in $\Delta E > 0$ (i.e $\nu < \nu_i$).The term $\nu - \nu_i = \Delta\nu$ is also refereed as Raman shift(commonly reported in wave-numbers) and is directly related to energy. To have a correlation between the wave-numbers shifts in the Raman spectrum and the spectral wavelengths, the following formula can be used:

$$\Delta\nu = \left(\frac{1}{\lambda_0} - \frac{1}{\lambda_i}\right) \tag{2.10}$$

Where λ_0 is the excitation wavelength and λ_i is the Raman wavelength. Thanks to quantum theory, it is possible to explain why the reduced intensity of anti Stokes scattering, not foreseen in classical theory [37].Generally the Raman signal has low intensities, reason why it is difficult to work with low concentrations and small amounts of samples. Accordingly to:

$$I_{Raman} \propto \alpha^2 E^2 \tag{2.11}$$

The Raman intensity is directly proportional to the second power of the polarization (α) and the second power of incident electromagnetic field (E) [38]. The intensity of the Raman signal should enhance, by increasing the incident electromagnetic field and so the efficiency of the polarization. This enhancement leads to the possibility of using small quantities of sample and detect the presence in low concentrations.

2.2 Surface Enhanced Raman Scattering

The Surfaced enhanced Raman scattering (SERS) is an analytical technique based on the amplification of the Raman signal, thanks to the iteration with a metal surface. The SERS has a higher sensitivity than the Raman scattering, allowing to analyze molecules at low concentration and with the decreasing of the fluorescence phenomenon. The nature of the enhancement mechanism is warmly debated, although SERS is a very active field of study [39]. In particular, two mechanisms have been accepted by the scientific community, namely the theory of electromagnetic enhancement (EM) and the theory of chemical enhancement (CE) [40]. Both of these enhancement act simultaneously. The theory of chemical enhancement contributes only to an enhancement of two or three orders of magnitude. The EC is due to chemical iteration that modifies polarization by interaction between metal and material molecules [41]. These enhanced electromagnetic fields are due to the coupling between the incident field and the localized surface plasmon polariton (LSPP) and derive from roughness characteristics . On the other hand, EM is the main source of enhancement, treating the molecule as a point dipole that interacts with the electromagnetic fields that form locally on the metal surface [42]. When electromagnetic radiation affects a rough metal surface (with

negative imaginary dielectric constant), the field near metal surfaces is strongly enhanced around nanoparticles through the generation of surface plasmons (as shown in fig. 2.2)[43]. There are two types of surface plasmon:

- Surface plasmon polariton: is a surface non-radiating electromagnetic wave that propagates in a direction parallel to the dielectric-metal interface. The wave finding itself confined between the dielectric and the metal, makes the oscillations are very sensitive to any change, such as the adsorption of molecules [44].

- Localized surface plasmon resonances (LSPRs) are collective oscillations of the charge of free electrons in metallic nanoparticles that are excited by light. They show a larger field amplitude near the resonance wavelength. The field is highly localized near the nanoparticles and decays rapidly away from the dielectric-metal interface [45].

The SERS signal benefits from this high electromagnetic field generated by LSPRs, enhancing the Raman signal. The EM enhancing mechanism can be described as a two steps process: the local field enhancement and the radiation enhancement.

Local field enhancement

The Raman intensity is proportional to the induced dipole, according the equation 2.1. Keeping in mind the equation 2.1, the free oscillating induced dipole moment can be wrote as the product between the incident field (E_0) and the polarization (α), considering the position r_m, as follow:

$$p_m(\omega_i, r_m) = \alpha_m(\omega_i, \omega_0) E_0(\omega_0, r_m) \tag{2.12}$$

The equation (2.12) express the modulation of the incident field (E_0) at the frequency ω_0, yielding the Raman scattering at frequency ω_i. The induced dipole irradiates in near field, locally and, into far field. At position R, the electromagnetic field is equal to:

$$E_m(\omega_i, R) = \omega_i^2 \mu\mu_0 \vec{G_0}(R, r_m) p_m(\omega_i, r_m) \tag{2.13}$$

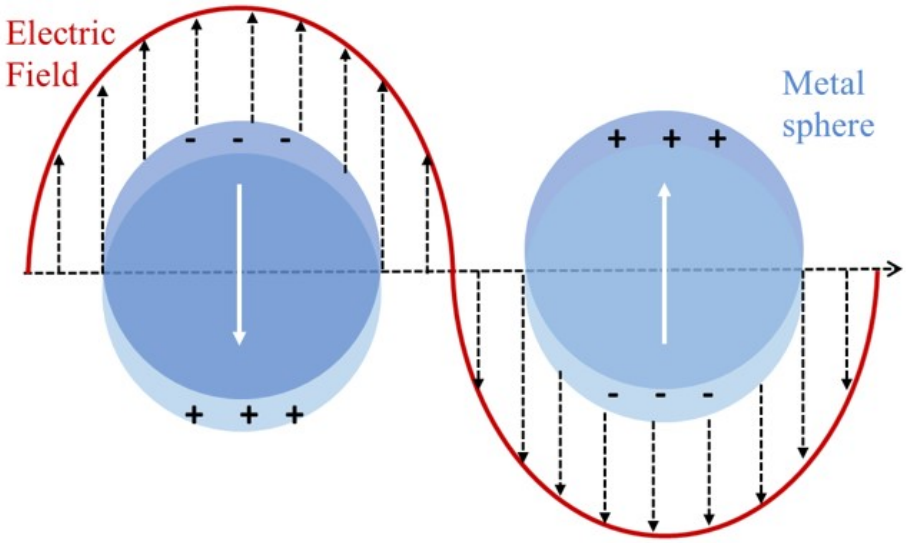

Figure 2.2. Schematic representation of the surface plasmons.

Where $\mu$and μ_0 are the relative permeability of the medium and vacuum, respectively. The $\vec{G_0}(R, r_m)$ stands for the dyadic green function in an homogeneous medium. The power irradiates from the induced dipole in the far field can be written considering the local induced electric and magnetic field (E_m and H_m):

$$P_m(\omega_i, r_m) = \iint_S \frac{1}{2} Re[E_m(\omega_i, r_m) \times H_m^*(\omega_i, r_m)]\hat{n}ds \tag{2.14}$$

where $\hat{n}$ is the normal vector along the p_m direction.For an isolated oscillating dipole, the power is also equal to:

$$\begin{aligned} P_m(\omega_i, r_m) &= \frac{1}{2}\omega_i Im[p_m^*(\omega_i, r_m) \cdot E_m(\omega_i, r_m)] \\ &= \frac{\omega^3}{2}\frac{|p_m|^2}{c^2\epsilon_0\epsilon_m}[n_p \cdot Im\vec{G_0}(r_m, r_m) \cdot n_p] \end{aligned} \tag{2.15}$$

The equation 2.15 represent the power of an isolated oscillating dipole in free space, where ϵ_0 and ϵ_m are respectively the dielectric constant of the

vacuum and of the material. The local electromagnetic field enhancement is primarily due to the LSPRs, resulting in a SERS signal. The local electric field strength at position r_m(the molecule location) is proportionate to the incident field as :

$$E_{loc}(\omega_0, r_m) = g_1(\omega_0, r_m)E_0(\omega_0) \tag{2.16}$$

Where $g_1(\omega_0, r_m)$ is the local electromagnetic field enhancement factor. Consequently, this field produces a strong oscillating dipole at Raman frequency ω_i:

$$p_m(\omega_i, r_m) = \alpha_m^I(\omega_i, r_m)E_{loc}(\omega_0, r_m) \tag{2.17}$$

The radiation characteristics of an oscillating dipole are significantly affected by the dielectric properties of what surrounds it and their optical resonance processes. The power is proportional to the second power of the dipole, according to equation 2.15, so the enhancement factor of the local field is :

$$M_{loc}(\omega_0, r_m) = |g_1(\omega_0, r_m)|^2 = \left|\frac{E_{loc}(\omega_0, r_m)}{E_0(\omega_0, r_m)}\right|^2 \tag{2.18}$$

The incident wavelength significantly affects amplitude, showing resonances associated with LSPR.

Radiation enhancement in SERS

Considering the enhancement factor (EF) of the electromagnetic field as a two-phase process, conceptually allows to understand where the generated power comes from but at the same time does not produce the correct solution to the problem. The correct solution is obtained by expressing the problem considering a plasmon structure coupled to a radiant dipole in the presence of an oscillating electromagnetic field. Referring to equation 2.15, the oscillating dipole $p_m(\omega_i, r_m)$ in the presence of a plasmonic nanostructure produces a total power equal to:

$$P_{tot}(\omega_i, r_m) = \frac{1}{2}\omega_i Im[p_m^*(\omega_i, r_m)E_m(\omega_i, r_m)] \tag{2.19}$$

The local electromagnetic field $E_m(\omega_i, r_m)$ is calculated using Maxwell equations, considering that is produced by the induced dipole $p_m(\omega_i, r_m)$

in the presence of metallic nanostructure (source). The dissipated power at the Raman-scattered frequency $\omega_i$is the sum of two contribute, a part is radiated into the far field and e some is dissipated as heat, by Joule effects, in plasmonic nanostructure. The first term is the radiated power P_{rad} and the latter is the non radiative term P_{nr}. Into far field at distance R, the Raman radiation field is composed of two term, as power:

$$E_R(\omega_i, R) = E_{DR}(\omega_i, R) + E_m(\omega_i, R) \tag{2.20}$$

Where $E_{DR}(\omega_i, R)$is the secondary field scattered from the enhanced field $E_m(\omega_i, R)$, excited by $p_m(\omega_i, r_m)$. The $E_{DR}(\omega_i, R)$ represents the dipole re-radiation field and the power associated is :

$$P_{rad}(\omega_i, r_m) = \iint_S \frac{1}{2} Re[E_R(\omega_i, r_m) \times H_R^*(\omega_i, r_m)]\hat{n}ds \tag{2.21}$$

By integrating in the plasmonic structures (V) and considering the conductivity σ, the non-radiative power is equal to:

$$P_{nr}(\omega_i, r_m) = \iiint_S \frac{1}{2} Re[E(\omega_i, r_m) \cdot E^*(\omega_i, r_m)]dV \tag{2.22}$$

The radiation enhancement depends critically on the orientation of the oscillating dipole. The power of the total Raman-scattered radiation is:

$$\begin{aligned} P_{tot}(\omega_i, r_m) = & \frac{1}{2}\omega_i Im[p_m^*(\omega_i, r_m) \cdot E_m(\omega_i, r_m)] \\ & - \iiint_S \frac{1}{2} Re[E(\omega_i, r_m) \cdot E^*(\omega_i, r_m)]dV \end{aligned} \tag{2.23}$$

In the absence of a plasmonic nanostructure, by the surface integral of the Poynting vector in the far field, the radiant power from an isolated oscillating dipole is given by:

$$\begin{aligned} P_0(\omega_i, r_m) &= \frac{1}{2}\omega_i Im[p_m^*(\omega_i, r_m) \cdot E_m^v(\omega_i, r_m)] \\ &= \frac{\omega^3}{2}\frac{|p_m|^2}{c^2\epsilon_0\epsilon_m}[n_p \cdot Im\vec{G_0}(r_m, r_m) \cdot n_p] \end{aligned} \tag{2.24}$$

where $E_m^v(\omega_i, r_m)$ is the virtual local field produced by the isolated dipole assuming there is no nanostructure. Consequently, the radiation enhancement M_{rad} is the radio between the radiative power and power P_0 is usually approximated as:

$$M_{rad}(\omega_i, r_m) = \left| \frac{E_{loc}(\omega_i, r_m)}{E_0(\omega_i, r_m)} \right|^2 \approx \left| \frac{E_{loc}(\omega_0, r_m)}{E_0(\omega_0, r_m)} \right|^2 \approx M_{rad}(\omega_0, r_m) \quad (2.25)$$

where $E_{loc}(\omega_i, r_m)$ is the local electromagnetic field generated by the field $E_0(\omega_i, r_m)$ at frequency ω_i. Thus leads the factor $M_{rad}(\omega_i, r_m)$ is :

$$M_{rad}(\omega_0, r_m) \approx \left| \frac{E_{loc}(\omega_0, r_m)}{E_0(\omega_0, r_m)} \right|^2 \quad (2.26)$$

When ω_i is approximately equal to ω_0 (for detail see [38]). The SERS enhancement factor (EF) is:

$$EF(\omega_0, \omega_i, r_m) = \frac{P_{rad}}{P_{m,0}} = \frac{P_0}{P_{m,0}} \cdot \frac{P_{rad}}{P_0} = \frac{P_0}{P_{m,0}} \cdot M_{rad}(\omega_0, r_m) \quad (2.27)$$

The term $M_{rad}(\omega_0, r_m)$ is the radiation enhancement meanwhile the first term is:

$$\frac{P_0}{P_{m,0}} = \frac{\frac{\omega^3 |p_m|^2}{2c^2 \epsilon_0 \epsilon_m} [n_p \cdot Im\vec{G}_0(r_m, r_m) \cdot n_p]}{\frac{\omega^3 |p_{m,0}|^2}{2c^2 \epsilon_0 \epsilon_m} [n_{p,0} \cdot Im\vec{G}_0(r_m, r_m) \cdot n_{p,0}]} \quad (2.28)$$

neglecting that $n_p \neq n_{p,0}$, meaning that the direction of the oscillation dipole in the system with nanostructure is different from the direction in free space (due to the change of polarization of the local field with respect to the incident field). Thus leads to:

$$\frac{P_0}{P_{m,0}} \approx \left| \frac{E_{loc}(\omega_0, r_m)}{E_0(\omega_0, r_m)} \right|^2 \approx M_{loc} \quad (2.29)$$

If the incident frequency ω_0 is approximately equal to ω_i the Raman frequency, the above equation can be simplified to:

$$EF(\omega_0, \omega_i, r_m) \approx \left| \frac{E_{loc}(\omega_0, r_m)}{E_0(\omega_0, r_m)} \right|^2 \cdot \left| \frac{E_{loc}(\omega_i, r_m)}{E_0(\omega_i, r_m)} \right|^2 \quad (2.30)$$

In other words:

$$EF(\omega_0, \omega_i, r_m) \approx \left| \frac{E_{loc}(\omega_0, r_m)}{E_0(\omega_0, r_m)} \right|^4 \tag{2.31}$$

The equation 2.31 is the well-known as the $|E|^4$ approximation for the EF. In the first phase of enhancement, an antenna collects light from a larger volume and focuses a large part in a localized part of the antenna, i.e. "hot spot"; in the second phase the local electric field pushes the antenna radiate resonantly due to the emission by the molecules located in the hot spot. Considering that EF in eq. 2.31 is position dependent, it is often reported in the literature as surface average EF[38]. Having a large number of zones where the field is strongly localized leads to a higher intensity of the SERS signal, improving sensitivity. By engineering ordered arrays, it is possible to obtain a large number of hot spots (due to gaps at intersections between the nanoparticles of the structure) with the advantage of better uniformity[46]. Considering two small nano-spheres, in figure 2.3 is shown as the strongest local field enhancement is located along the "x" axis through the centre of the spheres , and is oriented along the "y" axis in the the direction of the external field.

2.3 Plasmonic material

The SERS effect is due to the amplification of Raman signals by plasmonic effect, caused by the presence of a metal nanostructure. To achieve good signal amplification it is necessary to optimize the geometric structure of the nanostructure and the material used. Regarding the geometry of the substrate chosen, the next chapter 3 will discuss the various types of substrates manufactured over the years, providing an overview of the state of the art.The phenomenon of plasmon at optical frequencies arises from the collective oscillation on the surface of the free charges due to an applied electric field. Therefore, for plasmonic materials to be defined as such, they require an abundance of free electrons and therefore of metal components. This abundance of free electrons defines a negative real permeability (main characteristic of a plasmonic material). However, generally metals are characterized by large losses especially in the visible optical band, due to inter-band electronic transitions [47]. Leakage in the materials limits, in many cases, the applications of plasmonic devices and causes a drastic

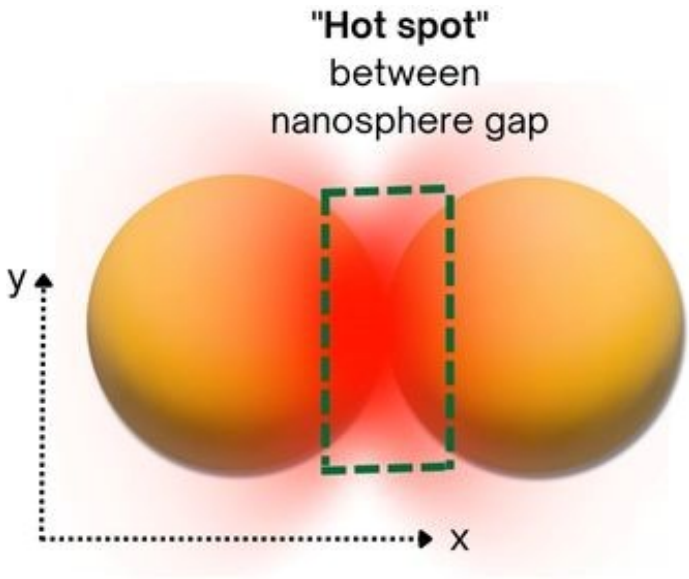

Figure 2.3. Schematic representation local electric field distribution.

decrease in performance. Low-loss plasmonic materials are needed to have overall high performance [48]. The iteration between an electromagnetic field and a material is described by polarization. Polarization can be both electrical and magnetic in nature, although the magnetic is negligible for materials that work at frequencies higher than THz. The complex dielectric function of a material (permittivity, "$\epsilon(\omega)$") well describes the state of electrical polarization. The permittivity consists of a real part ($\epsilon^{'}(\omega)$) that deals with the polarization induced by an external electric field and, an imaginary part that deals with the losses induced by polarization. Consequently, a low-loss material is defined as having ($\epsilon^{''}(\omega)$) low values. In the frequency range of near infrared, visible and ultra-violet, the mechanisms that feed the losses are mainly due to conduction electrons and inter-band effects [49]. The former derive from electron-electron iterations, while the latter are due to interaction between electrons and photons. Therefore, metals are excellent candidates due to their high conductivity, for plasmonic applications and consequently for SERS applications. The most commonly and widely used materials are gold and silver.

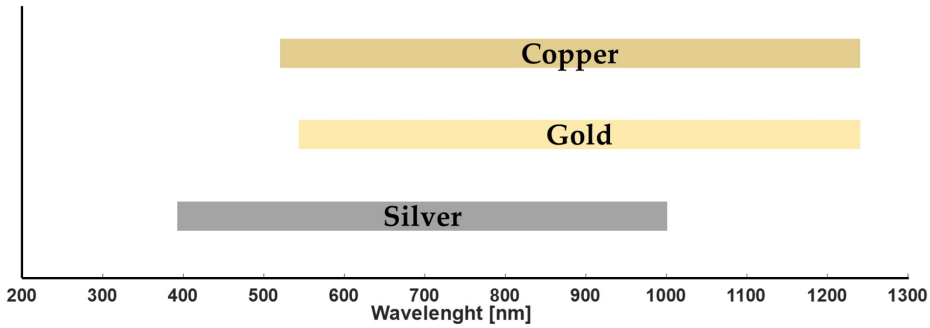

Figure 2.4. The wavelength ranges where SERS applications are supported by Silver, Gold and Copper.

These two metals have low losses in the visible and near infrared fields. In fact, almost all the experimental panorama on plasmonics devices uses these two materials [50], they predominate mainly in the SERS field [51]. Other metals have been used but their use has been imitated by high losses compared to these two materials. For example, in applications where the catalytic function of metals is fundamental, materials such as platinum and palladium find a context[52]. However, silver tends to degrade very quickly and the roughness of the surface also significantly determines the losses in the material[53]. On the other side, gold represents the best plasmonic material in terms of losses (in the visible and near infrared), is chemically stable and can form continuous films [54][55]. Silver and gold layers are typically made using physical vapor deposition (PVD) and/or sputtering techniques. Silver, gold and copper has LSPRs, covering the visible range where the most Raman phenomena occur (schematic representation in figure 2.4). Copper has the second highest conductivity (such as silver), also considering that the costs are considerably lower than gold and silver should be an excellent candidate as a plasmonic material. Chan et al. have shown that nanospheres made of copper have an LSPR response comparable to that of gold and silver. However, in practical cases [56],copper has been shown to oxidise very quickly (forming Cu_2O and CuO). Due to oxidation effects, copper is not suitable for plasmonic applications, much less for SERS applications. Aluminium was not a material used compared to those mentioned above, due to the fact that it has high values of the imaginary part of the permittivity in the range of visible wavelengths.

However, aluminium is better than gold and silver (in the ultraviolet range), albeit at relatively low values. Under atmospheric conditions, such as copper, aluminum has a tendency to oxidize (forming layers of Al_2O_3), making it difficult to manufacture and use. The typical thickness does not exceed 3 nm [57]. Despite everything has been used over the years for plasmonic [58], fluorescence [59] and Raman applications [60]. Like aluminum, plasmonic materials in the ultraviolet wavelength range are metals that typically have inter-band transitions in the range from 200 to 400 nm. In the ultraviolet range, photon energy is higher due to molecular resonance phenomena (i.e photocatalysis and/or photodegradation), increasing sensitivity and exploiting higher energy resonances than visible [61]. Besides aluminum, there are other non-traditional metals that can exploit resonances in the ultraviolet wavelength reason, such as rhodium, indium, and magnesium [62][63]. Nanoparticles made of rhodium have been manufactured and used for SERS and fluorescence (deep ultraviolet) applications successfully for biosensing [63][64]. On the other hand, arrays of indium nanoparticles have been created with excellent results mainly for applications involving photodetectors and refractive index variation measurements [65], while colloidal nanoparticles were also used for ultraviolet SERS [66] and molecular imaging [67]. Colloidally synthesized, nanoparticles composed of magnesium and an oxide layer of about 6 nm exhibit a resonance in the ultraviolet range, highly dependent on shape and size [68]. To free them from the dependence of shape and size, materials such as bismuth, antimony, and gallium have a plasmon resonance tunable in the ultraviolet range, mediated by inter-band transitions [69]. Metals (i.e Gallium, indium, rhodium and platinum), alkaline metals (Lithium, sodium, potassium, cesium and rubidium) and metal alloys have been studied to be candidate materials for SERS substrates [70]. However, these materials are highly reactive in the air, which is why their applicability remains excluded from the SERS scope. Developing methodologies capable of overcoming this type of reaction would allow new ways of making metal SERS substrates. Although they do not fit the conventional definition of SERS substrates, new materials such as graphene [71], semiconductors such as titanium dioxide (TiO_2 [72], and quantum dots [73] have been used as SERS materials.

Titanium nitride (TiN), like other transition metal nitrides, supports a plasmon resonance in the visible range due to their high free electron concentrations unlike nitride oxides [61][74]. Because of their low carrier concentrations, semiconductor materials face numerous challenges to obtain an LSP in the view [75]. However, strongly doped semiconductor materials represent an emerging platform in the field of plasmon, being strongly tunable in near infrared wavelengths [76]. In fact, the transparent conduction materials oxides are dopable and allow to obtain plasmonic resonances throughout the near infrared (i.e. aluminum-zinc oxide and indium-tinoxide). These properties in the near infrared are also characteristic of materials such as sulphides and transitional metal oxides [61]. Combinations of different materials increased the charge carrier density and enabling a tunability in the near infrared, such as fluorine/indium co-doped cadmium oxide and fluoride/tin co-doped cadmium oxide [77]. By changing the concentration of dopants to improve system response and near-infrared tuning, Copper-Sulfur/Selenium are other materials that can be manipulated.[78] Materials composed of cus or cute are semiconductors that perform a self-healingdoping due to oxidation, allowing LSPR and are mainly used in optical communication [79] . Like the metals Transition oxides, Ruthenium(IV) oxide are excellent candidates for photonic applications thanks to negative permittivity and low losses [80]. Extending the landscape of traditional plasmonic materials expands working wavelengths from deep ultraviolet to mid-infrared. Thus overcoming materials such as gold and silver, to use 2-D materials, non-noble metals and semiconductors, would improve a wide variety of optical processes, opening new possibilities in different application fields (especially in the field of plasmonic and SERS). The fields of application and the ways in which the materials can be used increase with the increase of the variety' of compositions of materials, which present plasmonic characteristics. In order to make the best of "new plasmonic composite materials", research must focus mainly on two fundamental aspects: intrinsic properties and cooperative interactions. On the other hand, future discoveries on high-performance plasmonic materials require advances in the accessibility of new materials, in the better understanding of dielectric function and processes regarding resonance phenomena.

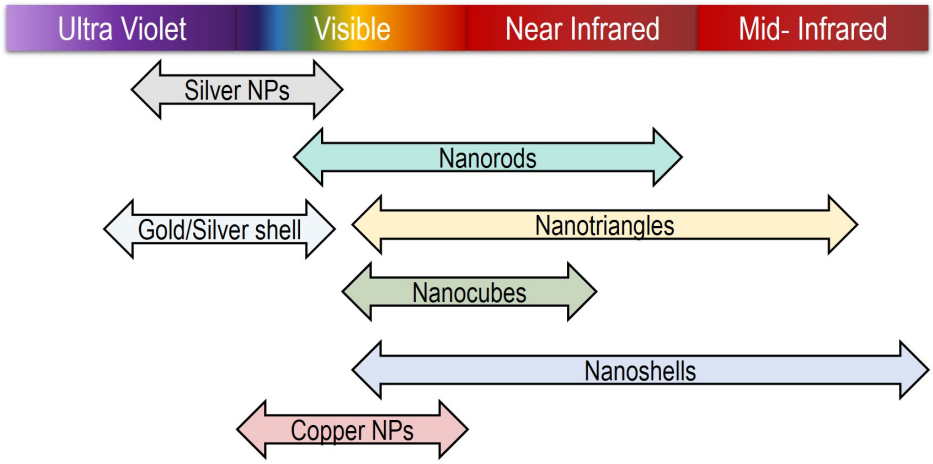

Figure 2.5. Qualitative representation of plasmonic structure, related to material and shape.

Therefore, thanks to the use of some metallic and non-metallic materials, it is possible to widen the window of the electromagnetic spectrum of absorption and use of photons. Over the years, the scientific community has focused on increasing the enhancement factor of SERS substrates from a material point of view. Overcoming single-layer substrates, recent progress involved in the use of combined materials. Guanliang Sun et al. proposed a substrate of silver nanoparticles combined with cobalt oxide nanowire on copper foam framework. The substrate is fabricated by successive two-step hydrothermal synthesis strategy [81]. The combination of these material evolved in high enhancement factor approximately equal to $2 \cdot 10^8$. Another example, Jagannath Rathod et. al. proposed different substrate using Germanium (Ge) substrate combined with silver and gold nanoparticles, obtaining enhancement factor up to $\cdot 10^5$ [82]. Thus, improving the dielectric function of a material for itself is not sufficient to increase plasmonic coupling. A purely qualitative representation of the response of different structure is schematized in figures 2.5, to correlate the dimensions, type of structure, materials to the spectral range of wavelengths.

To observe a greater chemical and physical functionality, aspects such as geometry, surface structure, dimensions of the basic elements, fabrication and surface functionalization are necessarily to be taken into account, developing a strategy that takes into account all the parameters. Andrei Nemilentsau et. al. have observed the phenomenon of oxidation in cubic silver nanoparticles with a platinum shell and, how to detect plasmonic phenomena. From their study a fundamental aspect emerged, namely that there was no transfer of plasmon energy from the platinum shell to the silver core [83].On this line instead , incorporating semiconductor materials inside metals would allow a greater and more effective separation of free carriers of charge, exhibiting greater plasmonic activity [84][85].

Chapter 3

SERS-active substrates: state of art

In this chapter a detailed description of the current state of art related to the SERS substrate is provided. In particular, the chapter is divided in two main paragraph. The first described the planar substrate scenario and the latter the fiber optic SERS probe current state. In particular, some of the most commonly used manufacturing techniques are described, illustrating the relative advantages and disadvantages. An overview of substrates from the simple single nanoparticle to the orderly and amorphous shapes of arrays, to the more complex structures in multiple dimensions. The aim is to provide information about the most influence parameters to obtain regular, uniform, reproducible and high highly performing in terms of enhancement factor SERS active substrate. All of these aspects have a significant impact on the design of the substrate. In particular the techniques used to fabricate SERS planar substrates are not always suitable for fiber optic fabrication (as for planar substrates) and consequently there is a decrease in performance. Indeed, the following chapter provides an overview of the state of the art of planar substrates and fiber optic substrates. Working with fibers has many advantages in terms of achievable applications, but at the same time not all fabrication techniques are usable (as for planar substrates) and consequently there is a decrease in performance.

3.1 Planar SERS active substrates

The Raman signal is strongly enhanced when these molecules are adsorbed on or are in close proximity to a metallic surface. In the chapter 2, is briefly described the mathematical formalism and the physics phenomena behind the SERS scattering. The SERS rely on the optical excitation of surface plasmons, in particular on the collective vibrations of the free electrons in the nanostructure. The sensitivity enhancing of the substrate is a crucial factor in SERS detection [86]. The sensitivity of a SERS substrate is mainly due to the presence of hot spots. By increasing the number, strength, density, and distribution, the intensity of the resulting SERS signal grows [87]. Hot spots are strongly influenced by factors such as the shape, size and material of the nanostructure. L. B. He et al have shown that the presence of nanogaps between nanoparticles is the cause of more than the half of the SERS signal [88]. Following a numerical simulation study from the work of Yu Huang et al. it emerged that by increasing the size of the gap between two nano spheres the local field enhancements decreased drastically exceeding 30 nm [89]. To have a SERS signal it is important that the substrate has a uniform distribution of hot spots, present in a large number and especially accessible to the target molecule (figure 3.1). Another aspect not to be underestimated is the choice of the fabrication method. Choose fabrication methods that take a long time or are very expensive, are not akin to a university research environment or mass production. In the medical field it is necessary that the substrate is low cost so that it can be used without limitations (for example in the field of diagnostics it may be necessary to carry out multi tests). The substrate must also be reliable and ensure repeatability. The well-known proposed SERS active substrates generally consisted of various nanoparticle aggregates to achieve a high density of hot spots. In literature it is easy to find simple particles aggregates as nanorods [90], nanostars [91][92], nanopyramids [93][94], nanocubes [95][96], nanotriangles [97][98], nanoprisms [99] and nanoflowers [100][101]. Nonetheless, the relatively poor repeatability and uniformity of such SERS-active substrates seriously limits the practical use as quantitative measurement [102].

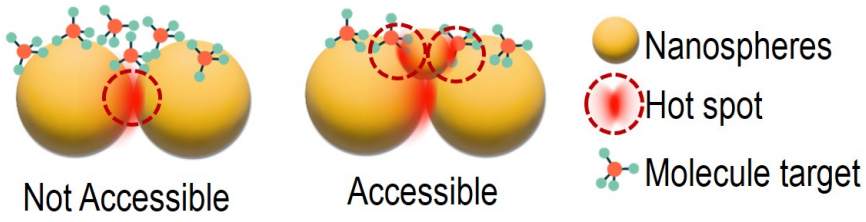

Figure 3.1. Graphic explanation of the importance of the accessibility of the hot spot to the target molecule.

In the last decades, several plasmonic nanostructures with a controlled size, shape, composition, and arrangement have been proposed as SERS-active substrates in the literature. A schematic overview of different plasmonic nanostructures are showed in figure 3.2. Commonly, the aggregates nanoparticles are made via chemical reduction method using solutions, tuning the types and concentrations of reductants can be optimized (or other parameters as reaction time and temperature, and surfactant types) [103]. Through the method of chemical attack, Chiba et al. exploited the effect of the gaps between a nanosphere and a film (both silver) to investigate a gap mode plasmon under an attenuated total reflection [104]. Despite the simplicity, it is difficult to have accurate control over the size and shape of the desired nanostructures [105]. Many SERS substrates have been fabricated by lithography based approach, i.e by lithography-based approach, i.e by focused ion beam (FIB) and electron beam (EBL) [106]. FIB is a direct writing process which utilizes a narrow-scanning ion beam source about 20 nm diameter, typically of gallium ions [107]. For the detection of the influenza A virus strain, Sivashanmugan et al. have decided to manufacture a well ordered Au/Ag multilayered nanorod arrays via the focused ion beam technique, tuning the shape and the thickness of each layer [108]. Alongside by FIB, Mandelbaum et al. created a structure made of depressions (open cavities), drilled into the silver layer. A SERS pixel array was provided as sensors of spatially real-time monitoring of a chemical reaction, by resolved measuring the chemical pH in fluid [109]. The EBL approach employs the focused electron beam able to perform patterns with higher resolution down to 10 nm [110], directly on electron-sensitive resist.

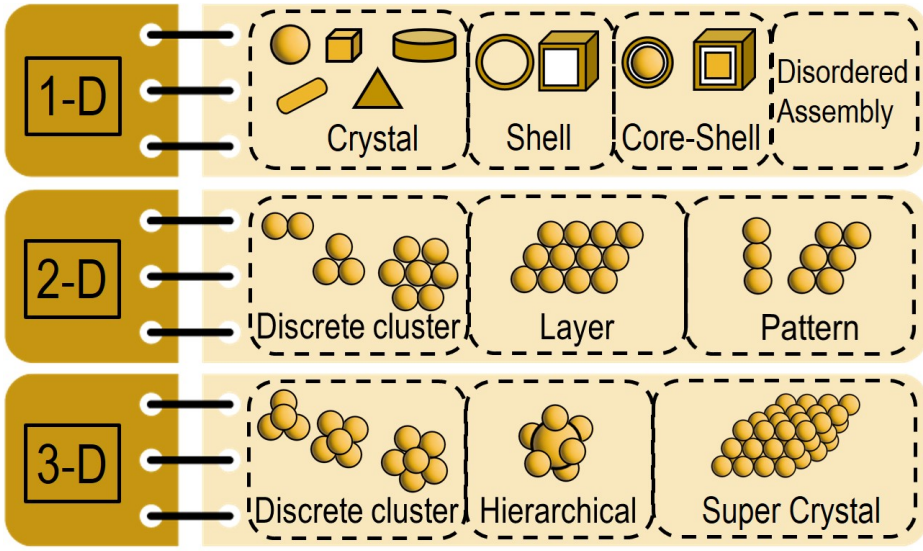

Figure 3.2. Schematic representation of the diversity geometry of nanoparticles.

The principle of operation is based on the fact that the resist material (usually polymethyl methacrylate) changes its properties as a result of exposure upon electron, without the use of mask. Ahmed et al. fabricated an arrays of 50 nm pitch gold nano-dots on fused silica substrates, created high-quality periodic arrays, using 10 keV EBL [111]. Das et al. proposed the use of nanoimprinting lithography combined to EBL to fabricate gold nanopyramids on a polymer substrate, obtaining an uniform pattern [112]. Meanwhile Alvarez-Puebla et al. were able to fabricate grating and pillar films prepared by nanoimprintig and physical vapor deposition (with no time-consuming as EBL), using a layer of 200 nm polystyrene as imprint resist [113]. Nanoimprintig lithography deals with mechanical deformation of the imprint resist and subsequent processes, resulting in the creation of nanopatterns. In this case the imprint resist is predominantly a polymer cured by heat or light UV. The technique's drawback is the lack of control over the material quantity that is deposited [114].

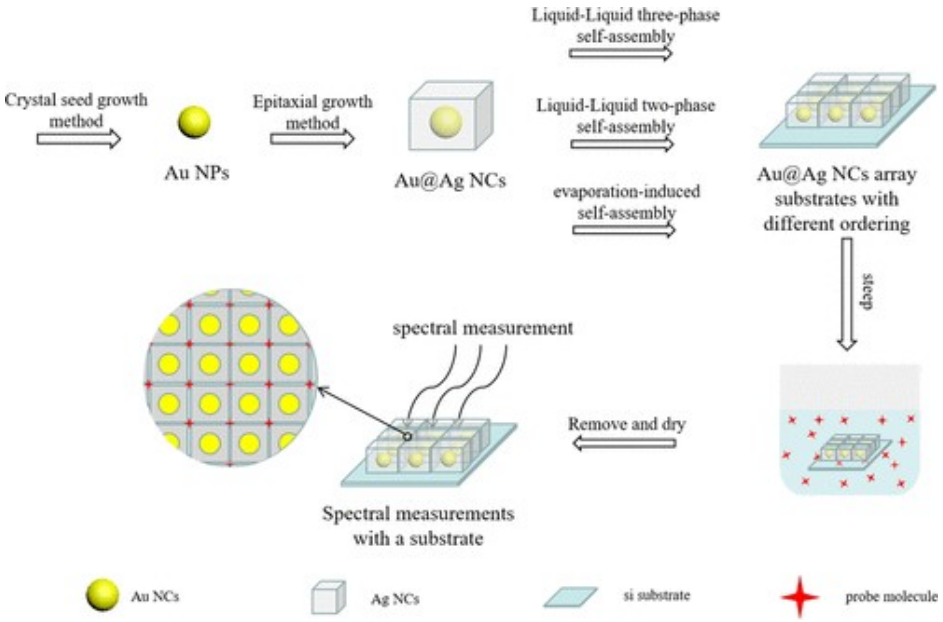

Figure 3.3. Preparation of different Au@Ag NC substrates with different arrangements and the subsequent SERS detection flow chart [1]. Copyright © 2022 The Authors. Published by American Chemical Society.

Qi Zhang et. al made a pyramid microstructure coated with silver and covered with nano silver cubes, combining two fabrication techniques one is the 3D laser photo-lithography and the self-assembly. The results was to observe that the hot spot densities were extended along the z-axis in the 3D SERS substrates [115]. These fabrication techniques allow the fabrication of various regular geometries with a high spatial resolution. Meanwhile the lithography-based approaches are extremely expensive, making their use not worthwhile for large-scale fabrication (due to low fabrication efficiency) [116]. Large and regular nanostructure patterns can be produced through a low-cost production process using bottom-up self-assembly techniques, which is an interesting alternative [117]. SERS active substrates that are well-ordered have been created successfully through various self-assembly approaches [20][118][119]. Jun Dong et al. realized a substrate composed by a gold nanoparticles coated with silver nanocubes [1].

In figure 3.3 is reported the flow chart of the fabrication process, showing also the schematic morphology of the substrate. The sample was fabricated on a substrate of monocrystalline silicon, following the sequence of three-phase and two-phase liquid-liquid self assembly and evaporation-induced self-assembly methods. Using this method, different structure with different $Au@AgNC$ arrangement patterns were obtained with a regular morphology and uniform size.

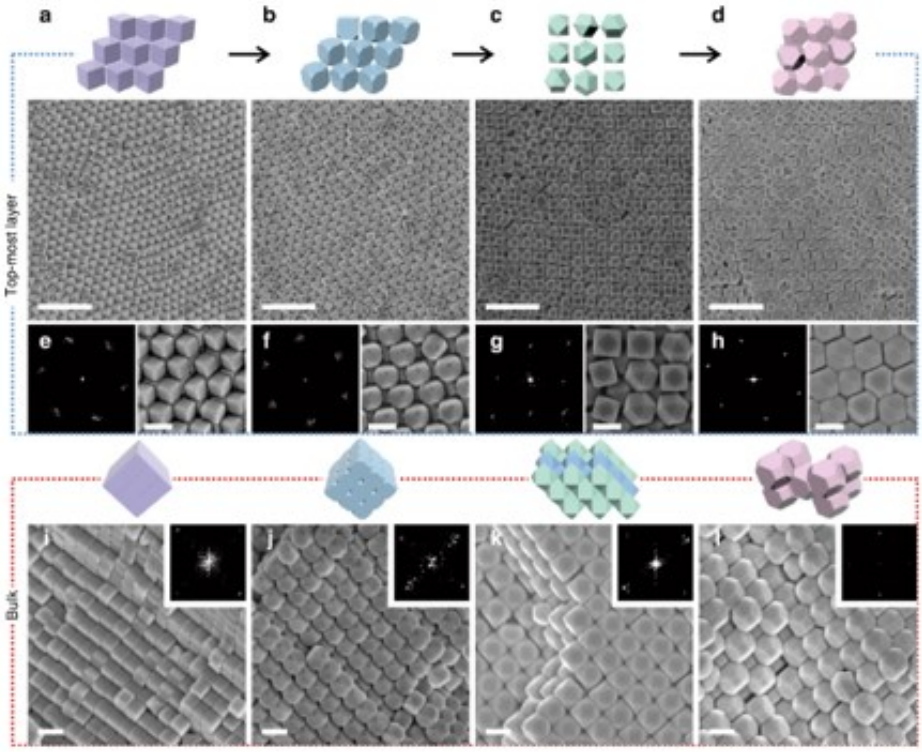

Figure 3.4. Dual crystal structures of Ag polyhedra. Top-view SEM characterization of (a) nanocubes, (b) truncated nanocubes, (c) cuboctahedra, and (d) truncated octahedra.(e–h) FFTs and close-up images of the various assembled structures.(i–l) Cross-sectional characterization of the bulk supercrystals. Insets are FFTs of the bulk crystal structures.(a–d) Scale bars, 1 µm; (e–l) scale bars, 200 nm [2].

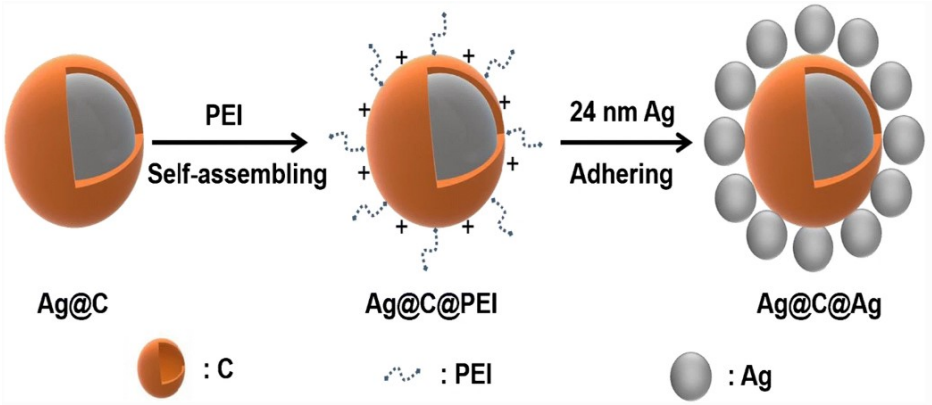

Figure 3.5. Schematic illustration of the synthetic process of $Ag@C@Ag$ NPs [3].

Xiaolin Huang et al. report a controllable and reproducible SERS substrate vesicles based (made up of gold nanoparticles that have been properly treated), by self-assembly approach [120]. Yih Hong Lee et al. demonstrated how implement the one assembly with dual structures, for a family of shape-controlled silver polyhedral, realizing different shape nanostructure as nanocube, truncated nanocube, octahedra, and cuboctahedra [2]. In figure 3.4 are reported the SEM characterization of the fabricated substrates, using a solvent evaporation-driven assembly system. In addition, the manufacturing process allow to obtained regular and uniform pattern (as shown in figure 3.4), with the possibility of controlling the number of vertices (i.e. the presence of tips) and the shape with accuracy. Xiaoli Xin et al. report an easy method to fabricate more complex structures based on self-assembly methodology [3]. The substrates is prepared by a low-temperature heating-stirring method, subsequently modified with polyethyleneimine and at least the particles are united using self assembly technique. The sample is made by a structure composed of silver spheres with a carbon shell and covered with a layer of smaller spheres of silver. In figure 3.5 is presented the schematic illustration of the process and the structure. Among the proposed self-assembly techniques, nanosphere lithography (NSL) is perhaps the most commonly used method.

Van Duyne's group demonstrated the ability to generate a wide variety of nanoparticles structures and ordered patterns by exploiting regular self-assembly of nanospheres [121]. Over the years, the same group has systematically examined the applicability of these structures to SERS applications. In addition, by further developing the basic concept of the NSL, many different structures have been fabricated with various morphology (i.e. rings, rods, dots) [4][122]. In figure 3.6 are reported two substrate, realized using in combination the nanosphere lithography and annealed polystyrene nanospheres masks [4]. The SERS active substrates made by NSL founds place in different field of application, such as chemical and biological sensing [39], [123]. The NSL has also been specialized to work efficiently directly on optical fiber tips [25] to produce engineered SERS optrodes for remote measurements and in-situ biological sensing [124].

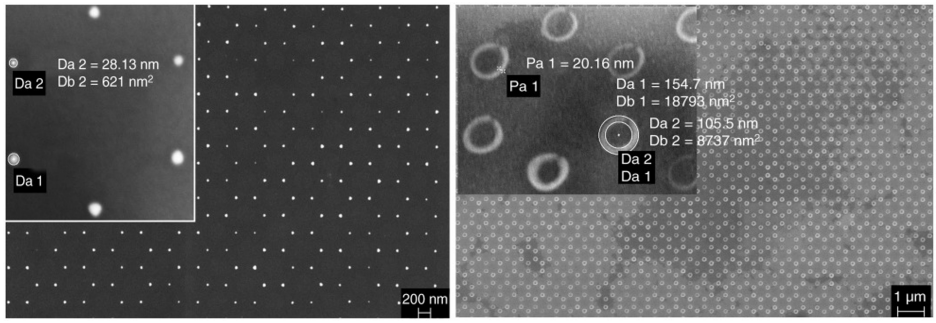

Figure 3.6. Fabrication of Nanoscale Rings, Dots, and Rods by Combining Shadow Nanosphere Lithography and Annealed Polystyrene Nanosphere Masks [4].

In addition to the aforementioned advantages, fiber optic optorodes allow to expand the application fields for advanced diagnostics, developing point-of-care technologies that can be integrated directly into medical devices in vivo. On the other hand, this technology requires that active SERS substrates are highly regular, uniform with accessible and highly dense hot spots [26]. On this line, Xiaolei Zhang et al. created a "sunflower-like" SERS substrate by preparing binary colloidal crystals coated with silver nanoparticles [125].

Advanced hierarchical hybrid nanostructures are currently being studied that are able to extend SERS hotspots into the third dimension (thereby increasing their spatial density)through controllable low-cost and easy fabrication techniques based on NSL. So far, by employing NLS, hierarchical nanostructures have already been successfully fabricated, consisting of a nano array with nanocaps or nanotriangles [126], and nanotowers or nanodisks [127] demonstrated using NSL.

3.2 Optical fiber SERS substrates

The need to detect the presence of certain molecules may arise in various scientific fields. In the field of pharmacology, industrial water discharge or food safety, the detection of toxic substances [128][129] is fundamental. In the medical and biological field determine the presence of cancer cells, it can be vital and support surgical operations and or diagnosis [130]. In the literature, it is possible to find different works on detection methods (qualitative and quantitative), depending on the various application scenarios [131][132][133]. However, these detection methods fail to meet the requirements for fast, small-sized, online measurements. SERS spectroscopy, considered the fingerprint of a molecule, is suitable for use as a non-destructive test. SERS substrates provide high EF values, but are not suitable for tests that require short time and in situ detection. In this context, the optical fiber integrated with an active SERS substrate find his place [134]. Fiber optic SERS probes represent an excellent synergy between the sensitivity of Raman spectroscopy and the small-scale versatility of fiber [135] On the other hand, fiber has unique advantages such as 'flexibility', ability' of detection in confined locations, dangerous environments and or curved paths. In other words, it enables fast, real-time detection and remote detection [136]. Another important advantage is that it plays both the guiding role (of light to the sample) and the role of low-loss receiver (collects the signal emitted by the sample) [137]. In the previous paragraph, different methods of nanoparticles fabrication method for different types of metallic/non-metallic substrates have been illustrated.

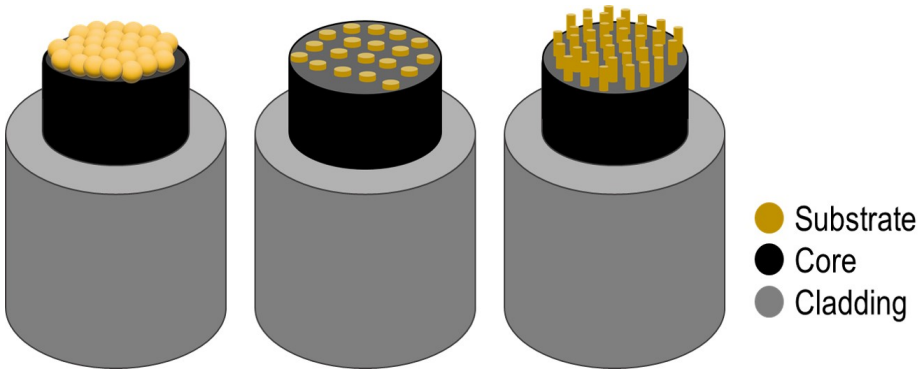

Figure 3.7. Examples of different SERS active substrate on the optical fiber tip.

However, fiber optics has a small cross-section, cylindrical surface, and chemical inertia that do not make it compatible with certain nanoparticle fabrication methods [138]. Nanoparticles, such as nanostars [139] or nanoflowers [140] (which present high local field enhancement values due to the high number of hot spots), are difficult to achieve on surfaces such as fiber optics, as a result fiber optic probes are unfavorable to having a high sensing sensitivity. Therefore, the substrate and its material must be designed and studied following the morphological, chemical and electromagnetic coupling characteristics of the optical fiber. In fact, another fundamental aspect consists in the matching between the fiber response with the LSPR response of the metallic nanostructure [141]. Modifying the end of the optical fiber with SERS substrates composed of gold or silver nanoparticles is an easy method of coupling the substrate to the fibre [142]. Through the use of this type of probes it is possible to obtain an EF in the order of $10^4 \div 10^6$, of some order of magnitude lower than the values obtained with a planar substrate $10^4 \div 10^{12}$ [143]. In figure 3.7 is possible to observe an example of different fabricable substrate on the optical fiber end face. In some applications, such as medical or biosensing [144], excellent spatial resolution may be required as well as EF. To optimize the fiber optic probe, other relevant parameters such as the numerical aperture, fiber length, and nano-array size must be taken into account.

Other methods of substrate fabrication on the tip of the suitably treated fiber optic are Sandblast roughening of the silica tips with subsequent metal coating or the creation of silver nanoislands by evaporation [145]. Focused ion beam milling and electron beam lithography are two techniques that allow you to create grating, nanoholes and periodic patterns with high precision [146][147]. At the same time they are two very expensive techniques and require long manufacturing times. In the 2016, Yu Lui et al. proposed the fabrication of a substrate composed of nanoparticles and made by laser-induced self-assembly technique [148].In the literature you can find several fiber optic devices integrated with SERS active substrate for bio-molecular recognition and other application fields [149][150][151]. Over the years, numerous advances have been made, from simple techniques aimed at obtaining homogeneous and uniform substrates to methods with more complex geometries for the optimization of the number of hot spots. In the 2022, Zhang et al. manufactured a hexagonally ordered gold nanospheres array (with 8 nm gap and 32 nm diameter) with a single-step method based on the self-assembly technique [152]. The substrate was manufactured by immersion (containing a solution with nanoparticles) directly on the fiber optic tip with the following characteristics: $\approx$ 0.5 m in length, 200 μm core diameter, 0.22 numerical aperture, visible/near infrared, fused silica fiber, polyimide coating and SMA905 connectors. Suited for chemical sensing, easily manufactured, the fiber substrate was tested using the marker 4-aminothiophenol (4-ATP), obtaining a significant EF of $3.5 \cdot 10^4$. Despite the advantages mentioned above, this type of method does not allow to obtain a uniform substrate (probably due to the not optimized immersion and annealing times). Similarly, the group of Pisco et al. manufactured several SERS substrates on fiber (classic single mode) using the self-assembly technique, demonstrating excellent reproducibility, uniformity and variability lower than 10% [153]. In particular, the approach is based on polystyrene nanospheres that at the interface between air and water self-assemble in a single-layer colloidal, whose periodic characteristics are defined merely by the size of the chosen particles. Tested with biphenyl-4-thiol (BPT) a molecule belonging to the family of thiols (such as 4-ATP), the SERS fiber probe obtained EF values equal to $4 \cdot 10^4$, quite higher than previous substrate.

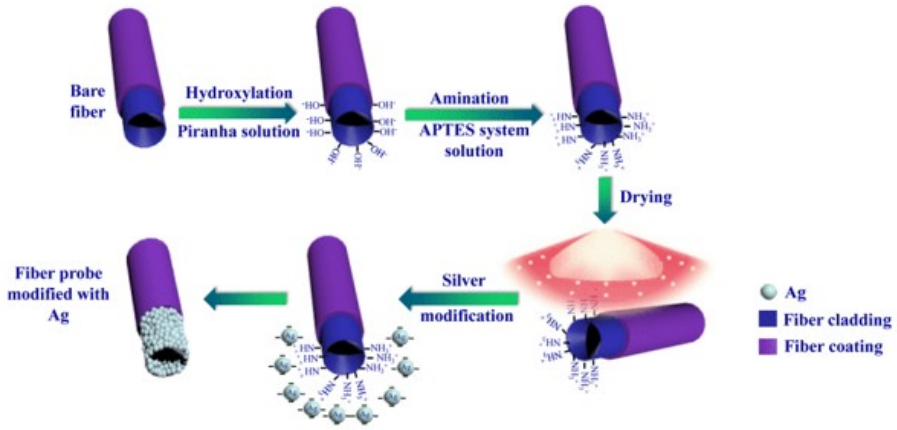

Figure 3.8. The experimental process of the self-assembly method of the fiber SERS probe [5].

Xinghu Fu used a more articulated self-assembly method to build a SERS probe on a multimodal fiber graded (with core and cladding diameter respectively equal to 62.5 and 125 μm) [5]. In figure 3.8 is shown the fabrication process used. The method is divided into two phases: a pre-treatment of the fiber (into piranha solution to hydroxylated the fiber surface) and a second phase in which the fiber is placed in the centrifuged nano-silver sol. Following this process they fabricated a substrate on the fiber tip with silver nanoparticles with exceptional EF values of $1.36{\cdot}10^8$. A silver-modified microcavity fiber SERS probe has been manufactured with exceptional results, but at the same time has the disadvantage that the use of silver limits its use for biological applications (considering the tendency of silver to oxidize [154]). The work of Thanh Binh Pham et al. fits in this context [155], proposing a high EF ($2.54{\cdot}10^7$) SERS fiber probe based on directly planting gold nanoparticles on the surface of silver nano-dendrites and fabricated an in-situ growth method with dual-laser assisted. The two layers of particles were fabricated on a spheroid end-facet optical fiber and tested with Rhodamine 6G (R6G).

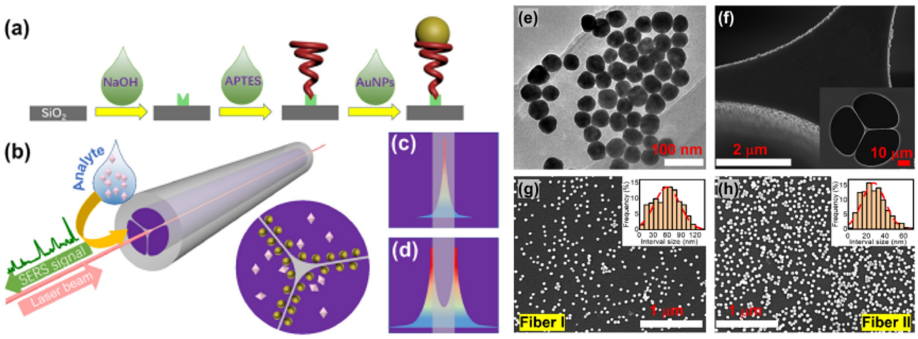

Figure 3.9. (a) Schematic illustration of the decoration procedures of AuNPs on the inner surface of suspended-core fiber. The fiber was cleaned with NaOH solution, functionalized with APTES solution, and AuNPs were immobilized on the fiber inner surface by bounding to amine groups. (b) Schematic illustration of the SERS probe based on AuNPs decorated suspended-core fiber. The SERS signal was collected in a backscattering configuration. (c) Schematic illustration of the power distribution of the core mode. (d) Schematic illustration of the power distribution of surface mode. (e) TEM image of synthesized AuNPs. (f) SEM image of the end face of suspended-core fiber decorated with AuNPs. Inset: SEM image of the end face of pristine suspended-core fiber. (g) and (h) SEM images of the inner surface of the fiber decorated with AuNPs. To expose the inner surface, the fiber was cut obliquely with a blade. Insets: Statistical plots of particle spacing [6]. Image © 2022 Optica Publishing Group under the terms of the Optica Open Access Publishing Agreement. [5].

Despite the peculiarity in using a spheroid end-facet optical fiber, this SERS probe has the double counterbalance of not having a uniform and reproducible pattern, given by the randomness in placing the gold nanoparticles and the use of silver that if not sufficiently covered could oxidize. Lei Zha et al. proposed a SERS probe based on AuNPs decorated suspended-core fiber made by chemical attachment [6] and showed in figure 3.9. The probe has reached an EF value of $1.02 \cdot 10^8$. The peculiarity of this probe consists in the use of a suspended-core fiber with gold nanoparticles on the inner surfaces of the suspended-core fiber, by bounding to amine groups (figure 3.9 b). Particularly innovative and with a high EF, but at the same time the use of a chemical preparation process, does not allow to control factors such as the size of nanoparticles and the uniformity of the layer

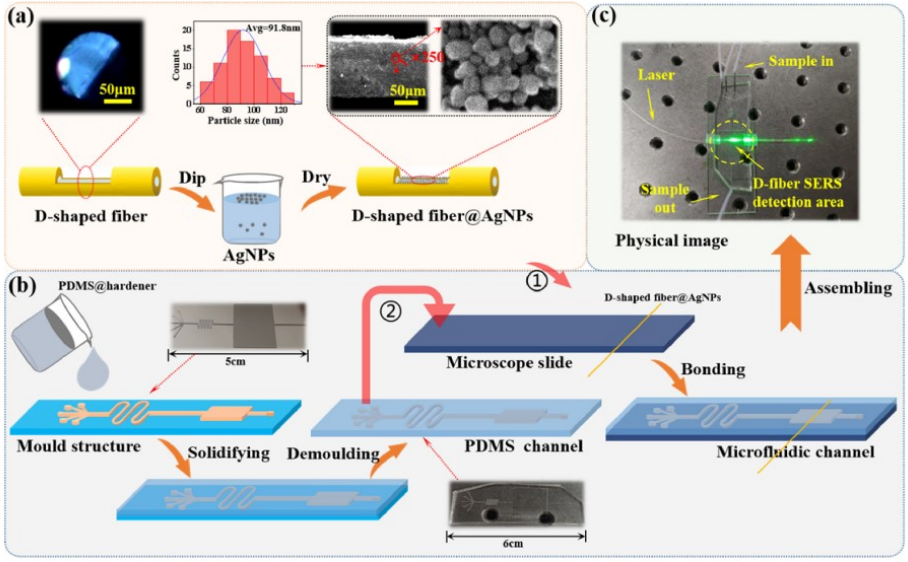

Figure 3.10. Experimental process flowchart. (a) Preparation process of DSF-AgNPs composite structure; (b) fabrication process of microfluidic integrated D-shaped fiber SERS probe; (c) photograph of the fabricated sample [7]. Image © 2023 Optica Publishing Group under the terms of the Optica Open Access Publishing Agreement

formed by the nanoparticles [156]. As results shown in figure 3.9 g and h, the particles are randomly distributed, not allowing to make an assessment on the repeatability and uniformity. Considering the shape of the optical fiber, Huang Bo realized a D-shaped fiber with silver nanoparticles [7]. The preparation process of the D-shaped fiber dealt with liquid-liquid interface method (in figure 3.10 a). In particular, the silver nanoparticles (chosen with 100 nm of diameter, cause their strong LSPR response)were synthesized using a seed-mediated growth method. Then the fiber was inserted into the liquid surface with the nanoparticles (with a 45°angle) raised and dried to obtain the final structure. The D-shape fiber was prepared through plasma surface bonding. The choice of the fiber was related to the application as a multi-channel microfluidic SERS probe, as could be seen in figure 3.10 b and c. The results is involved in EF equal to $1.14{\cdot}10^9$.

To gain higher detection limit for molecule detection, Tao Li et al. proposed a tapered fiber coated by silver nanoparticles as a SERS substrate, fabricated trough a three-step process [157]. The reported study dealt with the optimization of a tapered fiber angle and the density of silver nanoparticles decorated on the fiber surface. The fabrication method has as first step the formation of the cone of the multi-modal optical fiber (with a core-cladding equal to 50-125 μm) and NA = 0.22) through the vertically immersion into the mixture of hydrofluoric acid and sunflower seed oil for the corrosion. The second step involved in the nanoparticles synthesis, according the detailed procedure described by Lee et al. [158]. The last step indeed in silver nanoparticles deposition on the tip of the corroded tapered fiber by an electrostatic adsorption method (after a pre-treatment of the fiber). From an accurate analysis emerged that the angle of the tapered fiber decrease as increase the corrosion time. In terms of SERS intensity, a tapered fiber with a small cone angle provides more active SERS regions (due to the increase in the lateral surface), allowing light to interact with more deposited nanoparticles. For a SERS probe (with a cone angle of 12deg and silver nanoparticles adsorption density of 26.67%) tested with R6G, the average enhancement factor was $5.5 \cdot 10^6$. A density cover equal to 26.67% is quiet low, considering that it is not possible to obtain a uniform layer.

In 2021 [8], Yuting Long et al. have presented a similar probe realized with Tin(II) chloride sensitization via solvothermal manufacturing process, with the difference that the end part of the fiber does not have a cone structure but a flat end face. A schematic representation of the used set-up and the sample fabricated is shown in figure 3.11. After mixing a solution containing polyvinylpyrrolidone, ethylene glycol solution of silver nitrate and sodium hydrogen carbonate, the obtained solution was poured into a Teflon autoclave (100 mL). After a process of sensitization, the optical fiber placed in the autoclave with the solution. The autoclave was sealed and heated at 413.15 K for 1 hour. Dried under Argon flow, the optical fiber probe was obtained. The fiber probe adopted was a multimodal fiber with a core diameter of 62.5 μm and cladding diameter of 125 μm. The presence of stannous ions improved the adhesion to the surface of the optical fiber end facet by the silver nanoparticles.

Figure 3.11. SERS setup for SERS optical fiber probe. The optrode configuration by using optical fiber probe adds flexibility and simplicity of SERS measurement. Excitation light and SERS signal transmit within one single optical fiber [8].

The reason why the growth rate of the silver particles is increased, generating active sites for silver to adhere to the fiber surface, causing a dense distribution and small size of the particle. In others terms, when the oxygen ions interact with the stannous ion at the optical fiber surface, the electron cloud is deformed, promoting the formation of bonding between nanoparticles to the surface of the fiber involved. The resulting substrate is quite uniform, with an EF equal $6.5 \cdot 10^5$. An year later, Attila Kohut et al. proposed the same substrate by changing the fabrication method with a single step manufacturing process [9].

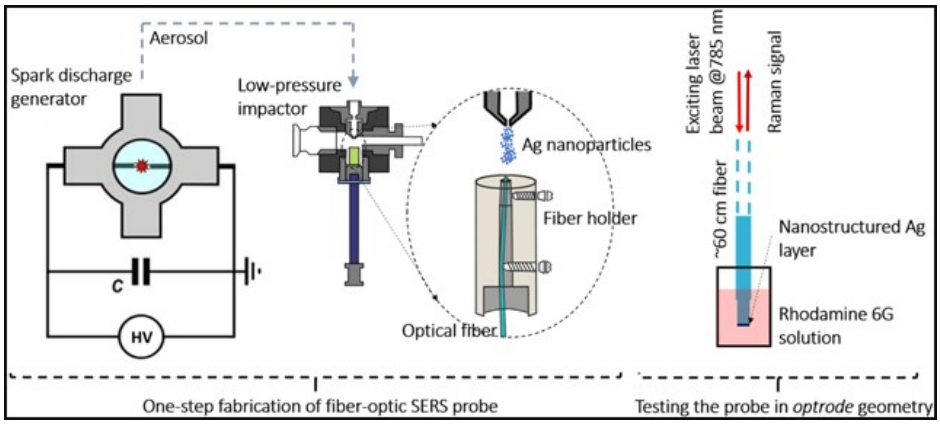

Figure 3.12. Schematic experimental setup for particle deposition and Raman measurements [9].

The substrate was realized with a spark ablation discharge nanoparticles generator (described in another work [159]), allowing the direct deposition of spark generated silver nanoparticles onto the tip of an optical fiber. The schematic experimental setup used for the fiber optic deposition is represented in figure 3.12. The study showed that the SERS intensity (of the selected peak) increases until it reaches an optimal value around 30%-40% of the transmission (when it increases), followed by a decrease. When the surface coverage of nanoparticles is low, there is an increase in transmission and a decrease in hot spots (resulting in a decrease in the SERS signal strength). At the same time, if you increase the surface coverage considerably you risk creating a layer too often that does not allow you to transmit light and then excite the surface plasmons (producing a signal SERS equally little intense). In other words, the SERS signal varies from regions with low transmission (15%)) to high transmission (50%)). The results obtained by measuring the R6G on the tip of the fiber, allowed to estimate the enhancement factor of the probe and is equal to $5 \cdot 10^4$. The manufacturing method is quite simple but provides an EF of an order of magnitude less than the SERS probe proposed by Yuting Long et al. [8]. Jang Ah Kim presents a novel fiber optic SERS probe fabricated on the tip using a simple two-step method, using standard components and materials [10].

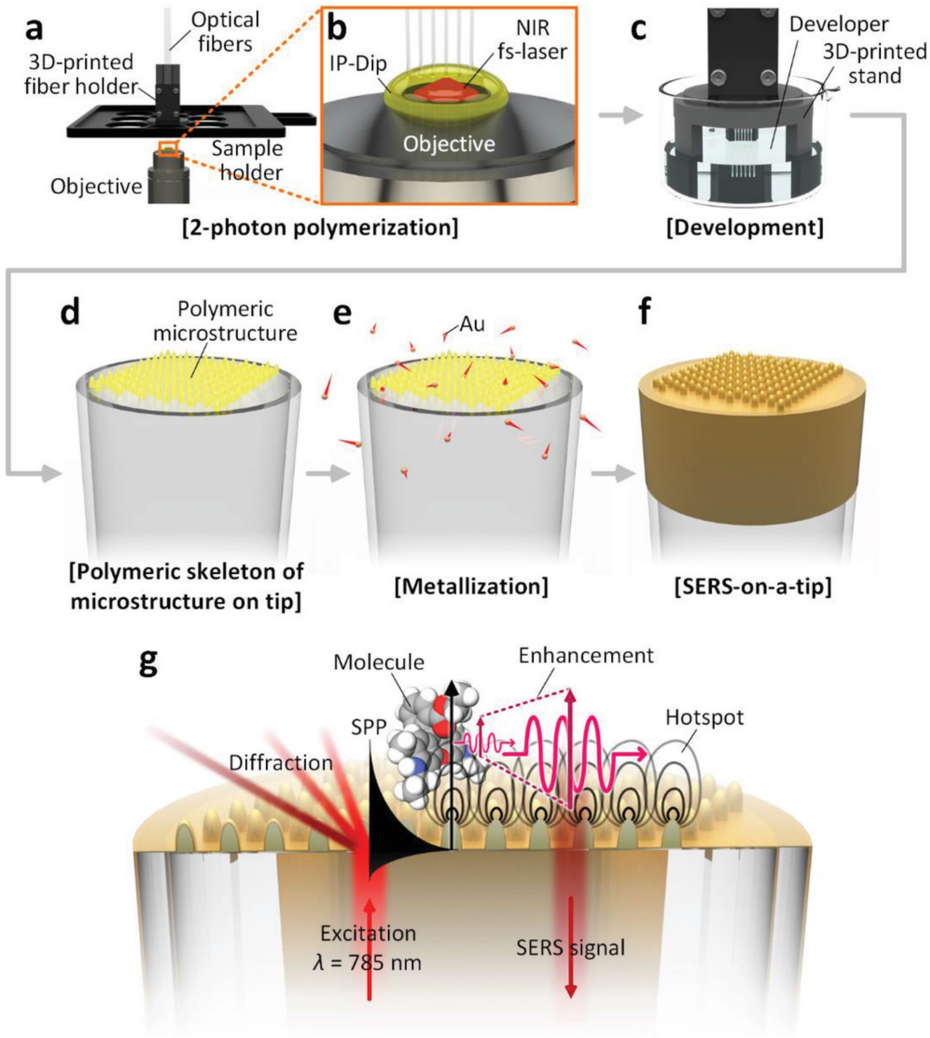

Figure 3.13. Fiber-Optic SERS Probes Fabricated Using Two-Photon Polymerization For Rapid Detection of Bacteria [10].

A wide range of arrays of both planar substrates and end facet optical fiber were fabricated. The fabrication process with the fiber optic SERS probes is outlined in figure 3.13. After a treatment of the end of the fiber (multimode silica optical fiber with 200-220 μm of core-cladding diameter, 0.22 numerical aperture), the two-photon polymerization (2PP) was used for yielding the polymeric skeleton of the array. The second step is to coat the tips of the optical fibers with a metallic layer (gold thin film of 50 nm thickness). The 2PP is a photopolymerization method, relying on non-linear two-photon absorption. This process allows to obtain high resolution additive manufacturing and is also able to provide arrays that are not fabricable with other methods. This microscale 3D printing technique has a resolution down to 300 nm in along the axial reference and 100 nm in lateral [160]. Currently, the 2PP technique gained interests by the scientific community, thanks to its many advantages (low cost and the possibility of mass production), in different application areas such as microfluidics, micro-optics and photonics [161]. Moreover, the fabrication by 2PP of small-scale substrates (i.e. microscale sensors [162]) and of sophisticated structures (i.e. miniature acoustic sensor [163]) has been successfully demonstrated. In the SERS application contest, usually, the 2PP is used to create polymeric mask or supports. Jang Ah Kim et al. with 2PP fiber probe were able to realize a probe with a high degree of controllability and repeatability. Despite the many advantages just listed, this probe presents a resulting EF pretty low and equal to $0.13 \cdot 10^4$.

The table 3.1 summarizes the main characteristics of the fiber optic SERS probes described above, for a direct comparison. The structures presented in table are some of the fiber probes made and present in the literature. Most of it has been designed for chemical sensing [152], bacteria detection [10], pesticide detection [157], antibiotics in milk [5], biomolecular detection [153] and generic molecule detection [6], [7], [157], [8], [9]. What emerges from this comparison is that it is difficult to obtain a uniform, reproducible, low-cost substrate with a high EF. In particular, therefore the realization of fiber optic SERS substrates is still widely studied. The performance and results of planar substrate fabrication are a long way off. The realization of SERS fiber optic probes has, without any doubt, purely application advantages but with an increase in performance losses.

Table 3.1. Counterpoint between the fundamental characteristics of the SERS fiber optic substrates presented.

Fabrication Method	Material	Raman reporter	EF	Ref.
Self-assembly	Gold	4-ATP	$3.50 \cdot 10^4$	[152]
Self-assembly	Gold	BPT	$4.00 \cdot 10^4$	[153]
Sol self assembly	Silver	R6G	$1.36 \cdot 10^8$	[5]
Growth method	Gold&silver	R6G	$2.54 \cdot 10^7$	[155]
Chemical reduction	Gold	Crystal violet	$1.02 \cdot 10^8$	[6]
Liquid-liquid interface	Silver	R6G	$1.14 \cdot 10^9$	[7]
Electrostatic adsorption	Silver	R6G	$5.50 \cdot 10^6$	[157]
Solvothermal	Silver	R6G	$6.50 \cdot 10^5$	[8]
Spark Ablation	Silver	R6G	$5.00 \cdot 10^4$	[9]
2PP	Gold	R6G	$0.13 \cdot 10^4$	[10]

To conclude, a state-of-the-art overview of SERS planar and fiber optic substrates was provided. A substrate to be highly performance must be homogeneous (also ensuring stability) and above all must have numerous and understood locations of electromagnetic field. To achieve this goal it is necessary to have a structure with tips or small nanogaps. By appropriately engineering the architecture, considering extending the geometry in more dimensions by creating complex hierarchical structures, it is possible to significantly increase the spatial density and intensity of the hot spots. In parallel, the choice of material plays a fairly important role. Gold is the most widely used plasmonic material due to its low electronic losses and bio-compatibility. Silver is another material that allows to obtain substrates with high performance, but limits the applications due to the lack of bio-compatibility. As has been observed, a substrate that is homogeneous is difficult to obtain if not involving fabrication techniques with long times and high costs. In this context fits the self-assembly approach that allows you to obtain complex structures, overcoming the limits of other techniques (costs and manufacturing times), by realizing hierarchical substrates. Over the years, numerous advances have been made in the field of fiber optic SERS probes. Despite this, the performance obtained with planar substrates is certainly higher than those in fiber optics.

Chapter 4

Design of hierarchical structures as SERS substrate

The proposed device comes from the integration of a substrate with a hexagonal hierarchy of nanospheres on the tip of an optical fiber, through self-assembly fabrication. The self- assembly technique allows the realization of a planar substrate to be transferred to a fiber substrate. In this case, the structure is analyzed from an exclusively planar point of view. In particular the substrate consists of a uniform layer of hexagonal symmetrically packed nano spheres (HSN), within the intersection spaces between the spheres are placed upper spheres, reduced in size. A layer of gold is deposited above the substrate. In this chapter, the numerical simulations of the structure will be illustrated, from an electromagnetic point of view, whit aim of for the designing and optimizing the geometrical parameters. The simulations are done via the commercially available numerical simulator: "Comsol multi-physics" [164]. Consequently, the main geometrical parameters that affect the configuration of the HSN substrate are: the diameter of the D_B nanospheres and the diameter, D_U, of the (smaller) nanospheres located on the top, between the bottom nanospheres. In the next paragraph we will describe the details of the model used and the complete results obtained. In order to obtain an effective performance analysis, the individual HSN structures were compared with a simpler structure. This structure is a closed packed array with hexagonal symmetry (CPA), analogous to HSN structures with the difference that it consists of a single

layer of nanospheres. The chapter is divided into two main paragraphs. The first paragraph adequately describe the model used: the boundary conditions, materials, mesh and includes the electromagnetic description used. The second paragraph focuses on showing the results obtained by simulating a complete analysis. In detail, the analysis involves three diameters of the bottom nanospheres, which are: 500 nm,750 nm and 1000 nm. For the above bottom diameters, the respectively diameters of the upper spheres are varied for values of δ corresponding to the range from $\delta = 0.24$ to $\delta = 0.56$. The δ ratio is defined as $\delta = D_U/D_B$,in other words is the ratio between the diameter of the upper spheres and the diameter of the bottom spheres. For comparison, therefore the CPA has been simulated for diameters equal to bottom spheres (500 nm,750 nm and 1000 nm). The wavelength range of interest is from 600 nm to 1200 nm, taking in mind that the fingerprint region goes from 785 to 910 nm.

4.1 Numerical model design

The proposed device was numerically analyzed by modelling the structure using the commercial software Comsol Multyphisics, based on the finite element method (FEM). The FEM method is a numerical technique to look for approximate solutions of problems described by partial differential equations by reducing the latter to a system of algebraic equations. In general, the finite element method is well suited to solving partial derivative equations when the domain has complex, variable, non-homogeneous form and/or when it lacks regularity. The electromagnetic numerical model of the structure is simulated through the "radio frequency" module of Comsol, by using the following equations:

$$\nabla \times \mu_r^{-1}(\nabla \times E) - k_0^2 \left(\epsilon_r - \frac{j\sigma}{\omega\epsilon_0}\right) E \tag{4.1}$$

$$\nabla \times (\nabla \times E) - k_0^2 \epsilon_r E = 0 \tag{4.2}$$

$$\epsilon_r = (n - ik)^2 \tag{4.3}$$

The simulated structure is in 3-D where, exploiting the symmetry of the system, it was possible to reduce the computational domain to the unit cell.

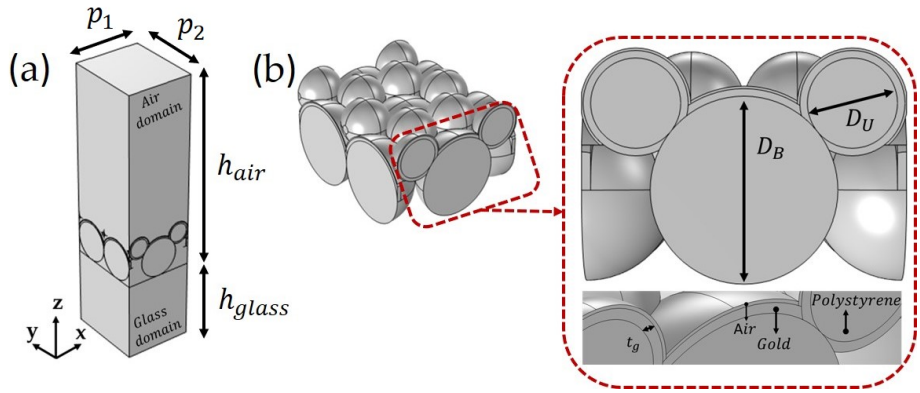

Figure 4.1. (a) Computational domain of the unit cell simulated; (b) Different side view of the substrate with specified the reference quantities

Reducing the structure to a single unit cell, not only does not make the results fallacious but also simplifies the structure, making the simulations inexpensive from the computational point of view and the time spent. In figure 4.1a-b, the rectangular unit cell is shown and it is composed by a centred sphere placed in the origin, enclosed by truncated spheres in half (bottom spheres). In the intersection sites between the bottom spheres is placed a second layer of spheres (upper spheres), reduced in size. The external upper spheres are truncated accordingly to bottom spheres. A conformal layer to the outer surface of the gold domain is made, consisting of air. This layer was created with the aim of evaluating the electromagnetic field diffused in it. In figure 4.1 is shown the conformal layer, and it is possible to observe that the layer follow the shape of the gold domain. The conformal layer was placed with a thickness of 10 nm, whereas the SERS effect takes place on the outer surface of the gold layer and decays exponentially. Both the upper and bottom nanospheres are made of polystyrene and covered with a 30 nm thick layer (called t_g) of gold. The HSN is placed on a slice made of glass. Along the positive z axis, the air domain is extended from the hierarchical binary structures up to four times the big sphere diameter (i.e h_{air}). In parallel along the negative z axis, the glass domain is set to the period of the unit cell (i.e h_{glass}).

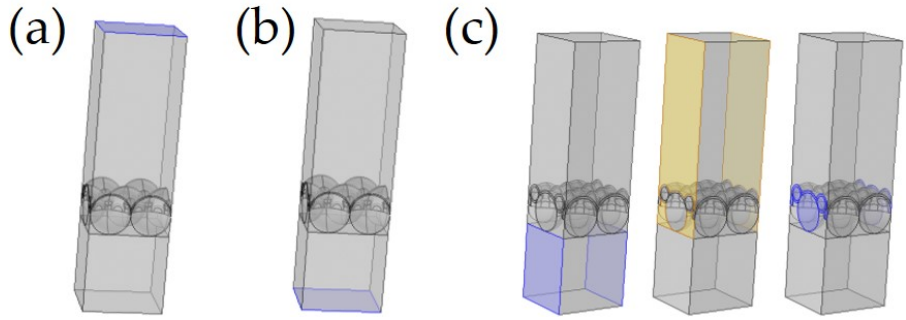

Figure 4.2. Periodic condition applied: (a) Source, (b) Receiver, (c) Floquet's condition.

For both domains, the lateral dimensions are respectively equal to $p_1 = \tan(\pi/3) \cdot D_B$ and $p_2 = 2D_B$ (figure 4.1 a). For each domain was set the refractive index to define the material. The refractive index of the gold is taken from the data set made available from Johnson and Christy [165]. All the refractive index of the materials used and the dimensions of each domains are listed in the table 4.1. On the top of the structure is set the active port condition (source: figure 4.2 a) and on the bottom the passive port condition (receiver: figure 4.2 b). In the source port, the incident field is modeled as a linear polarized plane wave along x (with a power of 1 Watt) and the port is defined as "periodic" with diffracted order calculation enabled. The Floquet's periodic condition was applied and placed two by two on the opposite side walls of the structure for each domain (air, gold + polystyrene and glass). In figures 4.2 c it is possible to see the Floquet's conditions applied, setting for each domain the respectively wave vectors.

Table 4.1. The refractive index and thickness of the materials used.

Material	Thickness-height	Refractive index
Air	$5 \cdot D_B$	1
Gold	30 nm	P. B. Johnson and R. W. Christy [165]
Polystyrene	$D_B or D_U$	1.6
Glass	$2.5 \cdot D_B$	1.45

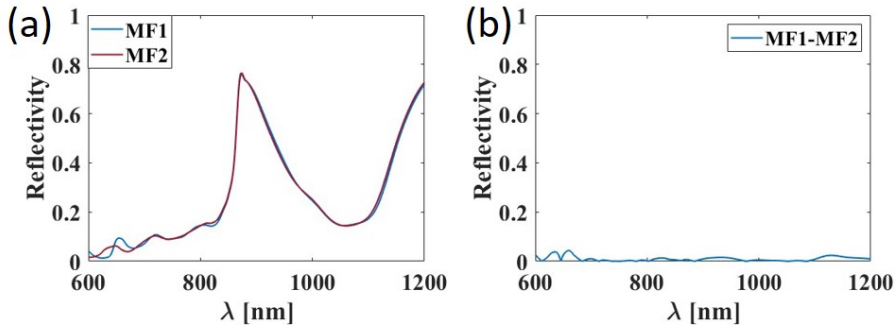

Figure 4.3. (a)Reflectivity spectrum obtained for MF1 and MF2, (b) Reflectivity difference between MF1 and MF2

This condition allows to replicate infinitely the unit cell in all direction. Floquet's periodicity is mainly used for frequency domain problems for structure with spatial periodicity of geometry and solution. Using the following equations, the Floquet's boundary condition is defined as:

$$E_{dst} = E_{src} e^{ik_f(r_{dst} - r_{src})} \tag{4.4}$$

Where E_{dst} and E_{src} are the electromagnetic field for the destination and source, respectively. Free triangular mesh is set for the boundary domain, instead for the remain domain is set the tetrahedral mesh. To have a stable model and not affected by the mesh, a series of simulations were made by varying the mesh. In particular, two meshes were compared on a structure with a bottom sphere radius equal to 1000 nm and an upper sphere radius equal to 240 nm. The first mesh (MF1) has a maximum element size of 100 nm, while the second mesh (MF2) has a maximum size of 120 nm. In figures 4.3, the reflectivities are shown, compared to the two meshes considered and in figures, you can see the difference between the two reflectivities to highlight possible variations. The displacement between the two reflectivities has a value less than 0.035. It is allowed to proceed using the MF2. The mesh has not been completed since the differences between the meshes analysed were negligible, moreover the single simulation takes more than 24 hours to carry out an analysis considering 60 solutions.

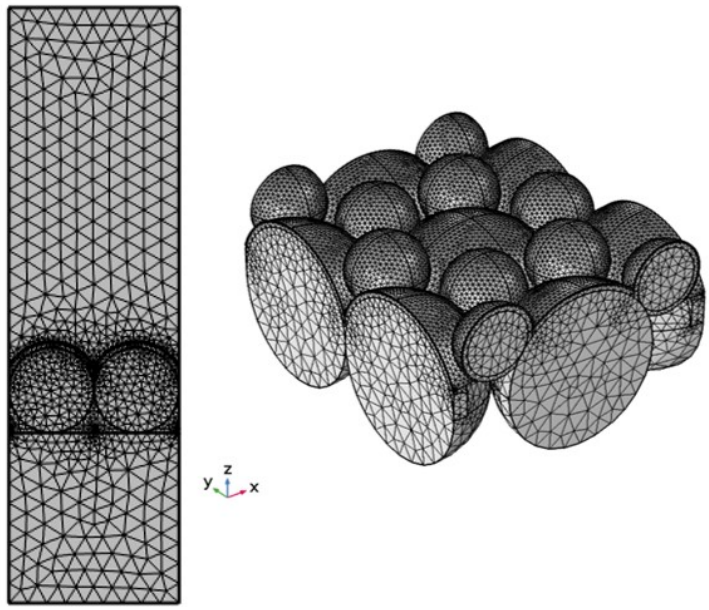

Figure 4.4. Representative mesh of the binary structure

In other words, simulating the wavelength range from 600 nm to 1200 nm with 10 nm pitch with MF2 for a structure (fixed diameters) takes 24 to 48 hours (depending on the diameter chosen). In figure 4.4, it is possible to see the MF2 used during the following simulations. Both the dimensions of the domains (of air and glass) dimensions were chosen in such a way that they did not affect the system response (following a preliminary analysis, aimed precisely at ensuring the stability of the system to the variation of the nanospheres sizes). As described previously in the introduction, the simulations performed were evaluated in terms of the fourth power volume integral of the ratio of the local field to the incident field. The incident field (E_0) was calculated using two methods: analytical and numerical, for a confirmation of the actual value. Whereas in the simulations an incident plane wave with a relative power of 1 W is set. The actual power considered by the simulator is equal to the relative power divided by a factor of 4, in other words is equal to 0.25 W.

Therefore, considering that the power density is proportional to the incident field, the following relationship is obtained:

$$D = \frac{\epsilon_0 \cdot c \cdot E_0^2}{2} \quad \Leftrightarrow \quad E_0 = \sqrt{\frac{2 \cdot D}{\epsilon_0 \cdot c}} \tag{4.5}$$

Where ϵ_0 is the dielectric constant of vacuum, c is the speed of light in vacuum and D is the power density. The power density is calculated as follow:

$$D = \frac{P_{in}/4}{A_b} \tag{4.6}$$

Keeping in mind the figure 4.1 a, the surface area A_b corresponds to the base area defined as the product between the two sides of the port (p_1 and p_2). The quantity P_{in} is the power input, divided by a factor 4 to make a comparison with the numerical calculation (since the effective power that is generated by the port in Comsol is exactly the power input divided by 4). Under this consideration the power density is:

$$D = \frac{0.25W}{8.66 \cdot 10^{-13} m^2} = 2.887 \cdot 10^{11} W/m^2 \tag{4.7}$$

By the analytical method, consequently the incident field was found to be equal to:

$$E_0 = \sqrt{\frac{2 \cdot D}{\epsilon_0 \cdot c}} \approx \ 1.47 \cdot 10^7 \ \frac{V}{m} \tag{4.8}$$

To be sure of the value used, at the same time the numerical method simulated a structure with the same previous conditions in the absence of the substrate (in the absence of the spheres and the gold layer) was used. Along a cut line the average value of the field has been calculated. The cut line extended from one port to another (from the source to the receiver), crossing the entire computational domain. The incident field using this method turned out to be $E_0 \approx 1.47 \cdot 10^7 V/m$. Whereas the two methods converged, in subsequent simulations for the relationship with the local field (for the calculation of the volume integral) is considered $E_0 = 1.47 \cdot 10^7 V/m$. The light source is a linear x-polarized plane wave that propagates in air and incident orthogonally to the HSN.

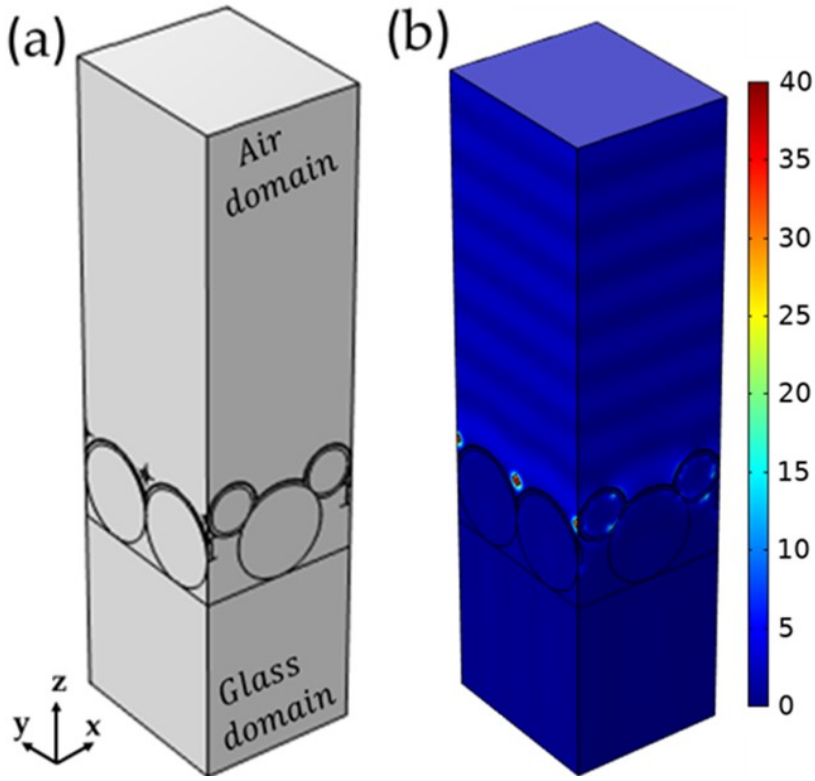

Figure 4.5. (a) Computation domain for a periodic HSNs (b) Electromagnetic field distribution normalized to the incident light intensity.

Numerical analysis provides the total electromagnetic field E_{TOT} in the range of wavelengths of interest. The figure 4.5b shows the distribution of the total electric field normalized to the incident electric field E_0 for the wavelength $\lambda = 785$ nm, considering the reference structure having D_B= 750 nm, D_U= 360 nm, t_g= 30 nm. From the point of view of the SERS signal, the total field distribution in the computation domain is irrelevant. However, it is interesting to note that the electromagnetic field distribution is the plane wave, which propagates along the z-axis causing a local perturbation at the interface with the HSN.

In fact, considering an active SERS substrate, the iteration originating the SERS signal, between the target molecule and the substrate itself takes place only near the metal surface. Three set of simulation are performed, considering the diameter of the bottom spheres equal to $D_B = 500$ nm, $D_B = 750$ nm, and $D_B = 1000$ nm. Once the diameter of the bottom spheres is fixed, the upper diameter D_U is varied keeping the ratio (δ) between the two diameter in the range: $\delta = [0.24 : 0.4 : 0.56]$. In the table 4.2 are presented the diameter of the upper spheres for each set.

Table 4.2. Diameter of spheres simulated with the respectively s.

$D_B = 500$ nm		$D_B = 750$ nm		$D_B = 1000$ nm	
δ	D_U	δ	D_U	δ	D_U
0.24	120 nm	0.24	180 nm	0.24	240 nm
0.28	140 nm	0.28	210 nm	0.28	280 nm
0.32	160 nm	0.32	240 nm	0.32	320 nm
0.36	180 nm	0.36	270 nm	0.36	360 nm
0.40	200 nm	0.40	300 nm	0.40	400 nm
0.44	220 nm	0.44	330 nm	0.44	440 nm
0.48	240 nm	0.48	360 nm	0.48	480 nm
0.52	260 nm	0.52	390 nm	0.52	520 nm
0.56	280 nm	0.56	420 nm	0.56	560 nm

4.2 Numerical results analysis

This section presents the results obtained by simulating the structures listed in the table 4.2. In figure 4.6 are presented the reflectivity spectrum of the three set of simulation performed. In figure 4.6 a-c are showed the reflectivity spectrum for $D_B = 500$ nm with $\delta = [0.24 : 0.4 : 0.50]$. Meanwhile, the reflectivity is presented in figure 4.6d-f for $D_B = 750$ nm with $\delta = [0.24 : 0.4 : 0.50]$ and, in figure 4.6 g-i for $D_B = 1000$ nm with $\delta = [0.24 : 0.4 : 0.50]$.

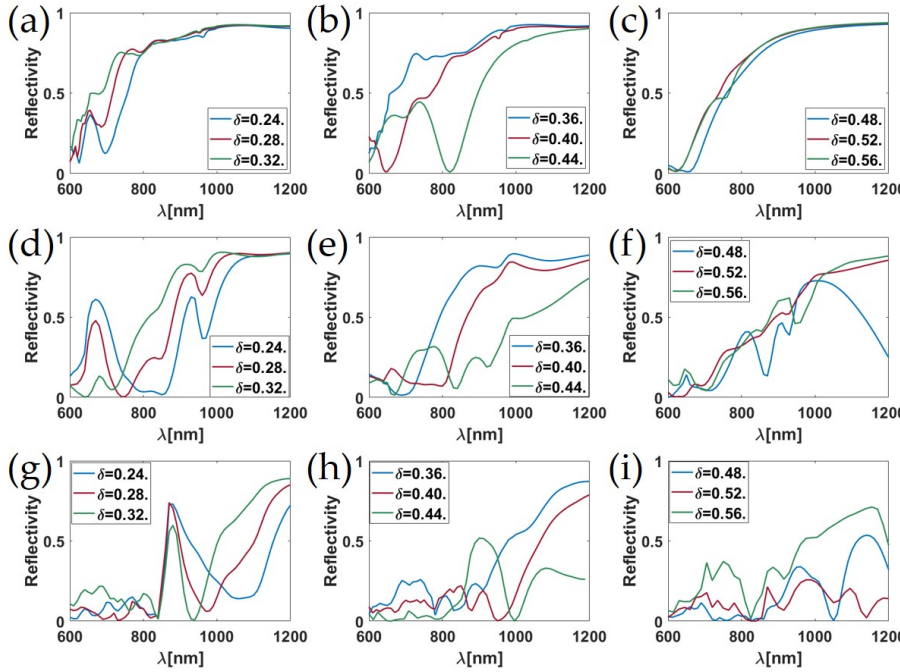

Figure 4.6. Reflectivity spectrum for: a) $D_B = 500$ nm with $\delta = [0.24 : 0.4 : 0.32]$, b) $D_B = 500$ nm with $\delta = [0.36 : 0.4 : 0.44]$, c) $D_B = 500$ nm with $\delta = [0.48 : 0.4 : 0.56]$, d) $D_B = 750$ nm with $\delta = [0.24 : 0.4 : 0.32]$, e) $D_B = 750$ nm with $\delta = [0.36 : 0.4 : 0.44]$, f) $D_B = 750$ nm with $\delta = [0.48 : 0.4 : 0.56]$, g) $D_B = 1000$ nm with $\delta = [0.24 : 0.4 : 0.32]$, h) $D_B = 1000$ nm with $\delta = [0.36 : 0.4 : 0.44]$, i) $D_B = 1000$ nm with $\delta = [0.48 : 0.4 : 0.56]$.

Increasing the ratio between the spheres, considering the figure 4.6 a, d and g the maximum peak present in the spectrum undergo a slight left shift, lowering the intensity. Observing the figure 4.6 b, e and h the opposite phenomenon occurs, the spectrum undergoes a shift towards high wavelengths and at the same time the maximum peak disappears. Increasing δ, the upper spheres grew and begin to make their influence felt, due to the comparable size with the bottom spheres. It is possible to observe this mechanism in the figure 4.6 c,f and i. The figure 4.6 a to c, d to f and g to i, shown that the maximum peak of reflectivity exhibits a shift to high wavelength, when the radius of the bottom spheres is increased.

To compare the performance of the different structures, a figure of merit is considered. This figure of merit provides an estimate of the wavelengths at which the best SERS performance is expected. The figure of merit chosen is the volume integral (VI). Considering that the field decreases rapidly away from the surface of the nanostructure [38], to estimate the amplitude of the generated SERS signal, only the field diffused within 10 nm from the surface of the HSN is considered and the volume integral (VI) is calculated on a 10-nm thickness conformal layer overlap on gold layer, of the following quantity:

$$VI = \iiint_V \left| \frac{E_{TOT}}{E_0} \right|^4 dV \tag{4.9}$$

Where E_{TOT} is the local electromagnetic field and E_0 is the incident field. The volume integral (VI) takes into account all and the various contributions generated by the individual hot spots between the nanospheres. The VI provides information on the enhancement of the magnetic field and therefore of the corresponding SERS signal generated by the HSN substrate, in the spectral range of interest. The VI was calculated for each substrate analysed.

Actually, the numerical model (as well as the volume integral) was already adopted in the work from Managò et al. [26], which analyzed the simple CPA structure and compared the results with the experimental data. The same CPA is used in this work as a reference to the binary hierarchical structure. Analysing the volume integral shown in figure 4.7, the best performances are obtained for δ equal to 0.44, δ equal to 0.48, and δ equal to 0.52 respectively for each set: D_B=500 nm, D_U=750 nm and D_B=1000 nm. As the diameter of the bottom spheres increases, the maximum peak decreases and moves to a greater wavelength. The fact that the peak maximum is obtained in a configuration in which the upper spheres assume a size that is comparable to the large ones, is mainly due to the increase in the number of hot spots, present in the substrate. In order to carry out an accurate performance analysis for each simulated spheres diameter, for each volume integral two fundamental parameters have been extrapolated : the maximum value and the average value.

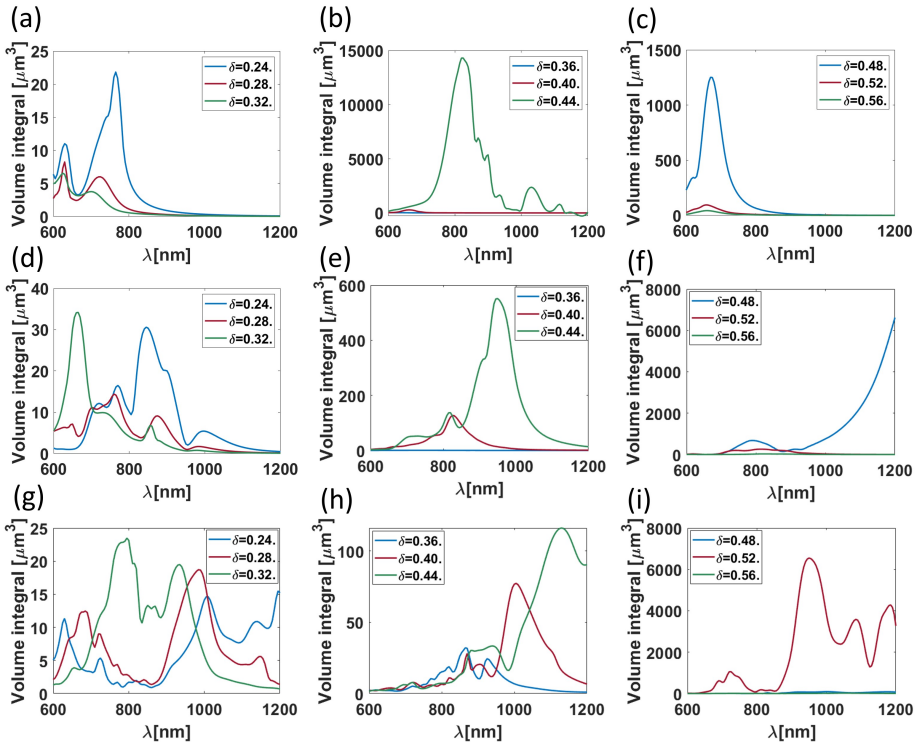

Figure 4.7. Volume integral for: a) $D_B = 500$ nm with $\delta = [0.24 : 0.4 : 0.32]$, b) $D_B = 500$ nm with $\delta = [0.36 : 0.4 : 0.44]$, c) $D_B = 500$ nm with $\delta = [0.48 : 0.4 : 0.56]$, d) $D_B = 750$ nm with $\delta = [0.24 : 0.4 : 0.32]$, e) $D_B = 750$ nm with $\delta = [0.36 : 0.4 : 0.44]$, f) $D_B = 750$ nm with $\delta = [0.48 : 0.4 : 0.56]$, g) $D_B = 1000$ nm with $\delta = [0.24 : 0.4 : 0.32]$, h) $D_B = 1000$ nm with $\delta = [0.36 : 0.4 : 0.44]$, i) $D_B = 1000$ nm with $\delta = [0.48 : 0.4 : 0.56]$.

The average estimation of the volume integral (AVI) has been calculated in the wavelength range from 785 nm to 910 nm. If we take as a reference the response of the BPT (as Raman reporter), the range has been chosen in such a way that the peaks relative to the Raman shift (which occurred approximately between 1080 and 1600 cm^{-1}) are included in the range of wavelengths considered. The maximum volume integral (MVI) was evaluated across the simulated wavelength range.

Table 4.3. Numerical results for CPA.

D_B $[nm]$	MVI $[\mu m^3]$	AVI $[\mu m^3]$
500	517.59	485.96
750	39.40	21.40
1000	21.42	2.89

For each substrate, the value of MVI and AVI, has been compared to the respective value of CPA. The relative values of CPA are present in the table 4.3. Increasing the size, both the MVI and the AVI decrease. The MVI changes from a value of $\approx 518\ \mu m^3$ to $\approx 21\ \mu m^3$ (respectively for D_B=500 nm and D_B=1000 nm). Likewise, the AVI is reduced by a factor of 48 (from D_B=500 nm to D_B=1000 nm). The fundamental results obtained for hierarchical substrates are summarized in the table 4.4. In particular as said previously, the parametric analysis respect to MVI and AVI reveals that the optimal structure is obtained for δ equal to 0.44,δ equal to 0.48, and δ equal to 0.52 respectively for each set: D_B=500 nm, D_U=750 nm and D_B=1000 nm. Considering the table 4.4, the size increasing of the large spheres produces a decrease in terms of MVI, at the same time working with too small spheres does not allow to fabricate uniform and stable substrates. In particular, the substrate with $D_B = 500$ nm and δ equal to 0.44 has a maximum value of the volume integral compared to the CPA of about 27 times higher than the CPA, while the structure with $D_B = 750$ nm and $\delta = 0.48$, about 167 and that with $D_B = 1000$ nm and $\delta = 0.56$ about 654. The analysis of the MVI values shows that by increasing the diameter of the upper spheres the performance increases significantly. Compared to CPA, the structure with $D_B = 750$ nm and $\delta = 0.48$, has a value of about 6 times higher than the structure with $D_B = 500$ nm and $\delta = 0.40$ and 1.8 less than the structure with $D_B = 1000$ nm and $\delta = 0.52$. In terms of AVI, the structure with $D_B = 500$ nm has a very low value of less than $\approx 4\ \mu m^3$, except for the structure with $\delta = 0.44$ wih a value of about 3138 μm^3. For substrates with $D_B = 750$ nm and δ values between 0.40 and 0.56, the AVI values increase from 73 to 400 μm^3.

Table 4.4. Numerical results for each diameter.

D_B $[nm]$	δ	MVI $[10^{-17}]$	$\frac{MVI_{HSN}}{MVI_{CPA}}$	AVI $[10^{-17}]$	$\frac{AVI_{HSN}}{AVI_{CPA}}$
500	0.24	21.000	0.041	3.270	0.006
500	0.28	8.250	0.015	0.710	0.001
500	0.32	6.370	0.012	0.410	0.001
500	0.36	24.550	0.047	0.880	0.002
500	0.40	279.880	0.541	6.320	0.013
500	0.44	14302.200	27.632	3138.900	6.459
500	0.48	1251.710	2.418	38.680	0.079
500	0.52	95.050	0.183	6.070	0.012
500	0.56	43.410	0.083	3.310	0.006
750	0.24	30.580	0.775	16.000	0.760
750	0.28	14.390	0.365	06.500	0.306
750	0.32	34.080	0.864	37.000	0.173
750	0.36	0.650	0.016	3.600	0.016
750	0.40	126.400	3.204	73.000	3.431
750	0.44	551.080	13.970	150.000	7.008
750	0.48	6621.900	167.877	400.000	19.086
750	0.52	260.330	6.599	210.000	9.943
750	0.56	32.650	0.827	260.000	1.223
1000	0.24	15.500	0.723	1.680	0.58
1000	0.28	18.710	0.873	2.880	0.976
1000	0.32	23.470	1.095	15.970	5.529
1000	0.36	32.110	1.499	18.180	6.293
1000	0.40	77.300	3.608	13.630	4.718
1000	0.44	116.120	5.420	16.420	5.682
1000	0.48	95.690	4.467	23.490	8.132
1000	0.52	6546.800	305.612	851.450	294.683
1000	0.56	23.230	1.084	5.150	1.783

For this type of substrate the values of AVI, generally are elevated, with differences respect the other structures that introduces a high peak for a single structure and extremely low values for the others.

For example, the structures with $D_B = 1000$ nm have (as for structures with $D_B = 500$ nm) a maximum peak of AVI (for $\delta = 0.52$) equal to 851 μm^3, twice times the previous structure, but for other delta values the AVI is lower than a value of 20 μm^3. From this analysis emerges that the upper nanospheres play an important role. As the diameters of the upper nanospheres increase, they form an additional model of packed nanospheres, which in turn generate hot spots at the point of contact between the nanospheres. Furthermore, additional nano-gaps that form between the upper nanospheres create hot spots, increased in number and in tems of intensity. When the upper nanospheres have a small diameter, occurs that they do not interact with each other and therefore have a negligible contribution to the overall enhancement of the electromagnetic field. This is why it is important to take into account the presence of nano-gaps due to upper nanospheres in the analysis to improve substrate performance. Based on geometric considerations, it is possible to estimate the expected separation between the upper nanospheres and when they are in contact. For the geometric construction, the upper nanospheres are located precisely in the orthocenters of the triangle, formed by the bottom spheres. The triangle is constructed by considering the vertices in the centers of three adjacent bottom nanospheres. Taking the figure 4.8 as a reference, the points lines represent two triangles having vertices in the center of the bottom nanospheres, represented in the figure as blue blank spheres, while the light green nano-spheres are the upper spheres. The bold line represents the heights of the triangles, whose intersection gives origin to orthocenters, consequently the reds dots represent the respective orthocenters O_1 and O_2. The distance between the two adjacent orthocenters (O_1 and O_2) is equal to:

$$\overline{O_1O_2} = \frac{\sqrt{3} \cdot D_B}{3} \tag{4.10}$$

At this point it is easy to estimate the separation, called "s", between the upper spheres both when in contact and when they are simply adjacent. Taking into account the diameter of the bottom nanospheres (D_B), the upper nanospheres D_U and the thickness of the gold layer (t_g),

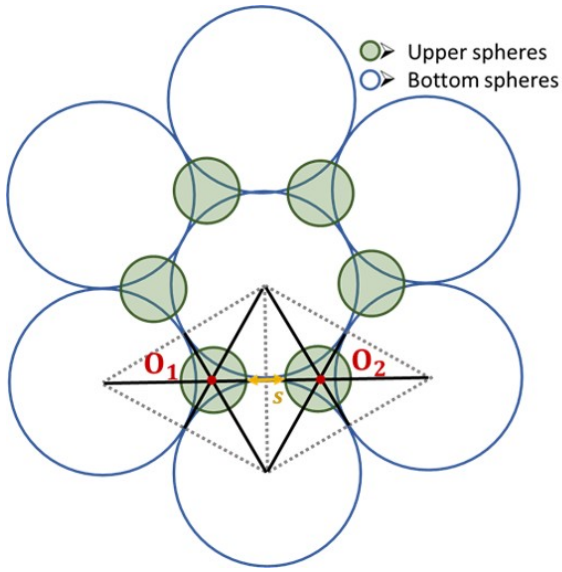

Figure 4.8. 2D schematic representation of the geometric construction of orthocenters (O_1 and O_2) and the separation (s), between two adjacent upper nanospheres

the separation cloud be calculated as follow:

$$s = \frac{\sqrt{3} \cdot D_B}{3} - D_U - 2t_g \tag{4.11}$$

Of course, for negative values of s, the upper spheres are in contact with each other (e.g. for $\delta \leq \sqrt{3}/3 \approx 0.577$); while for values of $\delta \approx 0.577$, the upper spheres cannot position themselves in the orthocenters. In the table 4.5 are listed the corresponding value of "s" for each substrate analysed. The best performance comes from structures with geometrical parameters: $D_B = 500$ nm with $\delta = 0.44$, $D_B = 750$ nm with $\delta = 0.48$ and $D_B = 1000$ nm with $\delta = 0.52$. Considering the observation made about the separation "s" and the relative gaps, it is interesting to note that the performance improve when the upper spheres are approaching. In fact, the structures with the best performance, correspond to the substrates with minor gaps. This occurs except for structures with bottom spheres diameter equal to $D_B = 1000$ nm, where the best substrate has upper spheres directly in

Table 4.5. Diameter of spheres simulated with the respectively s.

$D_B = 500$ nm		$D_B = 750$ nm		$D_B = 1000$ nm	
δ	s	δ	s	δ	s
0.24	109	0.24	193	0.24	277
0.28	89	0.28	163	0.28	237
0.32	69	0.32	133	0.32	197
0.36	49	0.36	103	0.36	157
0.40	29	0.40	73	0.40	117
0.44	9	0.44	43	0.44	77
0.48	contact	0.48	13	0.48	37
0.52	contact	0.52	contact	0.52	contact
0.56	contact	0.56	contact	0.56	contact

contact. As proof of the above concept, in figure 4.9 a-b, the reflectivity and volume integral (VI) calculated for two HSN substrates, exhibiting different ratios (δ) between diameters, are shown. In particular, we consider two structures with a bottom diameter of 750 nm and upper diameter of 210 nm and 330 nm (with $\delta = 0.28$ and $\delta = 0.44$ respectively). The two structures show a similar trend in terms of reflectivity, despite the volume integrals are pretty different. In fact, the structure with $\delta = 0.44$ has a volume integral ($VI \approx 10^{-16}$) of an order of magnitude greater than the substrate with $\delta = 0.28$ ($VI \approx 10^{-17}$). The highest value of the integral volume is generated directly by the "hot spots", present between the nanogaps between the adjacent nanospheres. Considering a cutting plane along the x and y axes, in figure 4.9 c-d, the maps relative to the distribution of the electromagnetic field are reported. To easily highlight the improvement in order of magnitude of the total electromagnetic field with respect to the incident plane wave, the field distribution is represented in terms of $\log\left(|E_{TOT}/E_0|\right)^4$, at two wavelengths: $\lambda = 785$ nm and $\lambda = 900$ nm. Assuming the incident wavelength is 785 nm, the spectral range associated with the region of the Raman fingerprint of interest (i.e the regions lower than $1800 cm^{-1}$) corresponds approximately to the range from 785 nm to 915 nm. Considering the figure 4.9 c-d, it is interesting to note how the plane wave is able to excite the surface plasmons, generating hot spots between the intersections between the nanospheres.

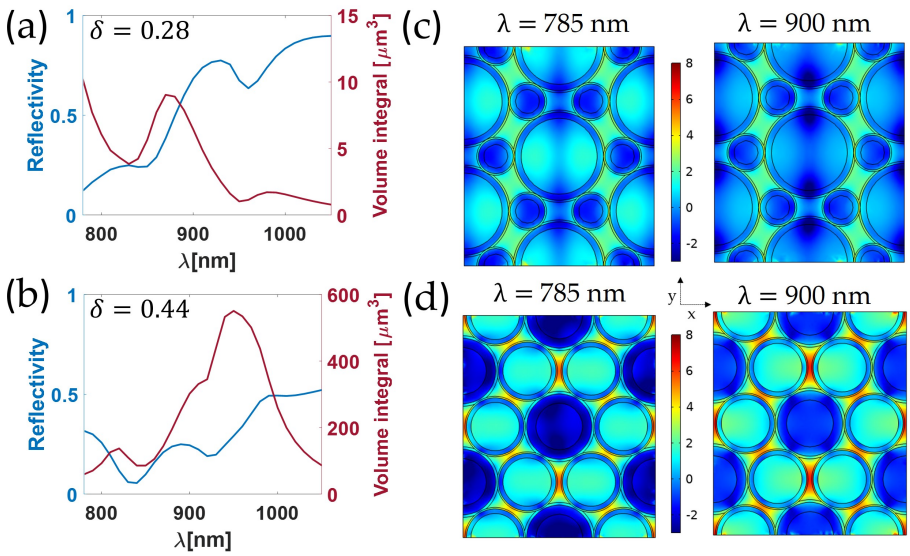

Figure 4.9. (a-b) Reflectivity and volume integral on the 10nm conformal air overlay of the forth power of the normalized electric field; (c-d) electromagnetic field distribution normalized to the incident light intensity along the xy cut plane

In particular in figure 4.9 c, it is possible to notice that the upper spheres do not give an effective contribution in the generation of the hot spots, created exclusively by the bottom nanospheres. In contrast, in figure 4.9 d, HSN exhibits a higher number of hot spots. The reason why is that the superior nanospheres contribute to the global enhancement by forming new hot spots, located in the intersections between the upper and lower spheres. So always looking at the figure 4.9 c-d, it's clear that the configuration with $\delta = 0.44$ provides an effective enhancement in both intensity and number of hot spots. Increasing the values of δ does not necessarily represent an improvement compared to the simplest configuration, in fact there is not always an improvement in performance. This analysis further confirms the generic analysis carried out above, highlighting some differences between structures. To complete the analysis, two simulations varying the polarization were made for a substrate with $D_B = 750$ nm and $\delta = 0.28$ and 0.44.

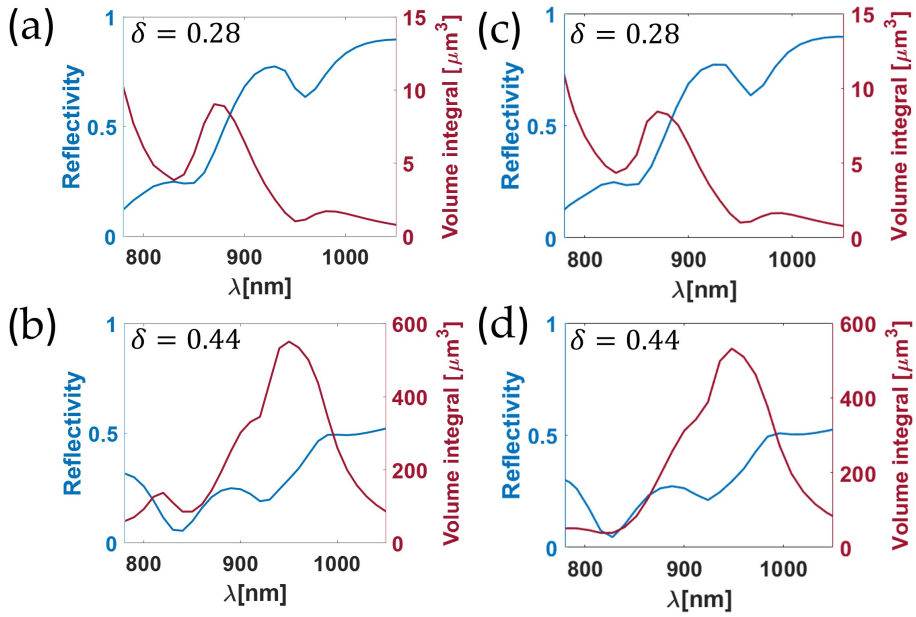

Figure 4.10. Reflectivity and volume integral for (a) $D_B = 750nm, \delta = 0.28$ and polarization along x, (b) $D_B = 750nm, \delta = 0.44$ and polarization along x, (c) $D_B = 750nm, \delta = 0.28$ and polarization along y, (d) $D_B = 750nm, \delta = 0.44$ and polarization along y.

The chosen polarization does not affect the main results of the reported numerical analysis. The resulting volume integrals for both polarizations are very similar. Specifically, we observed that different polarizations excite a different hotspot distribution, but the intensity and number of hotspots remains the same. The above simulations and their results have been obtained by spreading the substrate with a plane wave polarized along x . By changing polarization from x to y, great differences in the obtained results are not so evident. The figure 4.10 shows the volume integrals and reflectivity for the two substrates examined. In particular, in the figure 4.10a and c are taken the results obtained for a structure with bottom spheres diameter of 750 nm and upper diameter of 210 nm (with $\delta = 0.28$), respectively under polarization x and y.

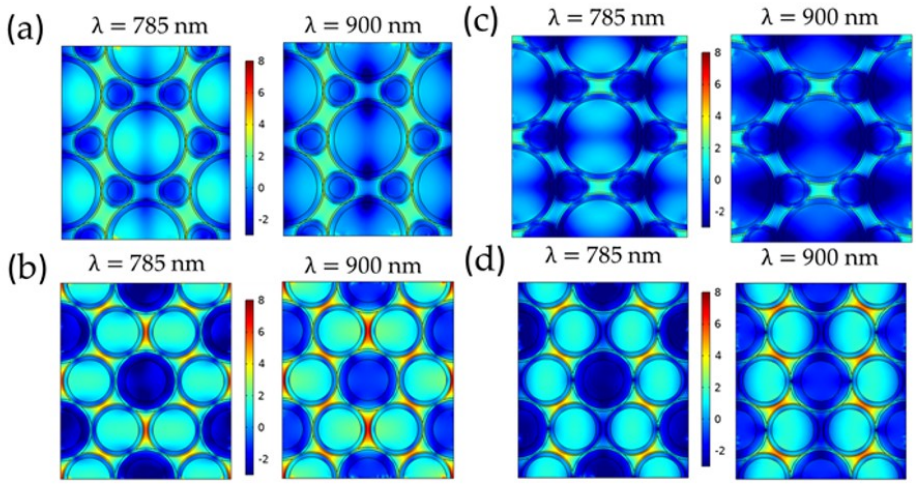

Figure 4.11. The electromagnetic field distribution, in terms of $\log_{10}(|E_{TOT}/E_0|^4)$ for: (a-b) $D_B = 757nm, \delta = 0.28$ and $D_B = 757nm, \delta = 0.44$ polarized along x; (c-d) $D_B = 757nm, \delta = 0.28$ and $D_B = 757nm, \delta = 0.44$ polarized along y

While in the figure 4.10b and d, are the results for a structure with bottom spheres diameter of 750 nm and upper diameter of 330 nm (with $\delta = 0.44$), respectively under polarization x and y. For the structure with $\delta = 0.44$, the reflectivity for the y polarization is slightly lower, for wavelengths ranging from 750 to 900 nm, with respect to the polarization along x. In terms of volume integral, values in the wavelength range from 750 to 900 nm are lower for the polarization along y respect polarization along x. The reflectivity spectra of the long polarization x and y for the structure with delta equal to $\delta = 0.28$, have no obvious differences. To better understand, the maps with the electromagnetic field distribution are shown in the figure 4.11. The electromagnetic field maps are taken along the xy cut plane and, represented accordingly to the formula $\log(|E_{TOT}/E_0|)^4$. In the figure 4.11 a-b, are showed the maps for $D_B = 757nm, \delta = 0.28$ and $D_B = 757nm, \delta = 0.44$ with a polarization along x and, in figure 4.11c-d with a polarization along y. Field maps were considered for the two most relevant wavelengths (785 nm and 900 nm).

The intensity and the number of hot spots remain unchanged, while changing the position as the polarization changes. The intensity of the electromagnetic field along the two polarizations remains unchanged, except for slight decreases, with reference mainly to hot spots. Considering the polarized structures along y there is a slight decrease of the intensity compared to the other polarization due to the small decrease of the integral of volume at low wavelengths (approximately around 750 to 900 nm). Instead, the hot spot position changes, changing polarization. In the table 4.6, the differences between the polarizations in terms of AVI, already intuited through the figure 4.10, are better deduced.

Table 4.6. Numerical results obtained for polarization.

Sample		AVI [μm^3]	
D_B	δ	Polarization x	Polarization y
757	0.28	6.50	6.50
757	0.44	149.70	133.30

Considering the substrate with $\delta = 0.28$, the values of AVI are equal while for delta the values of AVI are slightly lower for long polarization y (as shown also in figure 4.10d). The differences present are quietly negligible. To briefly summarize a large set of simulation varying the diameters of the spheres was carried out. The structures with the best presentations are those with $\delta = 0.44$, 0.48 and 0.52, respectively for values of bottom spheres diameter equal to $D_B = 500$, 750 and 1000 nm. Changing polarization from x to y, does not affect the response of the substrates. Increasing the diameter of the bottom spheres, increases the volume integral compared to CPA. Instead, CPA performance decreases as the diameter of spheres increases. By keeping the diameter of the bottom spheres constant and increasing the size of the upper spheres, the performance grow to a maximum to decrease progressively.

To summarize, hierarchical substrates with a double layer of spheres of different diameters of polystyrene has been simulated. Keeping the diameter of the bottom spheres fixed for values equal to 500, 750 and 1000 nm, the diameter of the upper spheres has been changed, respectively for δ values from 0.24 to 0.56.

The average volume integral on the 10nm conformal layer (on the gold surface) was used as figure of merit to evaluate the substrates performance. The numerical analysis showed that structures with *delta* values of 0.44, 0.48 and 0.52 (respectively for bottom sphere values of 500, 750 and 1000 nm) had the best performance compared to other structures, and above all respect the CPA.

To complete the analysis a study on the changing of the incident light polarization, going from x polarized to y polarized plane wave, was conducted. The chosen polarization does not affect the main results of the reported numerical analysis.

Chapter 5

Fabrication and morphological characterization of hierarchical SERS substrate

This chapter is described the methodology used to manufacture substrates and the results obtained after the morphological characterization. Two different self-assembly approaches were used to manufacture the substrates: co-deposition and sequential deposition. In the first paragraph, a detailed description on the manufacturing method and the geometrical characteristic of the fabricated samples. In the following section is described the set-up used to characterize the substrates manufactured. In the last paragraph is given a accurate description of the morphological outcomes obtained. In particular, the problems encountered, the main parameters of influence of the manufacturing process and the possible aspects to work on to improve the structures are deepened. The Fabrication and the morphological acquisition by Scanning elettron microscopy were implemented with the collaboration of the Institute of Chemical Sciences and Technologies "G. Natta" (SCITEC), Milan, Italy.

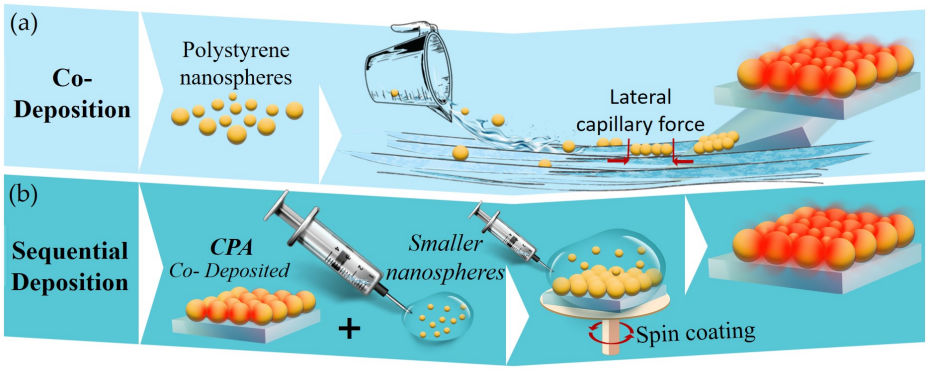

Figure 5.1. Schematic representation of the two approaches used for the nano-fabrication of HSNs: (a) co-deposition and (b) sequential deposition.

5.1 Fabrication process

To validate the results obtained by numerical analysis, several active sers substrates with hierarchical nanostructures were created using two distinct manufacturing methods. Based on the principle of self-assembly of nanospheres of two different diameters in an orderly way, the manufacturing process is distinguished in two primary approaches: co-deposition and sequential deposition, as illustrated in the figure 5.1 [166][167]. In the first approach, a solution containing nanospheres with different diameters self-assembles in a single step (figure 5.1a). While, the sequential deposition approach consists essentially of two phases (figure 5.1b): the former is the self-assembly of a single layer of bottom spheres (larger diameter) and then add over a second layer of upper spheres (smaller diameter). In other words, both approaches allow for a hierarchical structure with a lower layer of compact spheres, whose interstices are occupied by the upper spheres. Considering that each method has its own distinct constraints, the choice between the two methods is defined by the specific type of HSN substrate desired. Self-assembly methods significantly affect structures, due to the fact that the process used for hierarchical structures of binary colloidal crystals is considerably more complex (compared for example to a closed packed array structure). The co-deposition approach allows a large-scale HSN substrate to be produced in a single step.

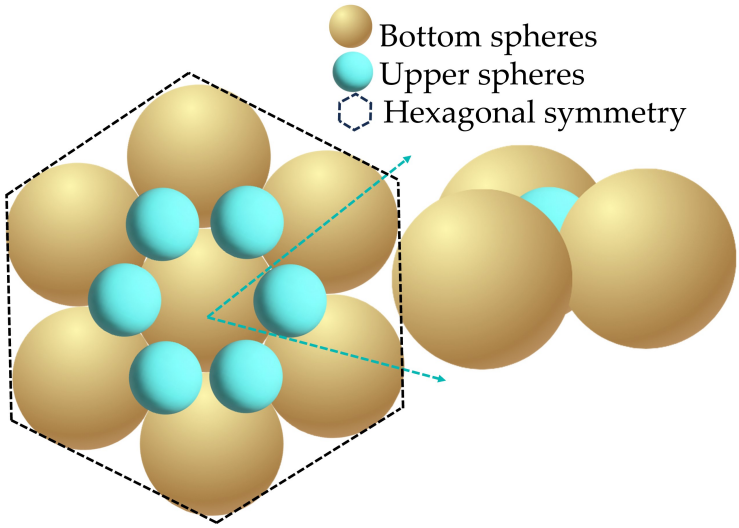

Figure 5.2. Schematic representation of the HSN structure.

The approach exploits the cohesive forces between the particles at the water air interface. In particular the bottom spheres serve as a guide for the upper spheres that are positioned between the interstitial sites formed by the bottom spheres, forming a layer (method typically used to manufacture the CPA). The process of co-deposition of polystyrene nanospheres to produce HSN active substrates on silica at the air/water interface has been successfully carried out. In this type of approach there are two fundamental parameters that greatly affect the formation of nanosphere structures in an orderly and uniform layout. The parameters are the dimensional ratio between the nanosphere diameters ($\delta = D_U/D_B$) and the number of nanospheres dissolved in the solution. These parameters must be chosen within a reasonable range. The number of nanospheres in solution is calculated as:

$$N_{U/B} = \frac{V_{U/B}}{\delta^3} \tag{5.1}$$

where $N_{U/B}$ is the ratio of the number of upper and bottom nanospheres, while $V_{U/B}$ is the ratio of the volumes of the two solutions (with the same

concentration). By considering the structure HSN shown in the figure 5.2 as target, $N_{U/B}$ should be placed equal to 2 (therefore the value of $V_{U/B}$ is defined according to the size of the nanospheres). The single deposition approach has been successfully used in the manufacture of HSN substrates having the following geometric characteristics: D_B = 757 nm, D_U = 196 nm, δ = 0,26 and $V_{U/B}$= 0.05 (theoretical = 0.035). A slightly higher $V_{U/B}$ value (theoretically obtained) was used, due to the fact that several manufacturing tentative with theoretical $V_{U/B}$ values led to structures with defects and missing spheres. These areas with missing nanospheres are due to the fact that the upper spheres tend to be trapped at defective sites, impoverishing the rest of the array. That is why, a slight excess is necessary and allows to manufacture expected and uniform hierarchical substrates. Polystyrene nanospheres (acquired at the microParticles GmbH, Berlin) were used for manufacture all the substrates, subsequently were covered with a 30 nm layer of gold.

In particular, two structure were fabricated using the co-deposition: the HSN1 (hierarchical structure with two layer of spheres) and the CPA (closed packed array with one layer of spheres). HSN1 and CPA were manufactured using the following parameters/products:

- CPA substrates [25]: fabricated by spreading on water a hydroalcoholic solution with 60 (μL) of spheres (5%w/v) aqueous suspension and 40 (μL) of EtOH. Collected on cleaned glass substrates, the colloidal crystal was pre-treated with oxygen plasma to increase their hydrophilicity. The substrate has a diameter of the spheres equal to 757 nm.

- HSN1 substrates: fabricated as above, using a hydroalcoholic solution with mixing 3 (μL) of upper spheres (5%w/v) and 60 (μL) of bottom spheres (5%w/v) aqueous suspensions (volume ratio 0.050), with 40(μL) of EtOH. The geometrical parameter of the structure are: D_B= 757 nm,D_U= 196 nm and δ= 0.26.

According to a study by Z. Dai et al.[168], to have ordered and uniform self-assembled systems, δ must not exceed the values of 0.3-0.4. In the figure 5.1b, are shown the steps on which the sequential deposition is based.

As the first step the co-deposition is used to form a single layer of bottom spheres, after a phase of thermal stabilization, we proceed by depositing a second layer of spheres with a lower diameter (upper spheres), over the first layer by spin-coating. This approach, respect co-deposition only, allows to overcome the imposed limits (relative to the δ values) and the geometric limitations are determined exclusively by the achievable geometry. By keeping the diameter of the bottom spheres D_B fixed, it was possible to make different substrates with upper diameter $D_U = 350, 425$ nm (respectively denominated HSN2 and HSN3). To prepare HSN2 and HSN3, a single layer of spheres (with 757 nm diameter) were first prepared using the co-deposition method (illustrated in figure 5.1a). Subsequently, the substrates were annealed at $60°C$ for 30 min to stabilize the structure. The upper sphere solution were spin-coated at 2500 rpm on top of these substrates (i.e the second step of the fabrication process, see figure 5.1b). In detail:

- HSN2: was used a hydroalcoholic solution of 350 nm spheres with a concentration of 1.25 $\%w/v$, composed by 25 μL of U solution 5$\%w/v$, 25 (μL) of H2O and 50 μL of EtOH.
- HSN3: was employed a hydroalcoholic solution of 425 nm spheres (concentrated at 2.5 $\%w/v$), obtained by 50 μL of U solution (5$\%w/v$), and 50 μL of EtOH.

Using those parameters, the substrates were successfully fabricated. All the substrate were coated with 30 nm of gold and ready to be tested/ characterized.

5.1.1 Experimental set-up for morphological charterization

HSN samples were fabricated directly on a silica layer and were morphologically characterized using an atomic force microscope (AFM) (JPK NanoWizard 4 XP). Morphological characterizations were performed when HSN samples were in a dry state. First the HSN samples were fixed on a flat support placed in the closed chamber of the AFM. The AFM measurements were carried out using the contactless mode in order to avoid causing damage or unwanted movements of the upper nanospheres (more exposed

for high delta values) placed on the bottom spheres. Once the images were taken, they were processed using the JPK Data Processing software. In addition to AFM imaging, further measurements were made using scanning electron microscopy (SEM). SEM analysis was performed using Phenom Pro Desktop microscope (Thermo Fisher Scientific Inc., Eindhoven, Netherlands). The SEM microscope has an acceleration voltage of 15.0 kV. The SEM acquisitions were made using simultaneously back-scattered and secondary electron detectors, in mixed mode.

5.2 Experimental results

In the previous paragraph are accurately described the two fabrication methods used to fabricate CPA and HSNs structures. The geometrical parameters of the fabricated samples are summarized in table 5.1. For the substrate fabricated using the co-depositing, the δ value was chosen equal to 0.26. The choice of δ was made considering that if the upper spheres are very huge compared to the bottom spheres, they interfere with the self-assembly mechanism and compromise the stability of the colloidal substrate. At the same time, the upper spheres must be large enough to position themselves and cover the interstices (between the bottom spheres) otherwise the hierarchical structure does not form. According to a study made by Z. Dai et al.[168], to have ordered and uniform self-assembled systems, δ must not exceed the values of 0.3-0.4. In fact, we have not been able to obtain hierarchically organized or reproducible substrates for greater δ values. The SEM images of the fabricated crystals (following the co-deposition approach) are shown in figure 5.3 a,b an c, referring to the

Table 5.1. Geometrical parameters of the fabricated substrates HSNs and CPA.

Name	D_B [nm]	D_U [nm]	δ	Fabrication approach
CPA	757	none	-	co-deposition
HSN1	757	196	0.26	co-deposition
HSN2	757	350	0.46	sequential deposition
HSN3	757	425	0.56	sequential deposition

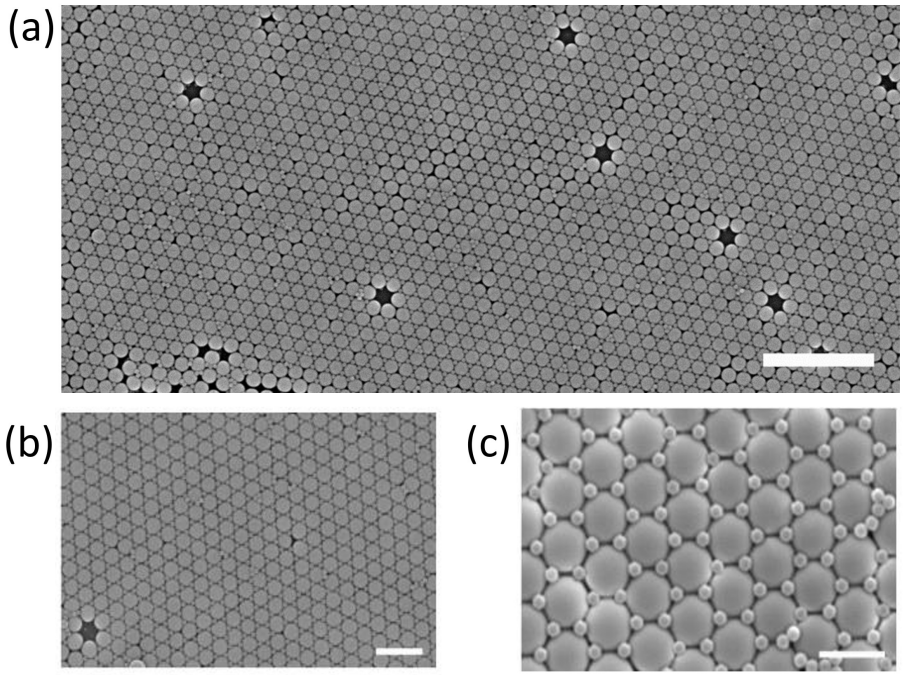

Figure 5.3. SEM of the fabricated hierarchical structure HSN1, viewed at two different magnifications. Scale bars are (a) 5 μm, (b) 2 μm and 1 μm.

HSN1 (the geometrical parameters are listed in table 5.1). Showed with different magnifications, the SEM images show how the upper spheres are perfectly placed between the interstices of the bottom spheres, creating a consistent pattern with the desired design substrate, with few excess, some agglomeration and few missing spheres. To make a comparison, in the same way, the CPA (single layer of only bottom nanospheres with a diameter equal to 757 nm). The CPA fabricated is shown in the figure 5.4. The spheres are closely arranged without gaps and missing spheres or structural defects. The numerical analysis outcomes (described in Chapter 4) showed that the best performing nanosphere structures are for samples with δ values above 0.4 (exactly 0.44, 0.48 and 0.52, respectively for bottom sphere values of 500, 750 and 1000 nm). With the co-deposition technique it is not possible to manufacture substrates with δ greater than 0.3.

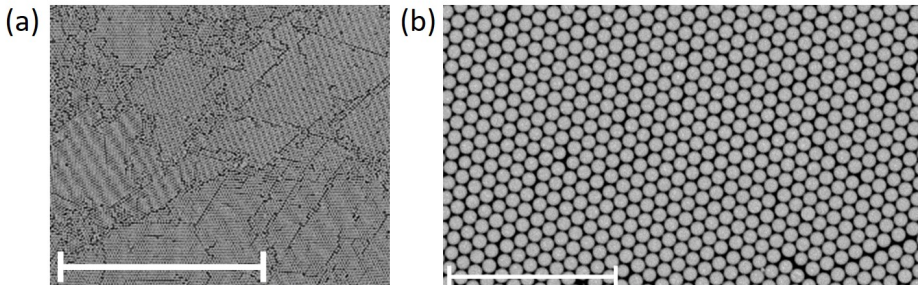

Figure 5.4. SEM of the fabricated structures CPA, with scale bars equal to (a) 50 $\mu m$and (b) 20 μm.

In order to manufacture an HSN structure with $\delta \geq 0.3$, the manufacturing technique based on sequential deposition was used. The sequential deposition consists in forming a first layer with co-deposition (of bottom spheres) and through spin coating is deposited a second layer of nanospheres with smaller diameters (upper spheres). Despite this technique increases fabrication complexity, adding a step to the process, allows to overcome the limitations of co-deposition technique and to realize uniform and ordered substrates. In particular, by properly regulating the deposition conditions, the hierarchical substrates were fabricated successfully through sequential deposition, with bottom spheres diameter fixed to 757 nm and upper spheres diameter equal to 350 and 425 nm (respectively: HSN2 with $\delta = 0.46$ and HSN3 with $\delta = 0.56$), listed in table 5.1.
In figure 5.5, the SEM images obtained of the HSN substrates manufactured called HSN2 is shown, with different magnifications. By increasing the size of the upper spheres, orderly structures were manufactured. Although some of the upper spheres are missing the substrates are overall homogeneous. In the two-step manufacturing process (sequential deposition), a crucial aspect is to minimize the possible defects that can form between the bottom layer of the spheres. If during the spin-coating phase, for example, the bottom nanospheres overlap, the upper spheres can accumulate around the overlap region, creating agglomerations. This is because the upper spheres tend to merge when they encounter an obstacle, so any existing defects (due to bottom spheres) would be amplified going to worsen the defects in the final structure.

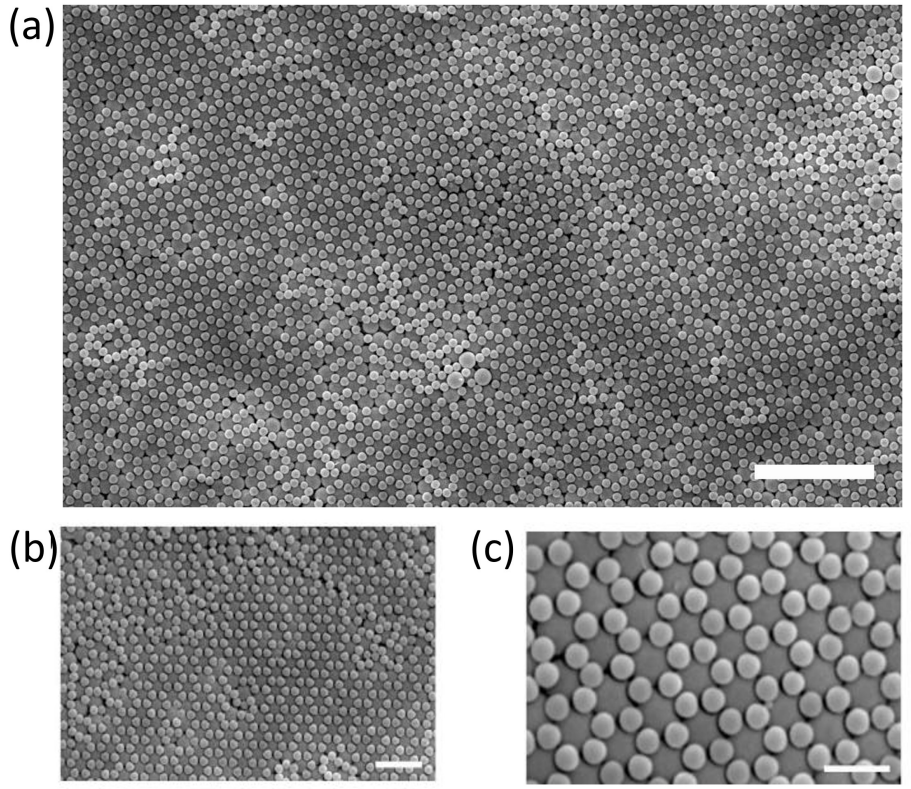

Figure 5.5. SEM of the fabricated hierarchical structure HSN2, viewed at three different magnifications with scale bars equal to (a) 5 μm, 2 μm and (c) 1 μm.

This is why having a orderly defect-free bottom spheres layer is a fundamental requirement for achieving high quality hierarchical structures. Using this approach, numerous attempts have been made to replicate HSN1. These approaches have been ineffective due to the huge significant difference between the diameters of the upper and lower nanospheres. The effects of the difference in diameter have been experimental to the assembly process. In fact, the substrates had areas with a high number of upper spheres and at the same time poor areas of nanospheres.

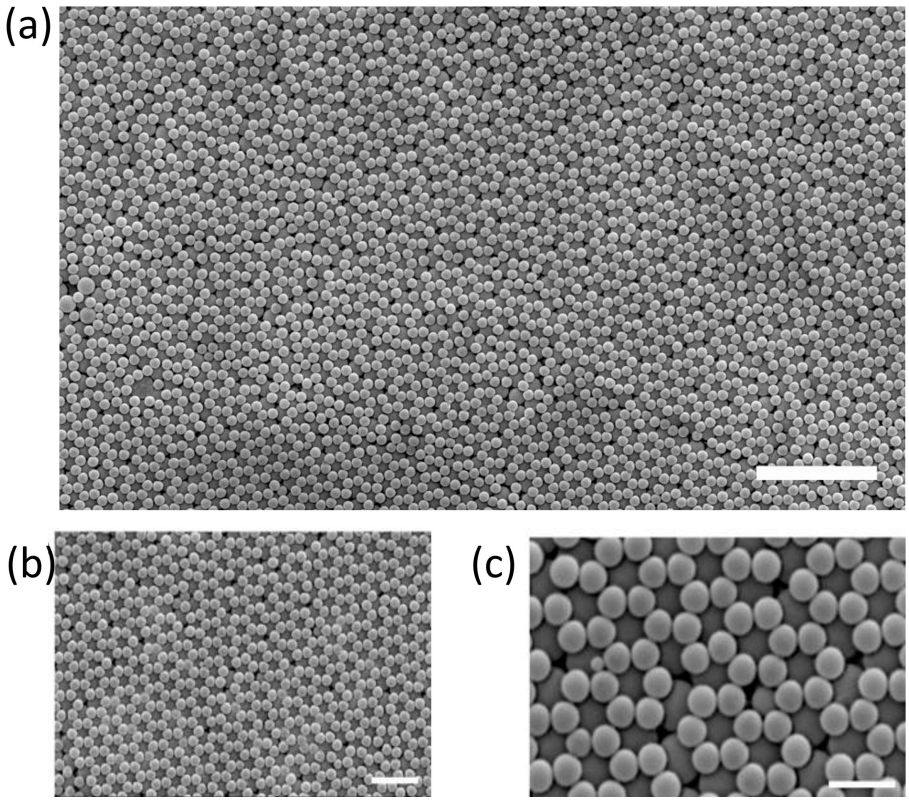

Figure 5.6. SEM of the fabricated hierarchical structure HSN3, viewed at three different magnifications with scale bars equal to (a) 5 μm, 2 μm and (c) 1 μm.

Accordingly, the SEM acquisitions made for the HSN3 substrate are shown in the figure 5.6. In figure 5.6 a, the SEM acquisition with scale bar 5 μm allows to view a larger area of the sample. In figure 5.6 b and c are shown the zoom in SEM acquisition, to better catch the substrate details (with a scale bar 2 μm and (c) 1 μm, respectively). As a result, it is possible to notice that the sample is regular even though some upper spheres are missing. The structure is assembled as planned, without forming agglomerations between the spheres.

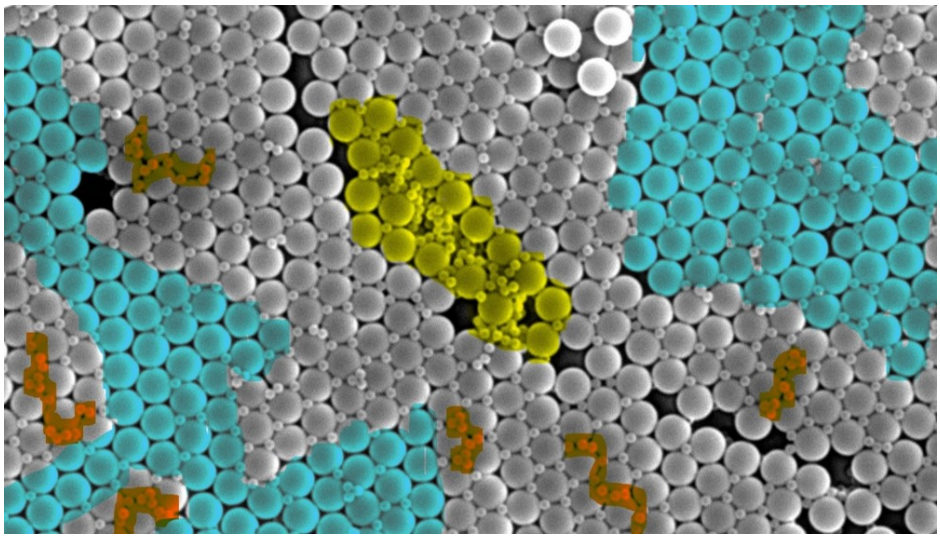

Figure 5.7. SEM acquisition of HSN1 obtained by sequential deposition. Different defects area are highlighted in different colors: yellow = excess of upper spheres caused by bottom layer defects, red = excess and cyan = poverty of upper spheres.

In figure 5.7, the defects due to the difference of diameters are illustrated through colored areas representing the abundance/deficiency of upper nanospheres. In particular, the blue areas are poor areas of upper nanospheres, the red areas are abundant areas and the yellow areas are agglomerated nanospheres due to defects of the bottom spheres. These negative effects have caused uneven regions containing varying concentrations of upper spheres, deviating from the desired hierarchical geometry. The morphological analysis carried out through AFM acquisitions, provided additional information, revealing significant differences on the samples. Considering the bottom spheres level as a reference point, the AFM height analysis shows that the upper spheres protrude from the bottom, with reference to the HSN2 and HSN3 samples (respectively, figures 5.8 c and f). Analyzing the section along the line covering six upper spheres and three close bottom spheres (blue line in figures), it emerged that the projection measures approximately 150 nm and 200 nm for HSN2 (figure 5.8 b) and HSN3 (figure 5.8 e), respectively.

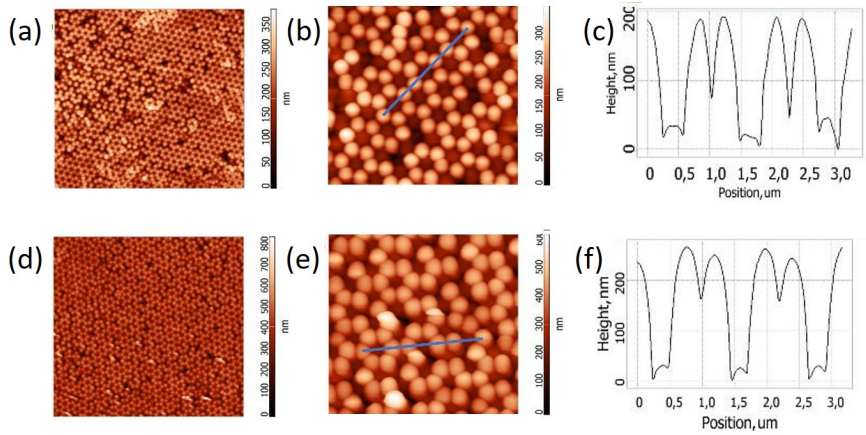

Figure 5.8. AFM analysis of the fabricated binary structures of different frame. Frame of 20 μm for (a) HSN2 and (d) HSN3; frame of 5 μm for (b) HSN2 and (e) HSN3; (c) and (f) the section analysis along the blue line of the corresponding to frame (b) and (e).

This measurement is also proven by the observation of the inclined HSN2 structure (relative to the observation plane), shown in figures 5.9. In contrast, in the HSN1 structure, upper nanospheres are hidden under the top plane of bottom spheres.

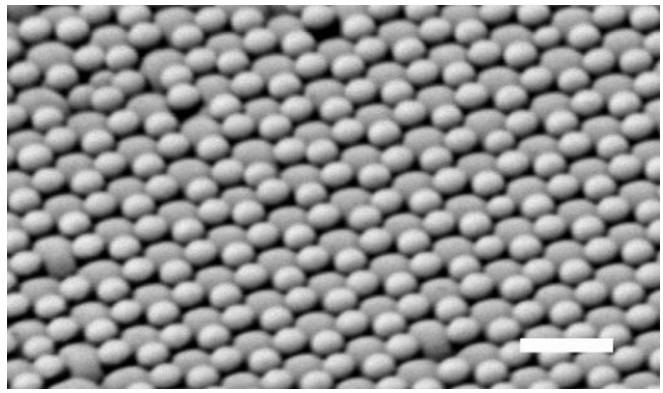

Figure 5.9. Tilted SEM image of HSN2, with a scale bar of 1 μm.

In figure 5.10 is shown the AFM acquisition considering a magnification of 20 μm, to appreciate the pattern of the substrate. Thanks to height analysis AFM presents in the figure 5.10b, the position of the upper spheres is calculated along the blue line. In figure 5.10 c, the height analysis reveals that the position of the upper spheres are approximately about 70 nm under the coordinate "z" of the bottom spheres.

To briefly summarized, morphological analysis outcomes reveals the the regularity of the obtained patterns. Definitively, to provide regular and quite ordered HSNs substrate both approaches have the ability to perform suitable substrate. Overall, the substrate of the target HSNs is the factor that determines the choice between the two methods. For HSNs with small values of δ (i.e., a large size of the difference between Upper and Bottom spheres), the co-deposition approach is particularly suitable. Meanwhile sequential deposition is the best option to achieve regular HSNs with larger δ values and it has less dimensional limitations.

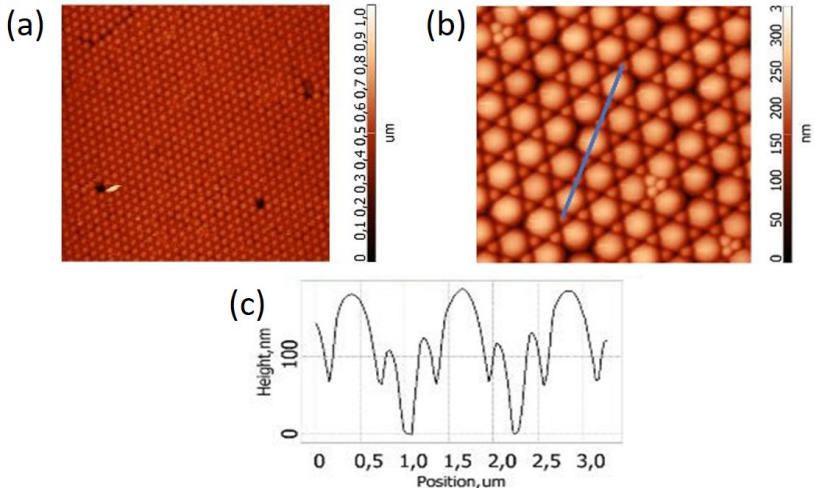

Figure 5.10. AFM analysis of the fabricated binary structure HSN1 of different frame. Frame of 20 μm for (a); frame of 5 μm for (b) and (c) the section analysis along the blue line of the corresponding to frame (b).

Chapter 6

Characterization and performance assessment of substrates

In this chapter, the characterization and performance assessment of SERS active substrates is implemented. The first paragraph deals with the methodology adopted for the sers characterization. To evaluate the performance and to establish which of the fabricated substrates are suitable as sers active probe, the the enhancement factor calculation is provided. detailed description, the actual wording of the EF and the main features of the Raman report used are reported. In particular, the Biphenyl-4-thiol (BPT) was employed as Raman reporter. For each substrate are considered: two intensity map to evaluate the hot spot distribution and the reproducibility and the SERS average spectra in the fingerprint region, whose peak value has been used to calculate the EF. The analysis was conducted considering the two main peak of the BPT, corresponding to the Raman shift 1080 cm^{-1} and 1585 cm^{-1}. Following the results obtained from the SERS characterization will be illustrated, for the manufactured substrates.

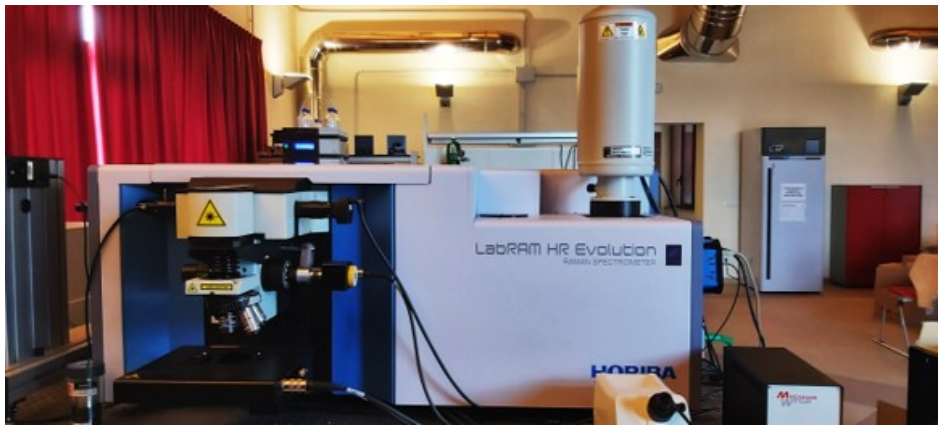

Figure 6.1. Labram HR Evolution (Horiba) microscope

6.1 Characterization methodology

The samples were characterized by SERS measurements, using Biphenyl-4-thiol (BPT) as Raman reporter. BPT is a substance that distributed itself uniformly on the substrate, avoiding agglomerations and allowing a more accurate estimation of the SERS signal. To measure the Raman spectrum, a small amount of BPT was used in the form of a 97% concentrated powder (produced by Sigma-Aldrich, St. Louis, MO, USA). Instead, for the acquisition of SERS, a liquid solution from BPT was used. To deposit a self-assembled uniform monolayer of BPT on the outer layer of the gold layer (covalently bonded to gold), the substrates were first immersed in the BPT solution (1 mm by 24 h), then washed in pure ethanol and finally allowed to air dry. Washing is a necessary step to eliminate any excess molecules that are not bonded to the surface. As a result of the functionalization of the substrates, the SERS and Raman signals were acquired via Labram HR Evolution (Horiba) microscope (figure 6.1). With an excitation wavelength of 785 nm, the laser source was focused through a 100x objective in the air onto the BPT substrate/dust, covering a circular area on the surface of the sample about $2.12\mu m$ in diameter. All spectra were captured by setting a grid on 300 /mm lines, for a single accumulation lasting one second and with a sample laser power of 410 μW.

The acquired XY maps have an area of $5 \times 5\mu m^2$ with a pitch of 0.5 μm for a total number of acquired points for single maps equal to 400. Intensity SERS maps were evaluated for three peaks related to Raman shift of the BPT molecule response at 1080, 1280 and 1585 cm^{-1}.

6.1.1 Enhancement Factor calculation

The performance of SERS substrates is well described by the definition of the enhancement factor (EF), a figure of merit able to compare different SERS substrate efficiently. In details, the EF quantify the ability of the SERS surface to enhance the electromagnetic field nearby the target analyte. The EF is defined as the product between the contribution of SERS signal per molecule (the intensity of the Raman signal coming from the active SERS surface I_{SERS}, normalized with the effective number of molecule contributing to the intensity N_{SERS}) to the Raman signal per molecule (the intensity of the Raman signal per molecule arise from the non-SERS active surface I_{Raman}/N_{Raman}). The equation 6.1 clarify the definition of the EF, calculated for the SERS substrate. Consequently:

$$EF = \frac{I_{SERS}}{N_{Raman}} \times \frac{N_{SERS}}{I_{Raman}} \tag{6.1}$$

In the equation 6.1 the term I_{SERS} represents the intensity of the SERS peak measured at 1585 cm^{-1} (of the substrate coated with BPT); I_{Raman} is the intensity of the Raman spectrum of the BPT powder (without the presence of the SERS substrate); while N_{SERS} and N_{Raman} are respectively the number of the molecule contributing to the SERS and the Raman signal. Following the methodology adopted in the works of Smythe et al.[169] and Le Ru et al. [170], the The number of the molecule contributing to SERS effect N_{SERS} is estimated according to:

$$N_{SERS} = A_{light} \cdot F_{SERS} \cdot \mu_s \tag{6.2}$$

Where μ_s is the packing density of the BPT molecule adsorbed by the substrate, assumed to be equal $4 molecules/nm^2$ [124]. The illuminated area of the substrate A_{light} is equal to $\pi \cdot r_{laser}^2$ (r_{laser} is the radius of the laser spot depending on the working wavelength). The A_{light} results to be 3.56 μm^2, with a wavelength $\lambda = 785nm$.

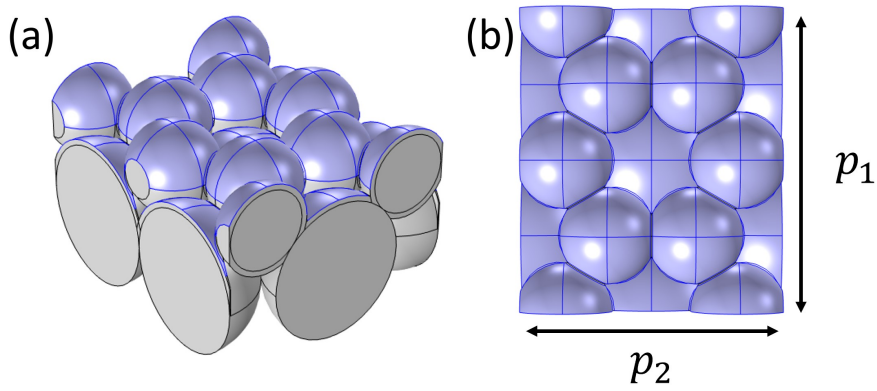

Figure 6.2. Schematic representation of the: (a) Exposed area and (b)Unit cell

F_{SERS} is the ratio of the exposed area of the substrate (A_{ex}) with the area of the unit cell of the structure (A_{uc}). In figure 6.2a is showed the exposed area in the unit cell, calculated through Comsol,in order to obtain an accurate estimation of the actual illuminated surface. In figure 6.2b, the unit cell is illustrated. The area of the unit cell is calculated as the product between p_1 (equal to $2 \cdot D_B$) and p_2 (equal to $\tan \pi/3 \cdot D_B$). The unit cell area has a value of 1.98 μm^2. Considering that upper spheres diameter do not influence the unit cell calculation, whose laterals dimensions depend on the bottom spheres diameter (757 nm), the unit cell area is equal for all the substrate. In table 6.1 are listed the respective exposed surface area and F_{SERS} for all the investigated substrate.

Table 6.1. Estimation of the exposed surface and the unit cell area for the CPA and HSNs substrate.

D_B	D_U	A_{ex}	F_{SERS}
757 nm	none	3.05 μm^2	1.538
757 nm	196 nm	2.84 μm^2	1.431
757 nm	350 nm	3.25 μm^2	1.637
757 nm	425 nm	3.11 μm^2	1.567

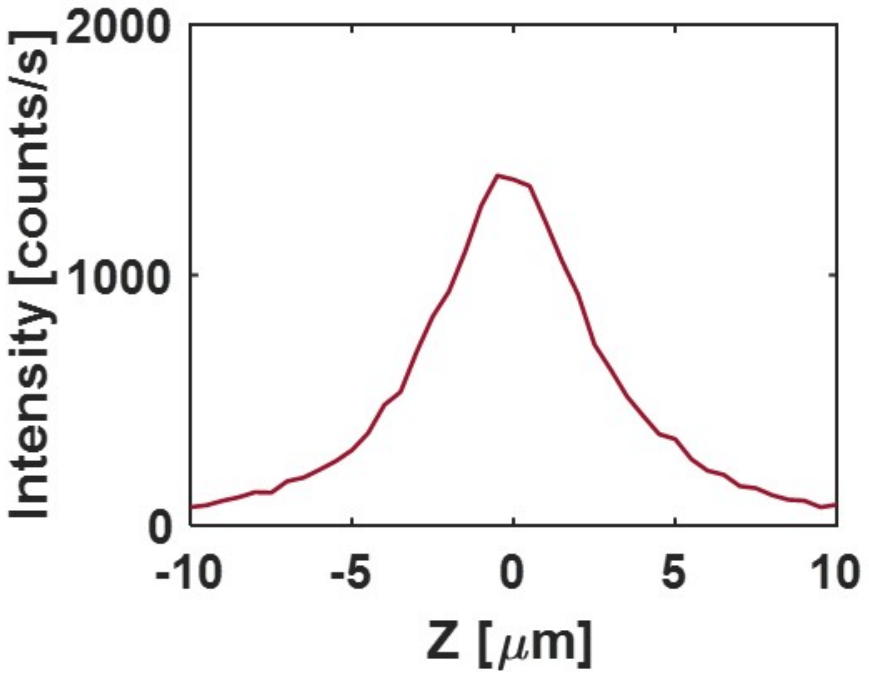

Figure 6.3. The 'z' profile of Raman signal of the silicon for 785 nm

As it is possible to observe in the table 6.1, the values of the exposed area for the individual substrates do not differ much from each other. The number of the molecule contributing to Raman effect N_{Raman} is defined as follows:

$$N_{Raman} = A_{obj} \cdot H_{obj} \cdot \rho_r \tag{6.3}$$

Where A_{obj} is the illuminated area by the source spot (equal to the upper term A_{light}). Since H_{obj} is the height of the BPT volume, the product $A_{obj} \cdot H_{obj}$ represents the BPT volume that contribute to the intensity of the Raman Signal. Simplifying A_{light} and A_{obj}, the remaining term H_{obj} is the one that affect the EF (for $\lambda = 785nm, H_{obj} = 0.919 \cdot 10^4 nm$). The parameter H_{obj} is determined by the measurement of the Z profile of the Raman signal of the silicon at 520.6 cm^{-1}.

The factor H_{obj} is calculated as follow:

$$H_{obj} = \frac{\int_{z_1}^{z_2} I_s(z)\, dz}{max(I_s)} \tag{6.4}$$

Where I_s is the Raman signal of the long z-profile of the silicon, with an excitation wavelength of 785 nm, in a window of -25,25 µm, represented in figure 6.3. The ρ_r is the BPT density and it is equal to $1.04 g/cm^3$ [169]. It is necessary to convert the unit of measurement from g/cm^3 to molecules/nm^3. Considering the Avogadro number equal to $6.022 \cdot 10^{23}$ 1/mol (N_a) and molecular weight of BPT equal to 182.27 g/mol (M), ρ_r is converted as follow:

$$\rho_r = \left[\frac{(1.04 g/cm^3) \cdot N_a}{M}\right] \cdot 10^{-21} = 3.44 molecules/nm^3 \tag{6.5}$$

To summarize and clarify the terms, the enhancement factor is equal to:

$$\begin{aligned} EF &= \frac{I_{SERS}}{I_{Raman}} \cdot \frac{A_{obj} \cdot H_{obj} \cdot \rho_r}{A_{light} \cdot F_{SERS} \cdot \mu_s} \\ &= \frac{I_{SERS}}{I_{Raman}} \cdot \frac{H_{obj} \cdot \rho_r}{F_{SERS} \cdot \mu_s} \end{aligned} \tag{6.6}$$

In the table 6.2, the terms with the respective values of the fixed parameters in the calculation of the enhancement factor are listed.
By using this parameters the EF is reduced to:

$$EF = \frac{I_{SERS}}{I_{Raman}} \cdot 0.39 \cdot 10^4 \tag{6.7}$$

The Raman signal is acquired from the BPT powder (97% concentrated). Meanwhile a BPT solution was used for the SERS signal. The intensity Raman I_{Raman} is taken respect the three main peaks (as for the SERS intensity of HSNs) at the Raman shift at 1080 cm^{-1}, 1290 cm^{-1} and 1585 cm^{-1}. For manufactured substrates, the respective SERS signals $I_{SERS}$are acquired (using the instrumentation and the method described in the previous paragraph).

In the next chapter 6, the results obtained for each sample will be shown. In particular, the outcomes obtained from the morphological analysis, the Raman and SERS intensity signal, the SERS field distribution and the enhancement factor calculated.

Table 6.2. Fixed parameters used to the EF calculation.

Parameter	Value
r_{laser}	2.13 μm
A_{light}=A_{obj}	3.56 μm^2
H_{obj}	$9.19 \cdot 10^3$ nm
μ_s	4 molecules/nm^2
ρ_r	3.44 molecules/nm^3
A_{uc}	$1.98 \cdot 10^6$ nm^2

6.2 Raman and SERS characterization results

For the manufactured and morphologically described samples, the SERS response has been studied in detail in order to assess the performance of each substrate and to check whether they actually behave as active SERS substrates. In particular, for HSNs and CPA structures, about 100 spectra of SERS signals (through raster scanning) were acquired, covering an area of 5x5 μm^2 with a pitch size corresponding to 0.5 μm. Details on the settings made for SERS signal measurements are broadly described in the previous paragraph. For all samples, the respective SERS response was investigated by depositing a homogeneous Biphenyl-4-thiol monolayer (BPT) on the outer surface of the substrate. BPT is a small molecule typically used as a standard molecular probe in the SERS/Raman environment, with the peculiarity of being distributed itself uniformly on the substrate, avoiding agglomerations and allowing a more accurate estimation of the SERS signal. A small amount of BPT was used in the form of a 97% concentrated powder for the Raman signal estimation.

The packing density of the BPT molecule adsorbed by the substrate is typically approximate to 4 molecules over $1nm^2$ [124]. When a BPT molecule is adsorbed from the gold surface of the substrate, it tends to change molecular polarization. This change results in well-known differences between the SERS spectrum and the signal spontaneously generated by the molecule. However, this known property is useful for estimating the molecular density and deposition condition of the monolayer [124]. The Raman signal is acquired under the same conditions of the SERS signal. The BPT has three peaks more intense corresponding respectively to the Raman shift 1080 cm^{-1},1290 cm^{-1} and 1585 cm^{-1}, characteristics of the molecule. The peak value are listed in table 6.3. In the figure 6.4 the Raman spectrum of BPT powder is shown. The three characteristic reference peak are highlighted by red boxes in the figure 6.4. The three characteristic peaks mentioned above are taken as a reference in the calculation of the signal sers. In particular at 1080 cm^{-1} and 1585 cm^{-1} (the peaks with the highest intensity), the bands are attributed to the C-H rocking mode and the phenyl ring mode [171]. Instead of powder, a liquid solution from BPT was deposited on the substrates external surface to acquire the respective SERS signal of the substrates. For each substrates, two field maps were acquired and for each map the corresponding mean value and average intensity signal over the spectral range. In order not to burden the treatment is shown only one map of the SERS intensity of the field of each samples. For the estimation of SERS performance, the enhancement factor calculation is implemented, accordingly to the method described in chapter 5. The quantitative comparison of SERS responses of the different types of SERS substrates reveals similarities and systematic differences, clearly. Specifically, the analysis is performed for the samples HSN1, HSN2 and HSN3 compered to CPA.

Table 6.3. The BPT Raman intensity corresponding respectively to the Raman shift 1080 cm^{-1},1290 cm^{-1} and 1585 cm^{-1}

Raman Shift	Peak Intensity
1080 $[cm^{-1}]$	41 [counts/s]
1290 $[cm^{-1}]$	85 [counts/s]
1585 $[cm^{-1}]$	123 [counts/s]

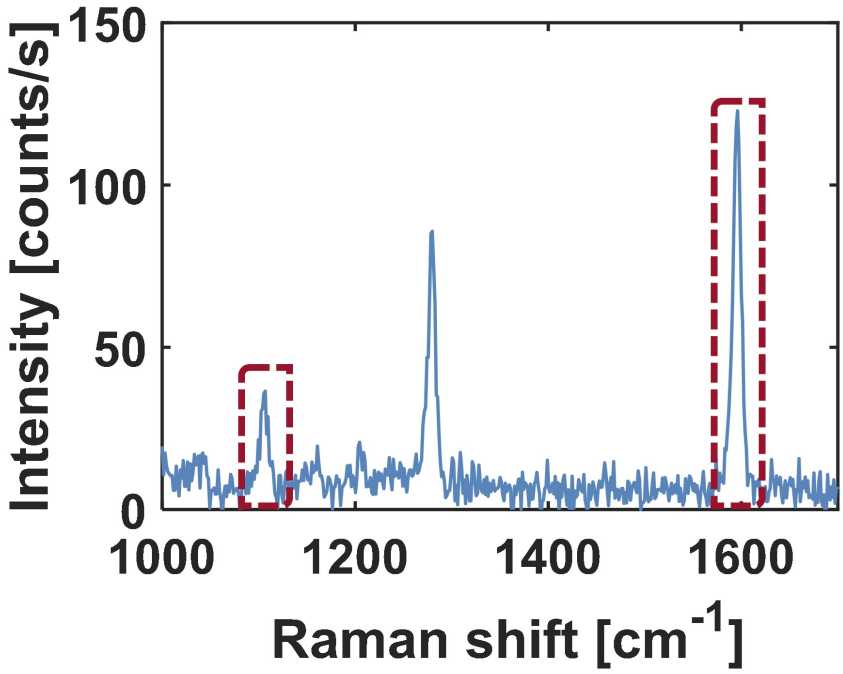

Figure 6.4. The intensity Raman signal of the BPT power.

The average SERS spectra (and associated standard deviation) for the samples CPA and HSN1 are reported in figure 6.5a and b. First, the HSN1 sample provides a very similar response to the CPA substrate. The geometric dimensions are equivalent for the bottom spheres 757 nm for both the samples, except for the presence of upper spheres in HSN1 (diameter 196 nm and δ= 0.26). In figure 6.5b compared to figure 6.5a, it is possible to note that the three reference bands have an equivalent response to less than a slight decrease in average intensity (i.e. HSN1 respect CPA). This phenomenon is fully in accordance with the numerical results obtained during the design phase of the substrate (in chapter 4). Partially evidenced by fabrication, upper nanospheres represent a small perturbation of the plasmonic resonance electromagnetic field. Being a slight perturbation of the system, the upper spheres do not affect the SERS response, providing a minor contribution.

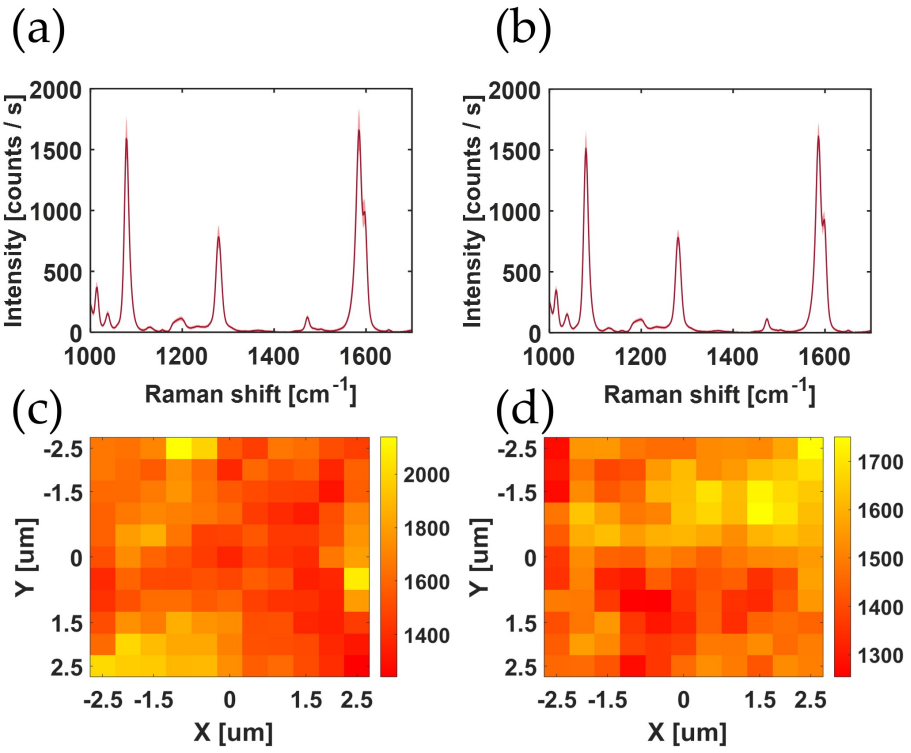

Figure 6.5. (a-b) Average SERS spectra and standard deviation for SERS active substrates CPA and HSN1; (c-d) SERS intensity map at 1080 cm^{-1} for CPA and HSN1 respectively, on a 5x5 μm^2 area.

Because of this phenomenon, the responses of HSN1 and CPA do not differ. In figure 6.5c and d are showed the intensity maps field distribution of the CPA and HSN1 respectively, related to the band peak at 1080 cm^{-1}. The SERS intensity maps confirm the similarity between the responses of the two substrates and except for a few points show an average intensity distributed similarly. Taking as reference the figure 5.3 a and b, in which the SEM image of HSN1 is shown, the distribution of the SERS average intensity highlights the in-homogeneity of the substrate HSN1, that already emerged from the morphological analysis.

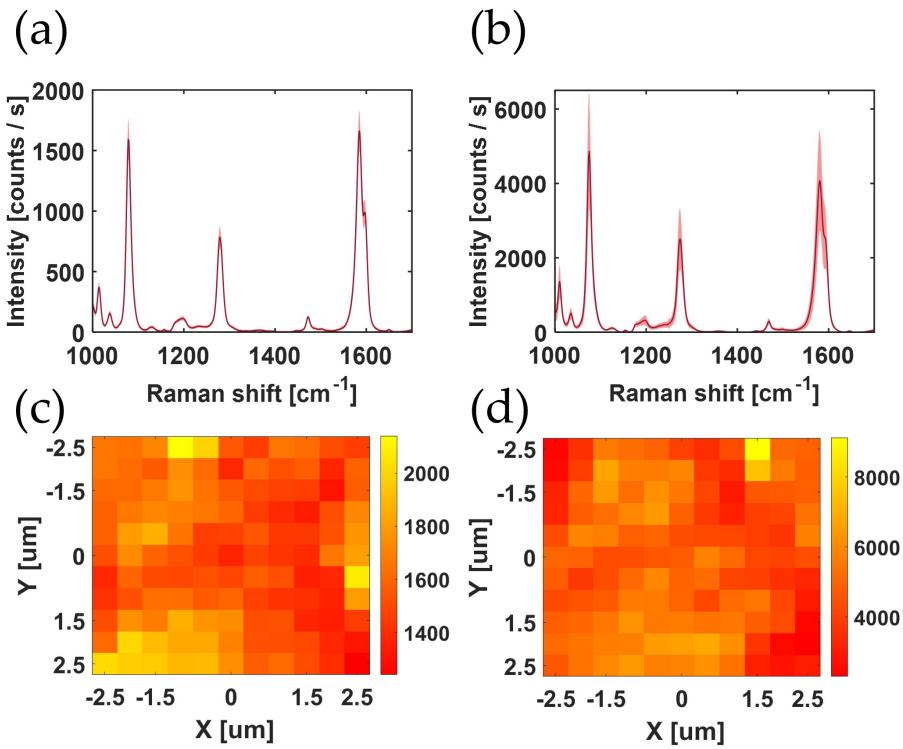

Figure 6.6. (a-b) Average SERS spectra and standard deviation for SERS active substrates CPA and HSN2; (c-d) SERS intensity map at 1080 cm^{-1} for CPA and HSN2 respectively, on a 5x5 μm^2 area.

In figure 6.6 b and d are reported the average SERS spectra and the SERS intensity maps for HSN2 compered to CPA (figure 6.6 a and c). Fabricated trough sequential deposition, the sample HSN2 has a bottom spheres diameter of 757 nm, upper spheres diameter of 350 nm and δ= 0.46. The substrate HSN2, which has a relatively high δ value, exhibits a considerable enhancement over the CPA sample. The average intensity SERS results to be for the HSN2 around three times over the the CPA, respect the Raman shift at 1080 cm^{-1}. Meanwhile, for the Raman peak at 1290 cm^{-1} and 1585 cm^{-1}, the HSN2 show an enhancement approximately around 2.5 times respect the CPA.

Similarly, HSN2 exceeds the average intensity values of the sers signal of HSN1 by a factor of 3.4, in accordance with the similarities obtained by comparing the CPA with HSN1. Obviously, this enhancement phenomenon is essentially due to the presence of upper nanospheres.In HSN2, upper nanospheres have a significantly higher diameter ratio than HSN1. Considering that the size of the upper nanospheres in HSN2 are considerably larger, their presence results in the formation of additional nanogaps and an increase in the number of hot spots. In full agreement with the numerical analysis carried out and assuming that the nanospheres are assembled in a uniform and orderly way (considering the precise formation of a 30 nm gold film), the upper nanospheres would lead to the formation of a gap s of 179 nm for HSN1 and 27 nm for HSN2. Whereas as nanogaps increase the SERS signal decreases [172], the decrease of nanogap s is one of the causes of the increase of the average intensity signal of HSN2, respect to HSN2. Considering the HSN2 substrate from a morphological point of view, the sample is not homogeneous,presenting defects in the structure. These defects are evident in the distribution of the intensity sers in figure 6.6 d. The map confirms the lack of homogeneity, presenting points extremely intense than the average. Nevertheless, the performance of HSN2 is better than the CPA and, as expected by the numerical analysis, the substrate HSN1. The samples HSN3 present a diameter of the upper spheres higher than the previous samples, with a value equal to 0.56 (with D_B=757 nm and D_U= 425 nm). In figures 6.7 b and d are shown the the average SERS spectra and the SERS intensity maps respectively for sample HSN3 at 1080 cm^{-1}, compered as previously to CPA (figures 6.7 a and c). The HSN3 is quite more than 2 times respect to CPA, at 1080 cm^{-1} (shown in the figures 6.7 a-b). Looking at the other peak, at 1585 cm^{-1} HSN3 is less than 2 times over the CPA . In figure 5.5 c-d is shown the SEM acquisition of the substrate HSN3. In this case, the sizes of the upper spheres are large enough to be in contact with each other, forming no gap. The structure is in general fairly homogeneous, despite some upper spheres failed to fit perfectly leaving empty areas. The numerical analysis showed that the structures had increasing performance up to a maximum reached with the structure having D_B= 750 nm and δ=0.48. Above these δ values performance began to decrease.

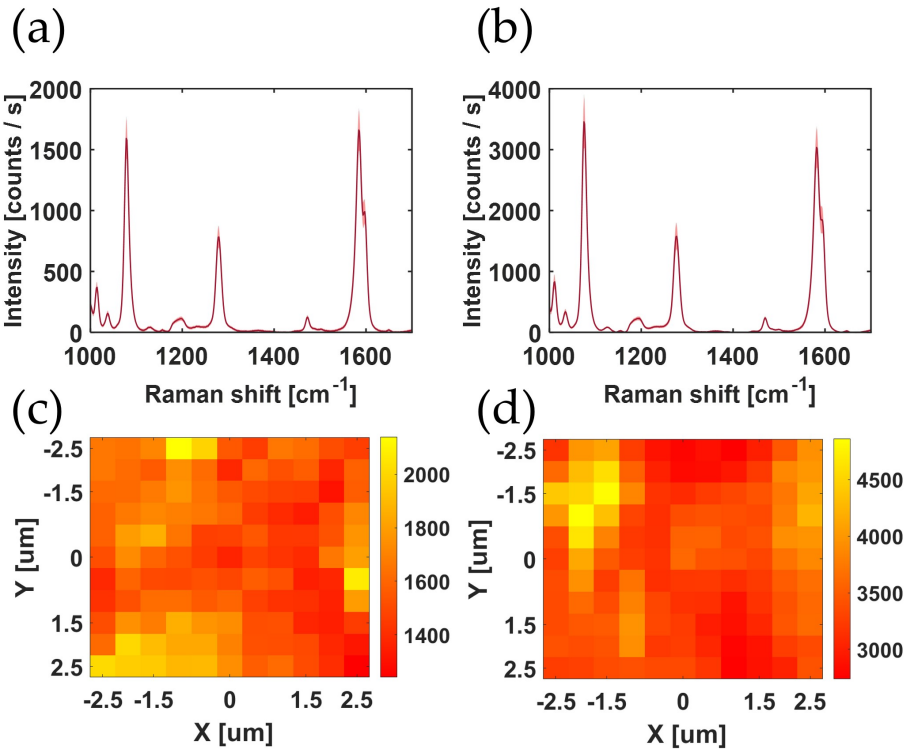

Figure 6.7. (a-b) Average SERS spectra and standard deviation for SERS active substrates CPA and HSN3; (c-d) SERS intensity map at 1080 cm^{-1} for CPA and HSN3 respectively, on a 5x5 μm^2 area.

The overall performance of HSN3 is higher than the CPA, although they remain lower than HSN2. Indeed, the HSN3 is lower by a factor 1.38 than the samples HSN2, at 1080 cm^{-1}. Keeping in mind these considerations, the outcomes emerged from the SERS performance analysis is consistent with the numerical analysis. Despite the structure there are no gaps between the upper spheres, we must also consider that they are large enough to obscure a small part of the hot spots available, which are created in correspondence with the bottom spheres. This feature of the geometry ends up influencing the actual exposed surface area available for BPT molecules, decreasing it.

The decrease of the exposed area and the consequent decrease of the hot spot accessible result in the decrease of the SERS intensity detected. Obviously this decrease concerns about the comparison with the structure HSN2, to CPA and HSN1, the sample is still winning. Indeed, HSN3 is greater than HSN1 by a significant factor 2.44 at 1080 cm^{-1} and a bit less than 2 at 1585 cm^{-1}. In figures 6.7 c-d, field maps for the CPA and HSN3 respectively are shown. The field map confirms what is already appreciated in the morphological analysis. In other words, the sample is generally homogeneous at the expense of some areas. The analysis of the average intensity SERS signals shows that all substrates (CPA and HSNs) are suitable for detecting the presence of BPT molecules, since (as can be seen in the figures 6.5 a-b, 6.6 b and 6.7 b), the main bands of BPT are clearly visible at 1080 cm^{-1}, 1290 cm^{-1} and at 1585 cm^{-1}.

In figure 6.8 are shown the intensity field maps related to the peak at at 1080 cm^{-1}, acquired in a different zone of samples respect the maps reported before. This second acquisition shows that the intensity maps of the field are not very homogeneous. Especially in the case of the HSN2 substrate, from a morphological point of view, the sample is not homogeneous and has different defects present in the structure. These defects are most evident in the intensity distribution of this second acquisition. On the other hand, the CPA and HSN1 exhibit a similar behavior of the field (figure 6.8 b and d)), as in the previous case (respectively in figure 6.5 c and d). The HSN2 sample shows highly localized field zones, as for HSN3 although with reduced intensity (respectively in figure 6.8 f and h). For the average intensity signals, the figures 6.8 a and c refer to samples CPA and HSN1. As you can see, the behavior is similar between the two samples, even if HSN1 has an average intensity slightly lower than the CPA. At the same time HSN1, in this second acquisition compared to the first, has a value almost higher. In the figures 6.8 e and g, for HSN2 and HSN3 respectively, the SERS average intensity signals reveal a slight drop in peak values to 1080 cm^{-1}. Also in this case, HSN3 is better than CPA and HSN, and at the same time lower than HSN2. These second acquisitions show how despite the highlighted differences, the performances remain analogous to the case with the first acquisitions.

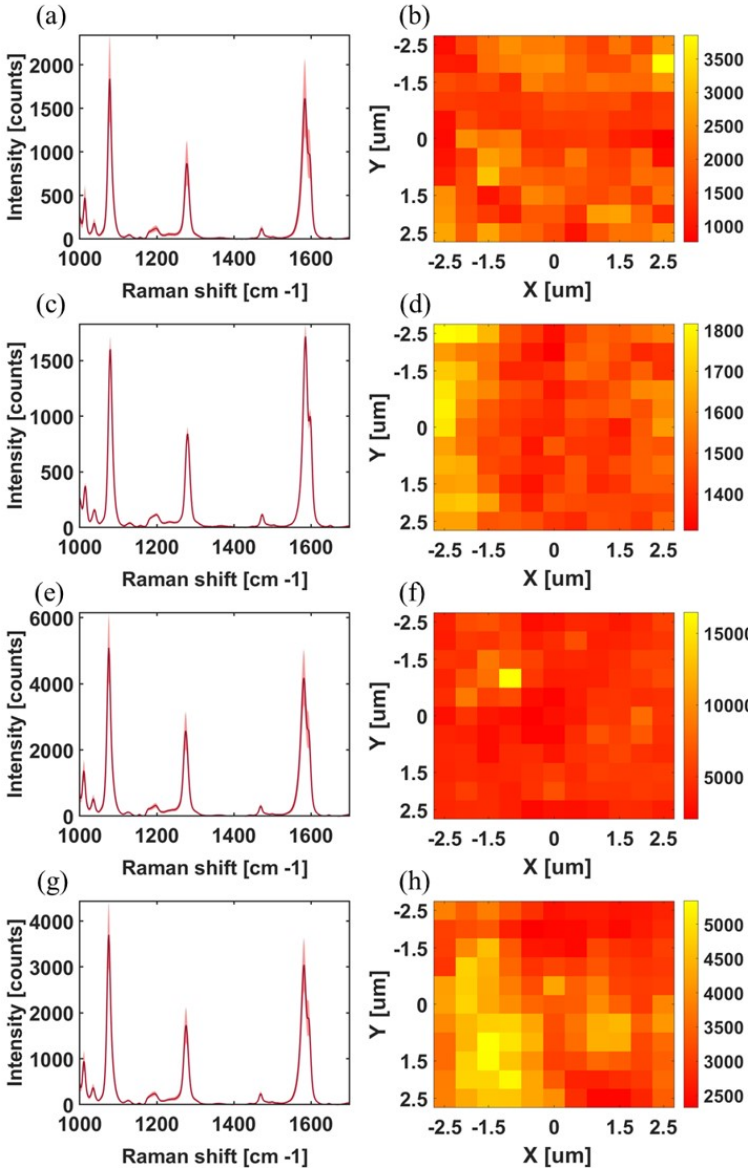

Figure 6.8. Average SERS spectra with standard deviation for SERS active substrates and SERS intensity map at 1080 cm^{-1} on a 5x5 μm^2 area second acquisition, respectively for: (a-b) CPA, (c-d) HSN1, (e-f) HSN2, (g-h) HSN3.

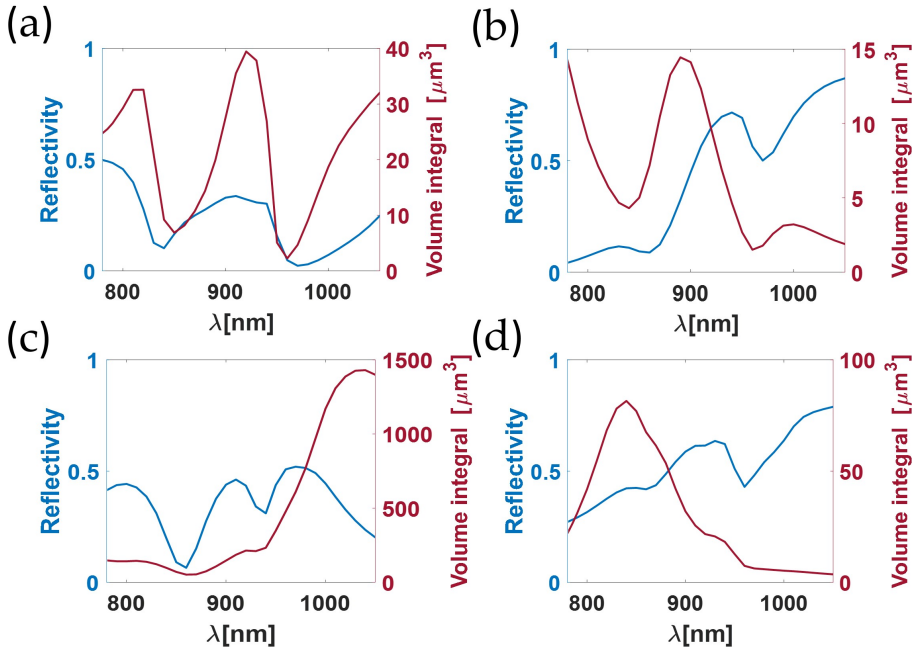

Figure 6.9. Numerical reflectivity and volume integral for SERS active substrates (a) CPA, (b) HSN1, (c) HSN2 and (d) HSN3, respectively.

We have numerically simulated the fabricated HSN structures and we report such numerical results, in term of reflectivity and volume integral in figure 6.9 and in terms of AVI in table 6.4. The reflectivity and integral volume are reported as a function of the wavelength of the samples under analysis. These graphs allow to understand and estimate the response of individual substrates across the wavelength range. By the observation of the spectral window from 785 to 910nm, it is possible to predict that the behavior of HSN1 (6.9 b) is analogous to CPA (6.9 a), with better performance in the range for λ = 850 nm to 950 nm. While in the figure 6.9 c, HSN2 presents a high volume integral compared to other samples throughout the analyzed range, with the best performance in the spectral window from 950 to 1050 nm. In figure 6.9 d, HSN3 has a high volume integral in the range of interest (785 at 910 nm), although it remains below the performance achieved by the HSN2 sample.

In table 6.4, the main characteristics associated with substrate performance are summarized, evaluated at the Raman shift corresponding to 1080 cm^{-1}. In particular, in the table 6.4 are listed the Peak Intensity (PI) with the associated standard deviation, Average Volume Integral(AVI), Enhancement Factor (EF) and the same terms expressed as ratio between the substrate HSNs and CPA relative to the firt acquisition. The PI and EF are calculated as described in the previous paragraph, by the experimental data set. Meanwhile the AVI has been calculated following numerical simulations as described in the chapter 4. Comparing the obtained PI values, the slight decrease in intensity between the HSN1 sample and the CPA substrate is even more evident, by emphasizing the similarity between the responses of the two structures. On the other hand, HSN2 and HSN3 samples show a noticeable increase in enhancement compared to CPA. In fact, the enhancement is exactly 3.23 and 2.35 times, respectively for HSN2 and HSN3, compared to the intensity provided by CPA, under the same conditions. Following a numerical analysis expressed in terms of AVI, it is possible to note how the relationships between HSNs and CPA (i.e AVI_{HSN}/AVI_{CPA}) represent a good approximation of the relationships obtained experimentally between the intensities of SERS signals. In fact, the AVI numerical model forecast an enhancement (compared to the CPA) of 5.4 for HSN2 and an exactly 2.4 for HSN3. The AVI for HSN1 is estimated as the half value obtained for CPA.

Table 6.4. SERS performance estimation for CPA and HSNs substrate in terms of : Peak Intensity, Average Volume Integral and Enhancement Factor, for a Raman shift at 1080 cm^{-1}.

@1080 cm^{-1}	PI $[\mu \pm \sigma]$	$\frac{PI_{HSN}}{PI_{CPA}}$	AVI $[\mu m^3]$	$\frac{AVI_{HSN}}{AVI_{CPA}}$	EF $[10^5]$	$\frac{EF_{HSN}}{EF_{CPA}}$
CPA	1578.11 ± 196.70	1.00	21.40	1.00	2.22	1.00
HSN1	1515.63 ± 106.20	0.96	9.60	0.45	2.29	1.03
HSN2	5094.35 ± 1117.40	3.23	116.10	5.40	6.74	3.03
HSN3	3701.24 ± 443.90	2.35	52.50	2.40	5.12	2.30

In performing a numerical simulation analysis, the computational domain is chosen in order to mimic, as much as possible, the fundamental underlying physical phenomena and the actual geometry, object of study. In the choice of the domain, some factors come play a relevant role, such as the computational requirements and the physical resources to simulate the device, which limit the possibility of simulating the physical reality faithfully. In this process some unavoidable approximations are made, such as the choice of mesh and the domain size. In fact, the program used to simulate HSNs and CPA structures uses a truncated domain replicated to infinity (i.e. the unit cell with the boundary conditions of Floquet). These choices are made in such a way as to have a trade-off between computational requirements and accuracy that does not affect the system response. Beyond these factors, the computational domain is idealized and presents inherent difficulties in capturing the minute characteristics of plasmonic nanostructures. Despite the difficulties, the numerical and experimental data are in agreement. The agreement between the data is considered good both from the point of view of the numerical model, capable of identifying the best configuration and from the experimental point of view, with the ability to provide a quantitative estimate of the expected performance.

The figures 6.5, 6.6 and 6.7, show the respective field maps for the samples analysed, from which the spatial distribution of the SERS response along the scanned area can be derived. The SERS intensity along the map varies around the reported average value, except for a few peaks at higher intensity. For example, HSN3 generally varies around 3700 counts/s, with small areas of higher intensity (with reference to figures 6.7 b and table 6.4). Both CPA and HSNs sample maps reveal a general lack of homogeneity in the SERS response. The in-homogeneity of the SERS response in the field maps can be quantified by the standard deviation given for each sample in the table. The standard deviation of the SERS intensity generally increases with the intensity itself. At the same time the coefficient of variation (ratio of standard deviation to mean) is higher for substrates with SERS improvement. In fact for HSN2, which represents the substrate with the best performance, the coefficient of variation is $\sigma/\mu[\%]$ (i.e. ratio of the standard deviation to the mean, obtained from experimental Peak Intensity values) equal to 21.9 %, meanwhile HSN3 has a value of 12 %.

Samples with reduced performance, CPA and HSN1, report a coefficient of variation values of 12.5 % and 7 %, respectively. Finally, always in the table 6.4 are the values of enhancement factor (EF) estimated for the substrates CPA and HSNs, relative to Raman shift at 1080 cm^{-1}, according to the methodology in the previous paragraph. In essence, the EF allows to estimate practically the amplification of the average SERS signals on the area covered by the incident laser beam. The CPA shows an EF value of 2.22 $\cdot 10^5$, very similarly the HSN1 show a value of 2.29 $\cdot 10^5$. Meanwhile the substrate with the best performance HSN2 presents an EF equal to 6.74 $\cdot 10^5$, followed by HSN3 with EF equal to 5.12 $\cdot 10^5$. All these values obtained can be considered valid, for practical use in SERS applications.

Based on the results of the morphological characterization, it is clear that the observed variations in SERS intensity cannot be solely attributed to structural defects, such as missing or additional nanospheres or disruptions in the structural symmetry of the hierarchical nanospheres structure, under investigation. This is primarily because the HSNs being studied exhibit a a similar degree of structural order. Instead, the fluctuations in SERS intensity are ascribed to the inhomogeneity, due to inherent variability in the diameters of the nanospheres and, consequently, the nanogaps between them. The data from the Polystyrene nanospheres data sheet indicates that the nanospheres diameters typically have a slight variation around a mean value with a standard deviation of approximately 10 nanometers. To prove the idea that this small diameter variability is responsible for the observed fluctuations in intensity, a numerical analysis was conducted. Specifically the effects of a ± 5 nm change in the diameter of the upper nanospheres in sample HSN2 was examined. A 5 nm reduction in diameter resulted in a 16 % decrease in AVI, while a 5 nm increase in diameter led to a 53 % increase of the same parameter. The details of this analysis are shown in figure 6.10, with the reflectivity and volume integral for SERS active substrates with HSN2 upper spheres diameter variations of ± 5 nm. To quantify the changes, the AVI was used together with the percentage variation (called "Δ (AVI) [%]"), shown in the table 6.5. Looking at the reflectivity graphs, a change in the spectrum is clearly evident in increasing the diameter of nanospheres.

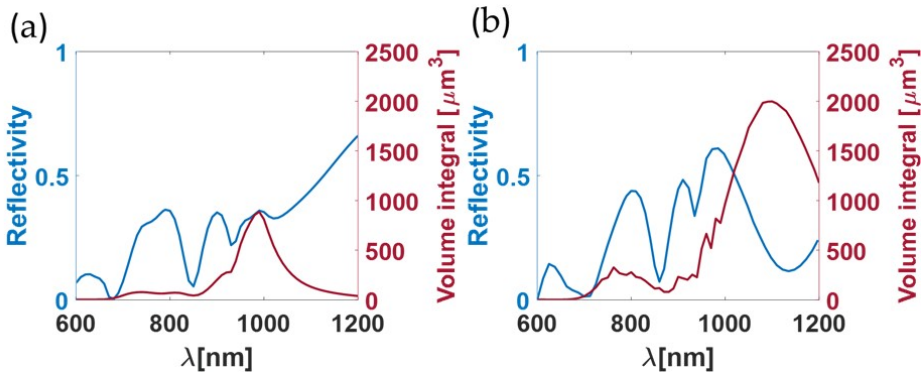

Figure 6.10. NNumerical reflectivity and volume integral on the 10nm conformal air overlay of the forth power of the normalized electric field for SERS active substrates (a) HSN2 - 5nm and (b) HSN2 + 5nm, respectively.

In the range of wavelengths below 900 nm, it is possible to observe how the peaks present in the structure HSN2 - 5 nm are more intense and marked in the structure HSN2 + 5 nm. In the HSN2 + 5 nm structure, above the 900 nm wavelength, a maximum and a minimum not present in HSN2 - 5 nm appears. These differences are all the more evident when analysing the volume integral. In fact increasing the diameter, it is interested to notice that the integral increases remarkably, increasing also the bandwidth. It is important to note that in the numerical model, the diameter variation uniformly affects all upper nanospheres, whereas in real experiments, random fluctuations in nanospheres diameters occur due to

Table 6.5. Numerical AVI comparison with % variation of HSN2 structure with upper spheres diameters ±5nm.

Samples	D_B [nm]	D_U [nm]	AVI [μm^3]	Δ (AVI) [%]
HSN2 – 5nm	757	345	44.9	-16.85
HSN2	757	350	54.0	-
HSN2 + 5nm	757	355	82.7	53.15

self-assembly fabrication tolerances and the inherent variability in the original nanospheres diameters. In particular, the small nanogaps that form within the HSN2 substrate contribute to a more intense SERS response. However, these small nanogaps are highly sensitive to variations in the diameters of nanospheres, resulting in more significant changes in the intensity of SERS hot spots. In essence, the higher the intensities of the hot brides, the more pronounced is the variation in intensity in response to a disturbance in the nanogaps size, related to manufacturing self-assembly tolerances. In table 6.6 are summed up the fundamental parameters (Peak Intensity, Average Volume Integral and Enhancement Factor) related to the second SERS acquisition at 1080 cm^{-1} for the analyzed samples. It is worth noting that the performance of HSNs and CPA samples is consistent with the observations made previously, despite the peak intensities (PI) in the case of HSN2 and HSN3 are lower than the first acquisitions (table 6.4). HSN2 changes from PI values of 5094.35 to 4862.11 counts/s with an increase in standard deviation of 504.3. This decrease manifests itself directly in the calculation of the enhancement factor, with a small decrement of a value corresponding to 0.31 (respect the first acquisition). With reference to sample HSN3, the decrease in terms of intensity of peak produces a decrease of the enhancement factor, between the first acquisition and the second, of approximately 0.39. In the opposite way, in the second acquisition there is an increase in the general values compared to the samples : CPA and HSN1. In fact the CPA takes an increment of PI of approximately 262 counts/s, while more moderately HSN1 introduces an increment of 154 counts/s.

Table 6.6. SERS performance estimation for CPA and HSNs substrate in terms of : Peak Intensity, Average Volume Integral and Enhancement Factor, for a Raman shift at 1080 cm^{-1} related to the second acquisition.

@1080 cm^{-1}	PI $[\mu \pm \sigma]$	$\frac{PI_{HSN}}{PI_{CPA}}$	AVI $[\mu m^3]$	$\frac{AVI_{HSN}}{AVI_{CPA}}$	EF $[10^5]$	$\frac{EF_{HSN}}{EF_{CPA}}$
CPA	1840.24 ± 341.08	1.00	21.40	1.00	2.59	1.00
HSN1	1669.58 ± 112.20	0.91	9.60	0.45	2.52	0.97
HSN2	4862.11 ± 1674.70	2.64	116.10	5.40	6.43	2.48
HSN3	3419.39 ± 775.00	1.86	52.50	2.40	4.73	1.82

Looking at the EF, the CPA goes from a value of 2.22 to 2.59, simultaneously the HSN1 switch from 2.29 to 2.52. HSN1 respect the first acquisition exhibits a negligible decrease in EF of about 0.06. In other words, although the CPA and HSN1 have differences in performance between one acquisition and the other, these are negligible, confirming the similarities between the two samples (HSN1 $\approx$ CPA). The coefficient of variation (σ/μ [%]) for CPA and HSN1 is 18 % and 7 % respectively, not so different from the first acquisition (12.5 % and 7 %). For the samples HSN2 and HSN3 the coefficient of variation is equal to 35 % and 23 %, respectively. An increase of 13.1 % (for HSN2) and 11 % (for CPA) is present compared to the case of the first acquisitions. The increase of the coefficient of variation for the two samples is due to the fact that simultaneously increases the standard deviation and decreases the peak intensity. Despite the differences highlighted, the second acquisitions made and analyzed repeated at the Raman shift at 1080 cm^{-1} are in accordance with the analysis and considerations expressed regarding the first acquisitions. This second acquisition is essentially aimed at verifying the repeatability and reliability of the measurements made. In order to have a complete analysis of substrate performance, the characteristics of the two fundamental peaks of the target molecule were analysed. The BPT has two fundamental (more intense) peaks for the Raman shift at 1080 cm^{-1} and 1585 cm^{-1}. The peak performance of 1080 cm^{-1} has been analysed for CPA and HSNs substrates. Similarly to the above, the analysis of peak 1585 cm^{-1} is reported below. In figure 6.11 are shown the average SERS spectra with standard deviation and the SERS intensity map for the CPA and HSNs structures. Consistently, the CPA and HSN1 samples both show a slight increase in peak intensity to 1585 cm^{-1} compared to the 1080 cm^{-1} Raman shift (shown in figure 6.11 a and c, respectively). This increment is approximately 100 counts/s for both samples. While for samples HSN2 and HSN3 there is a decrease in the intensity of approximately 900 and 700 counts/s, respectively (with the reference to figure 6.11 e and g). In figure 6.11 are shown the maps of SERS intensity, acquired for 1585cm^{-1}, in the same region in which the maps were acquired for 1080 cm^{-1} (figure 6.5, 6.6 and 6.7). Analysis of the maps confirms that the samples are not homogeneous, with strongly localized areas.

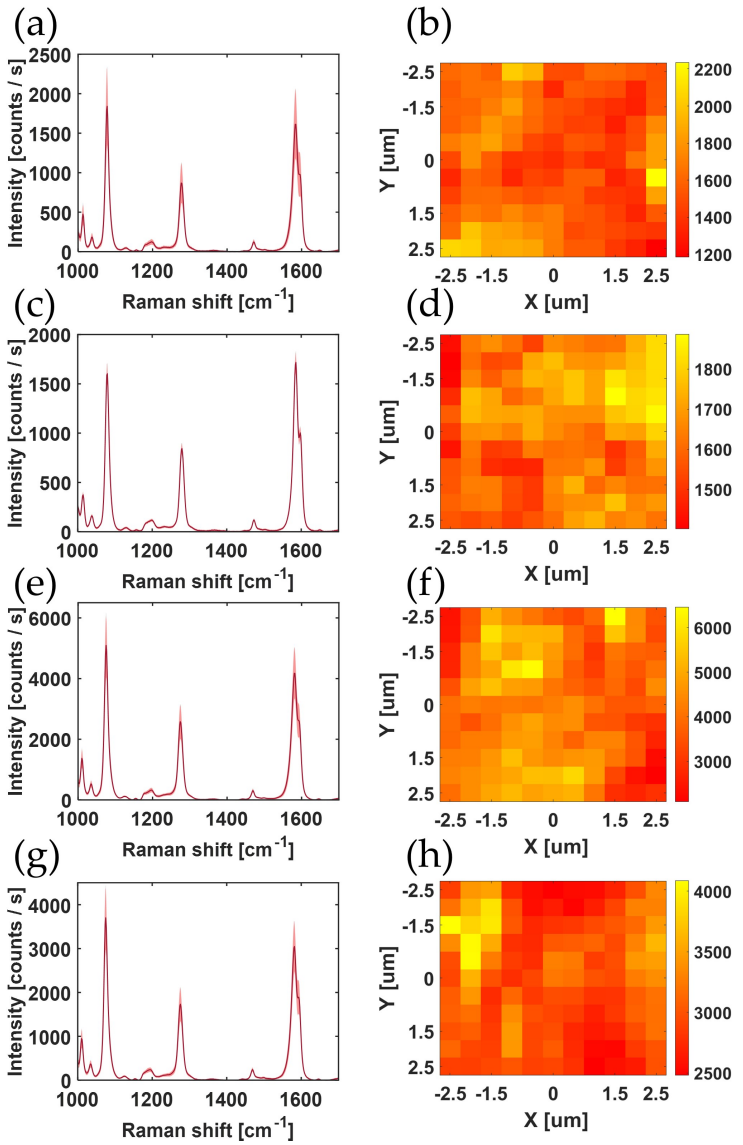

Figure 6.11. Average SERS spectra with standard deviation for SERS active substrates and SERS intensity map at 1585 cm^{-1} on a 5x5 μm^2 area, respectively for: (a-b) CPA, (c-d) HSN1, (e-f) HSN2, (g-h) HSN3.

While for samples HSN1 (in figure 6.11 d) and HSN2 (in figures 6.11 f) the inhomogeneous in terms of hot spot distribution is not very marked, for sample HSN3 (in figure 6.11 h) it is particularly noticeable. Especially, the substrate HSN2 exhibits the most intense map filed and average SERS spectra respect the other sample. In fact,after the SEM acquisitions, in the chapter 5 (where the morphological analysis of the samples is illustrated) was found that the HSN3 sample compared to HSN2 had some structural defects due to missing spheres (figure 5.5). Accordingly, the analysis of SERS intensity maps confirms the observations obtained by the SEM analysis and the analysis of maps at 1080 cm^{-1}. Looking at the field maps at both Raman shifts, there are no major differences in the location and distribution of hot spots in the analyzed region. In any case, there are differences in terms of peak values. At Raman shift 1585cm^{-1}, for HSN1 seem to increase slightly the areas with a greater intensity, while for the other samples the only variation of intensity is perceived.

In the table 6.7 are reported the principal parameters to estimate the SERS performance of the substrate, from the numerical and experimental point of view for the first acquisition at Raman shift 1585 cm^{-1}. Comparing the peak relative to Raman shift at 1585 cm^{-1} with peak at 1080 cm^{-1}, for CPA and HSN1, the analysis of SERS intensity showed that it peak value increased, accordingly, estimating the values accurately the table 6.7 shows how the standard deviation increases for CPA by 46 and decreases by 6 for HSN1. In the case of the other two substrates, the standard deviation is reduced by 253 for HSN2 and 101 for HSN3. The coefficient of variation (σ/μ is equal to 15 % for the CPA, 6 % for the HSN1, 21 % for the HSN2 and 12 % for the HSN3. Respect the results at the Raman shift 1080 cm^{-1}, the vales of the coefficient of variation are approximately the same for 1585 cm^{-1},demonstrating a data consistency. It is also interesting to note that the enhancement factor calculated at 1585 cm^{-1} for CPA and sample HSN1 has been reduced by about a factor of 3 compared to the values obtained considering the peak at 1080 cm^{-1}. This reduction is mainly due to the fact that the BPT's Raman signal exhibits a well-defined and more intense peak at 1585 cm^{-1} (the average Raman spectra of BPT is shown in figure 6.3).

Keeping in mind that higher is the Raman signal of the sample analysed, the lower is the resulting EF. As for the HSN2 and HSN3 samples, the EF is reduced dramatically due to the fact that in addition to increasing the Raman signal, also decreases the SERS signal acquired. Despite these marked variations HSN2 is the best performing sample, followed by HSN3. The same result was obtained following the analysis made for the Raman shift at 1080 cm^{-1}.

The second acquisition of average SERS spectra with standard deviation for the SERS active substrates and SERS intensity map at 1585 cm^{-1} are showed in figure 6.12. This second acquisition is spatially located on the samples in the same area in which the second acquisition at a Raman shift at 1080 cm^{-1} is made. Considering the second acquisition SERS average spectra, at 1585 cm^{-1} (figure 6.12 a) the samples CPA shows a reduced intensity peak around 200 counts/s, respect the Raman shift at 1080 cm^{-1} (figure 6.8 a). Meanwhile the samples HSN1 presents similar values for both peaks (figure 6.8 c and 6.12 c). On the same way of the substrate CPA, HSN2 and HSN3 has lower peaks for the Raman shift at 1585 cm^{-1} (figure 6.12 e and g) respect the peak at 1080 cm^{-1} (figure 6.8 e and g). Respect the first acquisition at 1585 cm^{-1} (figure 6.11), for the second acquisition, the SERS average spectra exhibit very close peak values, unless small variations (figure 6.12). In terms of field location distribution,"hot spot distribution", the second field map acquisition provides several useful information.

Table 6.7. SERS performance estimation for CPA and HSNs substrate in terms of : Peak Intensity, Average Volume Integral and Enhancement Factor, for a Raman shift at 1585 cm^{-1}, related to the first acquisition.

@1585 cm^{-1}	PI $[\mu \pm \sigma]$	$\frac{PI_{HSN}}{PI_{CPA}}$	AVI $[\mu m^3]$	$\frac{AVI_{HSN}}{AVI_{CPA}}$	EF $[10^5]$	$\frac{EF_{HSN}}{EF_{CPA}}$
CPA	1660.92 ± 243.12	1.00	21.40	1.00	0.69	1.00
HSN1	1691.47 ± 100.80	1.01	9.60	0.45	0.76	1.09
HSN2	4174.92 ± 864.80	2.51	116.10	5.40	1.64	2.36
HSN3	3037.10 ± 342.80	1.82	52.50	2.40	1.24	1.79

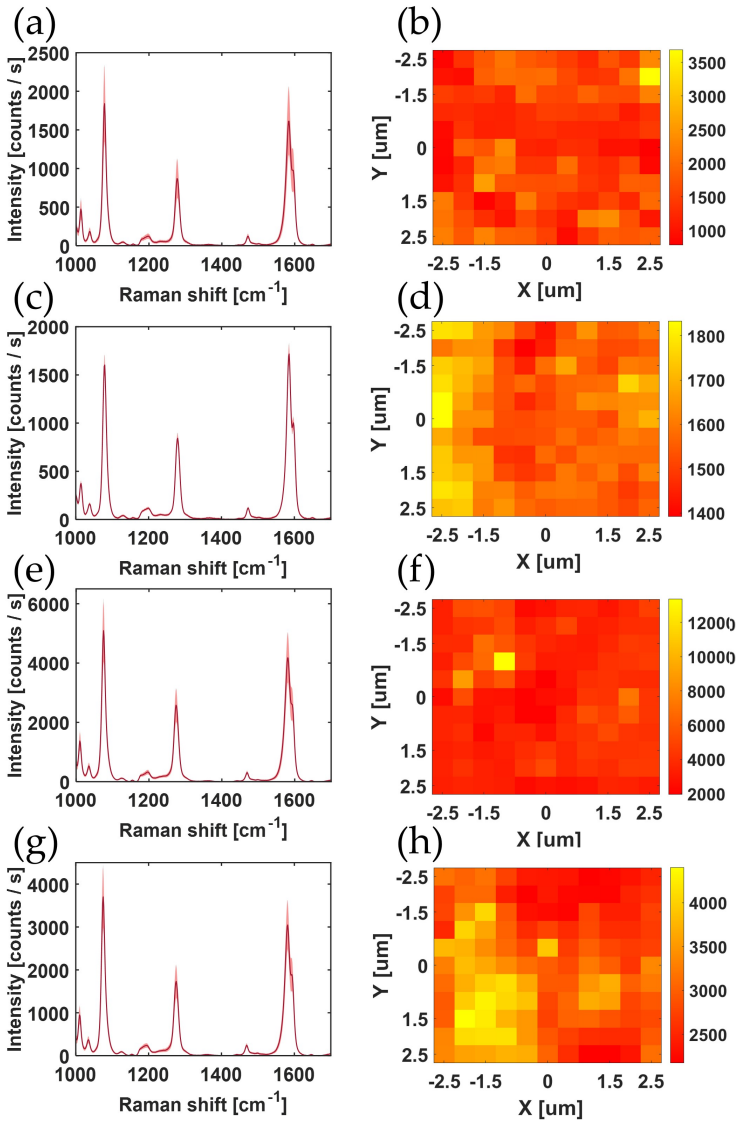

Figure 6.12. Average SERS spectra with standard deviation for SERS active substrates and SERS intensity map at 1585 cm^{-1} on a 5x5 μm^2 area, second acquisition, respectively for: (a-b) CPA, (c-d) HSN1, (e-f) HSN2, (g-h) HSN3.

First, considering only the second acquisitions and making a comparison between the maps of the two fundamental peaks (1080 cm^{-1} and 1585 cm^{-1}) that are acquired in the same region of the sample, it is evident that the hot spots excited are the same for the samples CPA, HSN2 and HSN3 (respectively in figures 6.8 b, f and h and in figures 6.12 b, f and h). Instead for HSN1, the field map acquired at Raman shift at 1585 cm^{-1} (in figure 6.12 d) results in a more homogeneous diffuse intensity than in 1080 cm^{-1} (in figure 6.8 d). Due to a more intense pixel in the field map of the HSN2 field map with reference to the second acquisitions for both peaks analyzed, it is not possible to appreciate the field distribution in the remaining map. Nevertheless, thanks to the morphological analysis carried out in the chapter 5 (figure 5.5 a and b) , it is possible to affirm that the sample is quite homogeneous and actually we see a diffused homogeneity of the intensity in the field map (in figure 6.12 f). In addition, in the second acquisition the HSN2 and HSN3 samples are reduced considering the peak at 1080 cm^{-1} (in figure 6.8 f and h) compared to 1585 cm^{-1} (in figure 6.12 f and h), a phenomenon that also occurs in the first acquisition. This decrease present in both acquisitions, in terms of intensity obtained by comparing the response to the two Raman shifts, basically shows that there is a more intense response at 1080 cm^{-1} than the one at 1585 cm^{-1}.

To better understand and catch the differences and similarities between samples, in the table 6.8 are summarized the main characteristics of the SERS samples analyzed in the second acquisition at Raman shift 1585 cm^{-1}. In the table 6.8 it is possible to notice as the values of peak between the two acquisitions to 1585 cm^{-1} are very near to each other, excluded HSN2 that introduces the greater difference with a decrease of approximately 100 counts/s passing from the first to the second acquisition (which compared to the peak value is about 2.5 %). Instead for the other samples the variation is in average around the 40 counts/s. Consequently also the values of enhancement factor do not differ of a significant digit. The CPA and the HSN3 both increase by a factor of 0.01, while HSN1 and HSN2 samples decrease by a factor of 0.04. Despite these differences, despite decreases in intensity, the results obtained show once again that HSN1 follows the behaviour of CPA, while HSN2 exhibits the best perfor-

mance followed by the HSN3 sample. In fact the HSN2 sample has EF values that are about 2.27 times the CPA values, HSN3 is 1.77 times the CPA. Comparing the performance of the second acquisition between the two peaks 1080 cm^{-1} and 1585 cm^{-1}, there is a general decrease of performance. the sample CPA show a decrease of 8.42 % and the substrate HSN1 of 3.41 %. Meanwhile the decrease is more significant for the sample HSN2 and HSN3, respectively with values of 16.25 % and 10.88 %. Accordingly, the substrate HSN2 exhibits the highest coefficient of variation (σ/μ) of 21 %, respect the data shown in table 6.8. The sample CPA and HSN3 exhibits a similar coefficient of variation, respectively equal to 15 % and 12 %, meanwhile HSN1 has the lowest value equal to 6 %.

Table 6.8. SERS performance estimation for CPA and HSNs substrate in terms of : Peak Intensity, Average Volume Integral and Enhancement Factor, for a Raman shift at 1585 cm^{-1}, related to the second acquisition.

@1585 cm^{-1}	PI $[\mu \pm \sigma]$	$\frac{PI_{HSN}}{PI_{CPA}}$	AVI $[\mu m^3]$	$\frac{AVI_{HSN}}{AVI_{CPA}}$	EF $[10^5]$	$\frac{EF_{HSN}}{EF_{CPA}}$
CPA	1685.82 ± 450.92	1.00	21.40	1.00	0.70	1.00
HSN1	1614.65 ± 86.40	0.96	9.60	0.45	0.72	1.02
HSN2	4072.05 ± 1385.20	2.42	116.10	5.40	1.60	2.27
HSN3	3047.40 ± 574.60	1.81	52.50	2.40	1.25	1.77

To conclude the obtained values of EF reveal that HSNs samples are active substrates and are considered valid for practical use in SERS applications. The substrate that exhibits the best performance is the HSN2 sample, both compared to CPA and other HSNs substrates. The HSNs substrates work better considering the peak corresponding to the Raman shift at 1080 cm^{-1}, compared to 1585 cm^{-1}. The second acquisitions made for both peaks confirm the repeatability and reliability of the results obtained, despite some decreases in peak intensity values.

Chapter 7

Cmos-compatible material for SERS substrates: preliminary analysis

Reproducible SERS substrates play a critical role in SERS detection, helping to mitigate signal fluctuations by either controlling the electromagnetic field of individual metal colloids in single-particle SERS systems or creating well-ordered metal nanoparticles arrays with fixed nanogaps on solid-state substrates [173]. In this context, to overcome limits and create substrates that are reproducible and stable, CMOS (Complementary Metal-Oxide-Semiconductor) technology plays a key role. Microfabrication techniques compatible with CMOS technology, allow to create nanostructured surfaces or features that enhance the Raman scattering signal. CMOS-compatible SERS devices can be fabricated with high precision, allowing for the mass production of highly sensitive and miniaturized SERS sensors, combining the benefits of CMOS technology with the enhanced analytical capabilities of SERS [174]. In visible-wavelength spectra, silver (Ag) and gold (Au) are commonly preferred materials for plasmonic applications due to their low electronic losses. However, a significant challenge arises because Ag and Au are not compatible with CMOS process lines. This incompatibility poses obstacles in the development of cost-effective and large-scale SERS devices. To address this issue while adhering to the strict requirement of using only CMOS-compatible materials, extensive ef-

forts have been dedicated to blending metals with non-metals to create inter-metallic compounds. Researchers have been exploring ways to optimize the optical properties of nitrides, silicides, and germanides to produce materials with low loss. At the Leibniz Institute for High Performance Microelectronics (IHP), the focus has been on developing silicon-based technologies, components, and systems for high-speed communication. In this context, metal germanides and nitrides play a crucial role for SERS applications and also sensing. In this chapter is presented a comparative preliminary analysis of the performance of hierarchical binary structure, considering two alternative materials: nickel germanides (NiGe) and titanium nitrides (TiN). The preliminary analysis is implemented by performing numerical analysis. During a short term scientific collaboration at IHP, the refractive index of the two materials under analysis was acquired using ellipsometry instrumentation. The acquired refractive index has been used to define materials in numerical simulations performed by Comsol multiphysics. The numerically simulated structure is the same as widely described in previous chapter 4, with the difference that instead of using gold the new materials are analyzed. In particular, the considered are the closed packed array (CPA) and the hierarchical nanospheres structure (HSN).

7.1 Ellipsometry: theory and experimental.

Ellipsometry is a powerful and versatile optical technique, useful for material characterization, and has gained widespread recognition in both scientific research and industrial applications. Originally developed in the 20th century, ellipsometry evolved into a sophisticated, non-destructive measurement method that provides information on the optical properties, thickness, and composition of thin films about solid substrates. Ellipsometry is based on the measurement of changes in the state of polarization of light upon reflection or transmission from the analyzed sample. In the figure 7.1 is shown a schematic illustration of the operating mechanism of an ellipsometer, in the classical configuration. By analyzing variations

in amplitude and/or phase of reflected or transmitted light, ellipsometry can provide valuable information on optical constants (as refractive index and/or extinction coefficient), layer thicknesses, and also the structural properties of the materials under consideration. This technique has found applications in a wide range of fields, including material science, semiconductor technology, surface chemistry, and thin film optical sensors, to name a few.

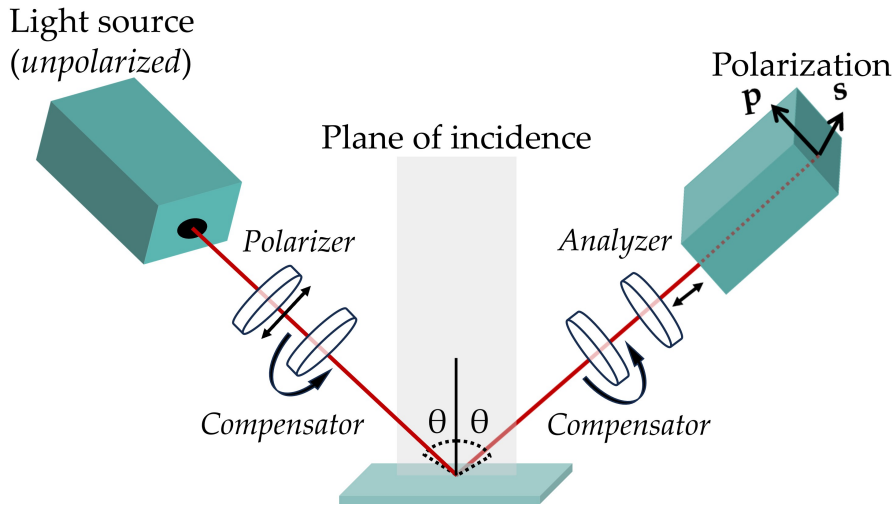

Figure 7.1. Conventional configuration and operating mechanism of a classical ellipsometer.

Basic principles

The ellipsometry is essentially used to characterize and optimize thin film properties for applications such as anti-reflective coatings, optical filters, semiconductor devices, and bio-materials. In addition, its versatility extends to monitoring and optimization of fabrication processes such as deposition or surface modification, making ellipsometry an indispensable tool in the quality control field. When an incident light interact with the sample investigated, the material structure responds with a variation in polarization. The incident light can be decomposed in two contributions:

the "s" and a "p" component. Where "s" is the oscillating component perpendicular to the incident plane and parallel to the sample surface, meanwhile the "p" component is parallel to the incident plane. Normalized to initial value, after the reflection response, the two component are denominated as r_s and r_p, respectively. Keeping in mind the above considerations, evaluated by ellipsometry, the polarization variation can be quantified by measuring the complex reflectance ratio. The complex ratio ρ is defined as the ratio between the quantity r_s and r_p. In details, the complex ratio ρ is equal to:

$$\rho = \frac{r_p}{r_s} = \tan\Psi \cdot e^{i\Delta} \tag{7.1}$$

Where Ψ is the amplitude ratio upon reflection, meanwhile Δ represents the phase shift. Generally, for an-isotropic or non-homogeneous materials, a layer model should be defined as such that it considers the fundamental optical constants (for example, the refractive index) and geometric parameters such as the thickness of all individual layers of the sample and the correct sequence of layers. Using an iterative procedure and gradually varying the values of unknown optical constants and thickness parameters, the Ψ and Δ values are calculated using the Fresnel equations. In the case of isotropic and homogeneous materials, a direct inversion of the parameters Ψ and Δ is simply possible.

7.1.1 Experimental set-up and results

The refractive index acquisition are performed using the spectroscopic ellipsometer (SENTECH Instruments GmbH). In figure 7.2 is represented an image of the instrumentation and the sample. The measurement are made on pieces of wafers, on which are deposited the material object of analysis. In particular, we analyzed the optical proprieties of the titanium nitride (TiN) and nickel germanide (NiGe) layers. For both samples the acquisition were implemented considering multiples angle of incidence (ϑ)

from 60 deg to 70 deg with a step equal to 5 deg. The spectral range of operation goes from 190 nm to 3500 nm. The TiN sample has a nominal thickness of 100 nm, and an effective (measured) thickness of 90.76 nm.

In figure 7.3 are showed the resulting acquisitions of the parameters Ψ and Δ for the titanium nitride. It is interesting to observe that increasing the angle of incidence (ϑ), the quantity Ψ exhibits signals quite similar to each other with a small shift in terms of wavelength (figure 7.3 a), meanwhile the Δ analysis reveals that the signals decrease in terms of intensity with no shift (figure 7.3 b). Above the wavelength equal to 100 nm the response of Ψ and Δ is without significant variation, but show a slight progressive increase of the intensity. The same acquisition is performed for the sample made with nickel germanide and shown in figure 7.4. Con-

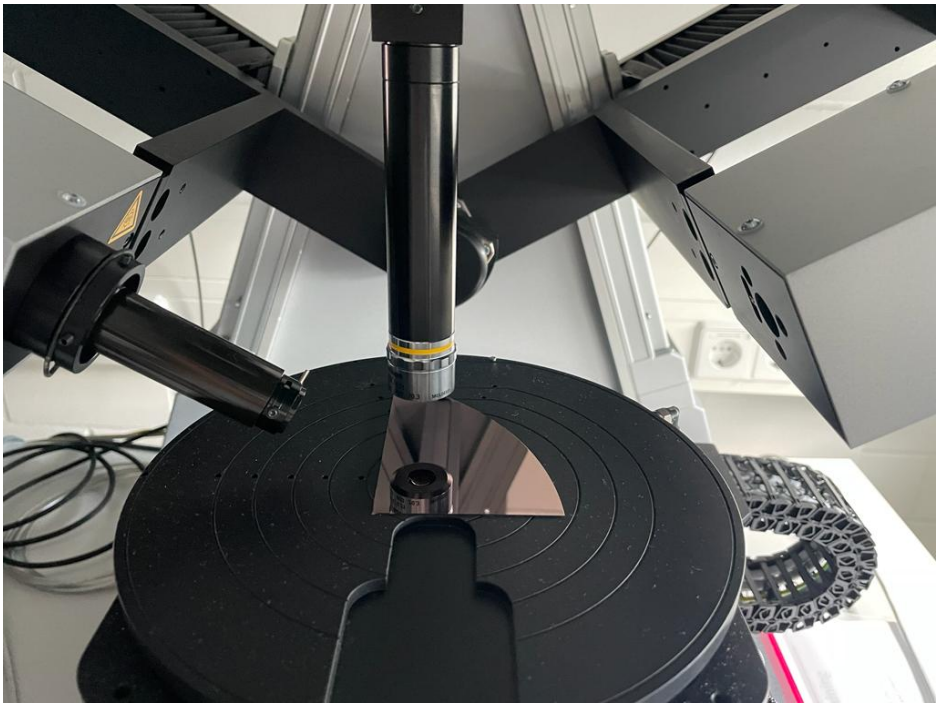

Figure 7.2. Spectroscopic ellipsometer and a sample (SENTECH Instruments GmbH)

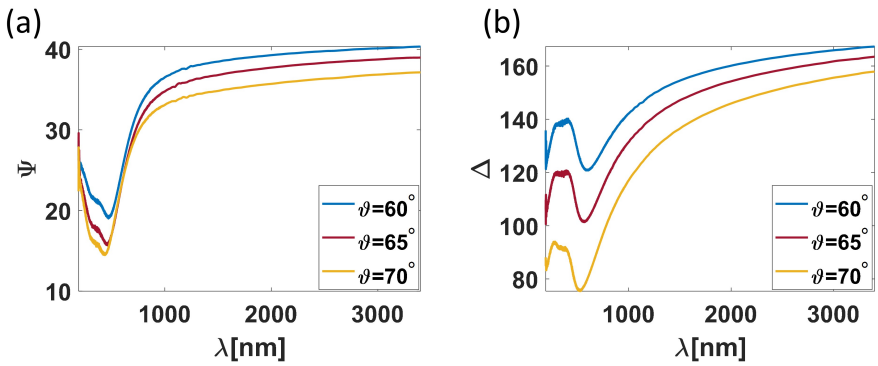

Figure 7.3. The acquisition of Ψ (a) and Δ (b) values for different angle of incidence for the sample TiN.

sidering the figure 7.4 a, the major variation of the Ψ and Δ acquisition are confined in the region of wavelength going from 350 nm to 1500 nm. Under 350 nm, the Ψ signals coincide for the three angles considered. Progressively increasing wavelengths the signals vary significantly up to 1500 nm, showing a decrease in intensity when the angle of incidence increases. Above 1500 nm, the signals became more stable, reducing the intensity discrepancy (increasing the wavelengths). The same phenomena is possible to observe in the Δ signals, shown in figure 7.4 b. In this case under 300 nm the Δ signals retain the intensity variation shown at higher wavelengths, unlike the Ψ signals that are very close to each other. Above 200 nm, the Δ signals is more linear. After an iterative procedure, using know theoretical models for TiN and define new model for NiGe, the refractive index was extracted.

In figure 7.5 are shown the respective real part ("n") and imaginary part ("k") of the complex refractive index for the samples Au (taken from the data set made available from Johnson and Christy [165]) TiN and NiGe (experimentally acquired). For the TiN (figure 7.5 a) was used the Drude model to obtain the complex refractive index, meanwhile for the NiGe was necessary to use the "option" define "new model", considering that there are not know model for this material. The n e k of TiN shown a variability under the wavelength 1000 nm, meanwhile above that the signal are linear and increase with the increasing of the wavelength. The NiGe is purely

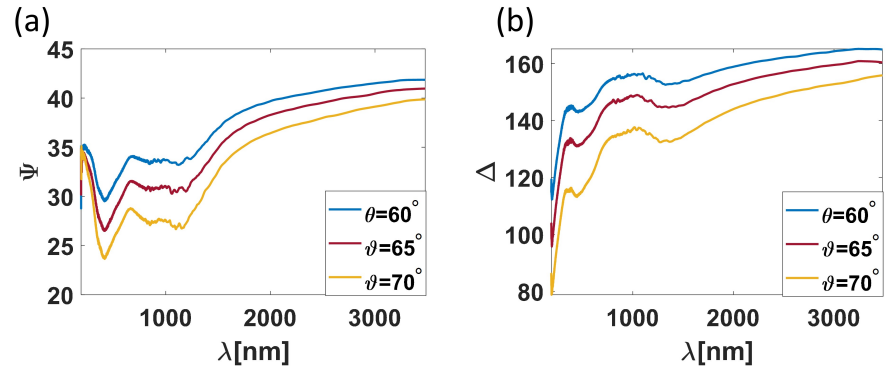

Figure 7.4. The acquisition of Ψ (a) and Δ (b) values for different angle of incidence for the sample NiGe.

constant except in the range from 500 nm to 1100 nm.

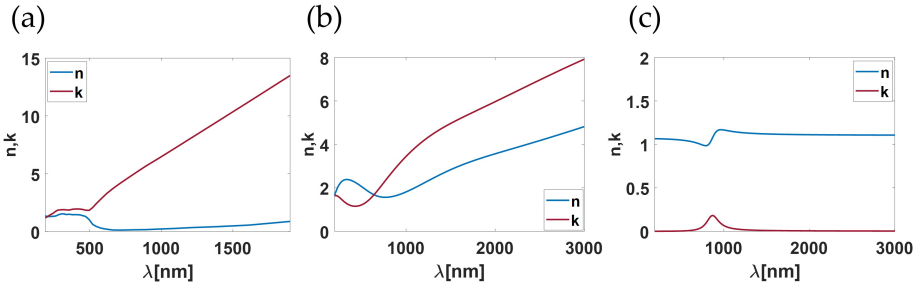

Figure 7.5. The acquisition of n and k values for the : (a) AU, (b) TiN and (c) NiGe.

7.2 Numerical Analysis

The performance analysis of the tested materials were numerically analyzed by modelling two structure using the commercial software Comsol Multyphisics (also proposed in chapter 4). The structure used to evaluate the materials performance are: the structure CPA and a hierarchical nanospheres structure. The hierarchical nanospheres structure is composed by two layer of spheres, where the bottom spheres have a diameter (D_B)

equal to 757 nm and a ratio between the upper and bottom spheres (δ) equal to 0.48. In order to compare the structure according to the method described in chapter 4, the simulation are performed considering the same condition. The mesh, the periodic condition (Floquet boundary condition and port condition with an incident x polarized planar wave) and the dimension of each domain are equal to the structure simulated and described in detail in the chapter4. In figure 7.6 is shown a schematic representation of the structure simulated, resuming the principal characteristic.
Over the polystyrene spheres is considered a layer of 30 nm made first with TiN and then with NiGe, for both the structure. To define the materials were used the refractive index acquired experimentally in the previous paragraph. For each sample is evaluated the volume integral, calculated on the conformal layer (made of air and with a thickness of 10 nm), of the fourth power of the ratio between the electromagnetic local field on incident field. In the figure 7.7 is reported the spectra (reflectivity and volume integral) of the CPA simulated considering a layer made of Au (figure 7.7

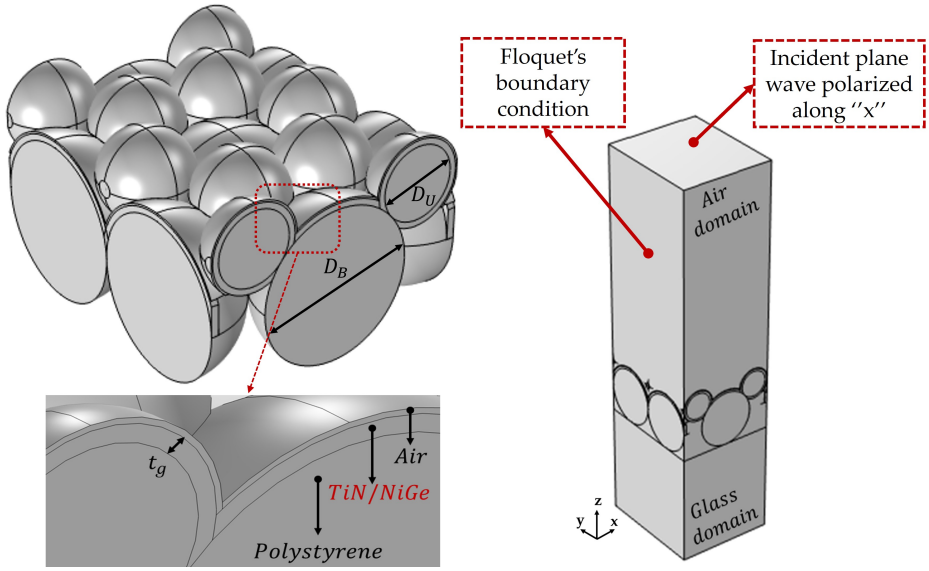

Figure 7.6. Schematic representation of the simulated hierarchical structure, showing the main characteristics.

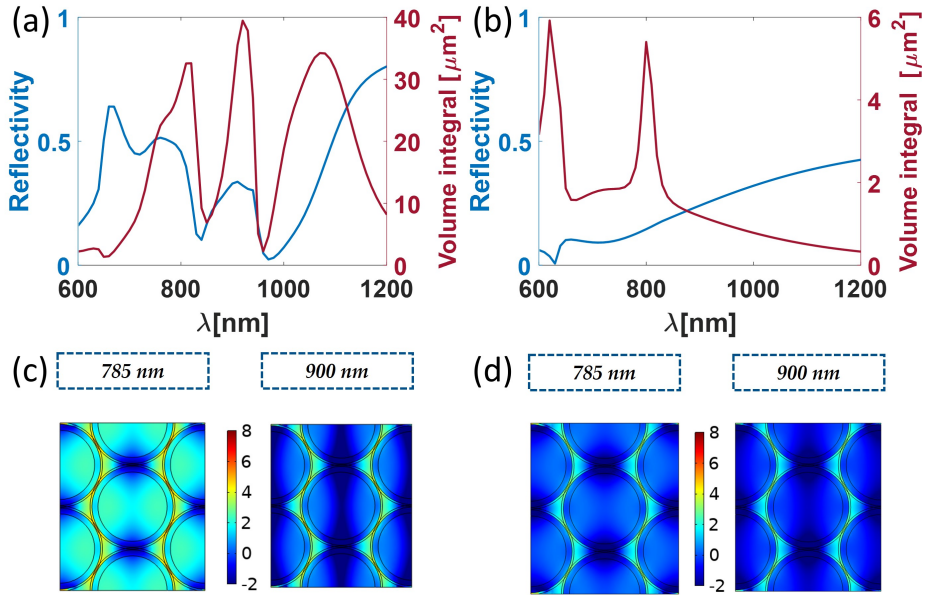

Figure 7.7. Numerical reflectivity and volume integral for SERS active substrates CPA with: (a) Au, (b) TiN; electromagnetic field distribution normalized to the incident light intensity along the xy cut plane with: (c) Au, (d) TiN

a), compered with a structure containing a layer of Tin (figure 7.7 b). Compering to Au, the CPA with TiN exhibits a general lower intensity. In particular, the maximum intensity value for TiN, reached at 620 nm, is 5.9 μm^2, around 6 times less than the maximum reached by Au (equal to 39 μm^2 at 920 nm). The CPA with Au shows two side peak with a value equal to 32 μm^2 and 34 μm^2 (at 810 nm and 1070 nm, respectively),

that are 5-6 times greater than the maximum intensity obtained with TiN. In figure 7.7 c and d are shown the electromagnetic field distribution along the xy cut plane for Au and TiN, respectively. Despite changing the material, the maps reveal that the tin can turn on the same hot spots of the Au-CPA, even if in reduced intensity. The reflectivity and the volume integral for the structure HSN are shown in figure 7.8 a for Au and in figure 7.8 b for TiN. In this case the response of TiN appears to be worse compered to HSN with Au, meanwhile exhibits an increase in terms of

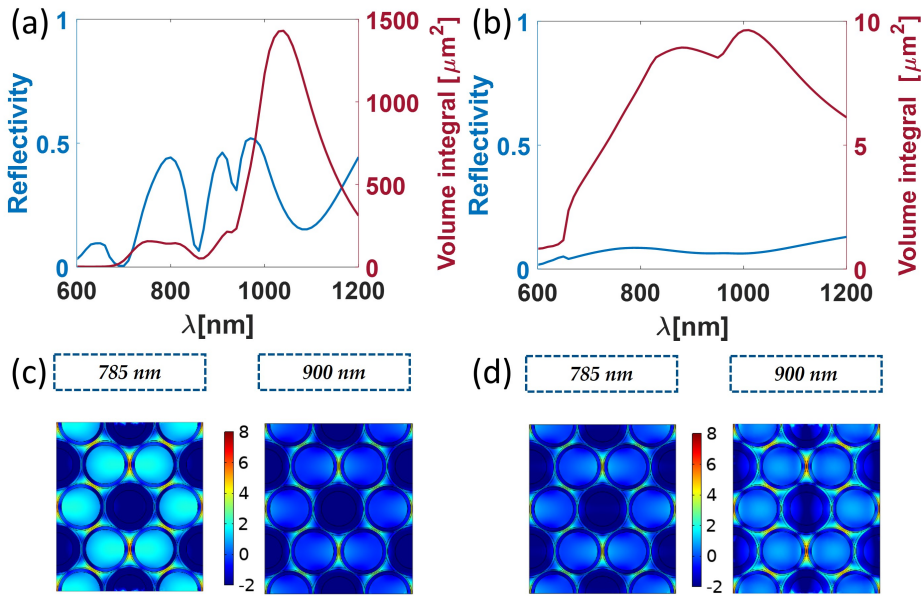

Figure 7.8. Numerical reflectivity and volume integral for SERS active substrates HSN with: (a) Au, (b) TiN; electromagnetic field distribution normalized to the incident light intensity along the xy cut plane with: (c) Au, (d) TiN

intensity respect the structure CPA with TiN. The intensity increasing is around a value of 0.3, in fact the maximum value is about 9.6 μm^2. Despite this increase, comparing the performance of the HSN structure with Au, we see that the TiN has a peak value of about 149 times lower. Meanwhile in figure 7.8 c and d are reported the electromagnetic field map at 785 nm and 900 nm for the Au-HSN and TiN-HSN, respectively.
As for the CPA, the HSN structure (considering Au and TiN) are more intense at 900 nm respect 785 nm, exhibiting the same hot spots. In the table 7.1 are resumed the principal characteristic of the structure under analysis: the geometrical characteristic, the material and the average volume integral. Evaluated in the range from 785 nm to 910 nm, the average volume integral is used to compared the performance between the substrate. In this range, the structure with TiN keep the trend that the structure HSN is better respect the CPA (trend arise in the analysis made

in chapter 4 and chapter 6). The HSN is 5.4 and 3.7 times greater than the CPA, considering the gold and the TiN respectively. The loss of performance is evident pass from Au to TiN. In fact the HSN with Au shown a AVI equal to 116.08 μm^2, respect the AVI of TiN (8.35 μm^2) is 139 times higher. Considering the sample chosen HSN represents the optimal structure for gold, obtained following a thorough numerical analysis, the optimum for HSN-TiN may not coincide with the one for gold. Despite the above observation, even in this case, the HSN structure proves to have better performance than the CPA structure.

Table 7.1. SERS performance estimation for CPA and HSN substrate in terms of Average Volume Integral, considering Au and Tin as material.

Name	D_B $[nm]$	δ	Material	AVI $[10^{-17}]$	$\frac{AVI_{HSN}}{AVI_{CPA}}$
CPA	757	-	Au	21.41	-
CPA	757	-	TiN	2.25	-
HSN	757	0.48	Au	116.08	5.396
HSN	757	0.48	TiN	8.35	3.709

The above analysis is also implemented for the NiGe, which refractive index is experimentally acquired (in the previous paragraph, shown in figure 7.5 b) and used to perform the following simulation, in the same condition (CPA compered to HSN). The reflectivity and volume integral are shown for the structure CPA in figure 7.9 a for Au and figure 7.9 b for NiGe.

In figure 7.9 c and d are reported the electromagnetic field map, normalized to incident field at 785 nm and 900 nm for the CPA with Au and NiGe, respectively. The reflectivity of NiGe appears to be quite linear with general value under the 0.3, unlike the one of Au-CPA . The volume integral exhibits two main peak at 612 nm and 720 with an intensity value equal to 3750 μm^2 and 3320 μm^2 respectively. Considering the structure with Au the volume integral is two order of magnitude lower than the NiGe. In figure 7.9 d, the electromagnetic field intensity maps oh NiGe-CPA shows hot

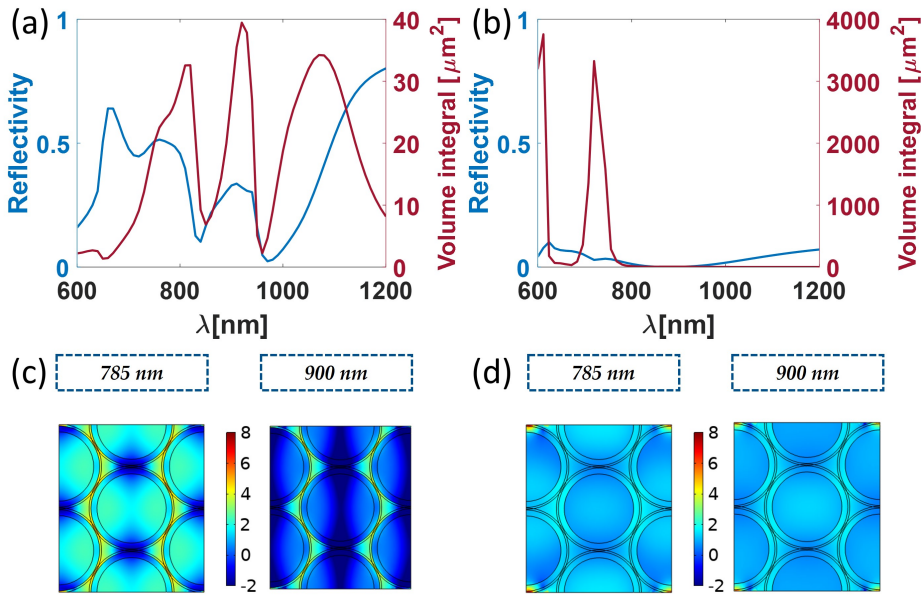

Figure 7.9. Numerical reflectivity and volume integral for SERS active substrates CPA with: (a) Au, (b) NiGe; electromagnetic field distribution normalized to the incident light intensity along the xy cut plane with: (c) Au, (d) NiGe.

spots, equal in number but in reduced intensity compared to Au (in figure 7.9 c). This phenomenon is explainable considering that the volume integral of Nige shows very intense peaks localized in the range of wavelengths below 780 nm. Indeed, for the Au-CPA structure electromagnetic maps reveal well-defined and intended hot spots, keeping in mind that the volume integral shows very intense peaks around 785 nm and 900 nm. In the figure 7.10 a and b are reported the reflectivity and the volume integral of the structure HSN, simulated with Au and NiGe respectively. In this case the performance look like their are inverted respect the previously substrates. In particular, the HSN with Au shows a volume integral higher than the NiGe about three order of magnitude. The main responsiveness of the Au HSN structure is principally in the wavelength region going from 950 nm to 1100 nm. For Au, the maximum intensity peak is equal to 1430 μm^2 at 1030 nm, exhibiting a bandwidth of approximately 200 nm. Meanwhile,

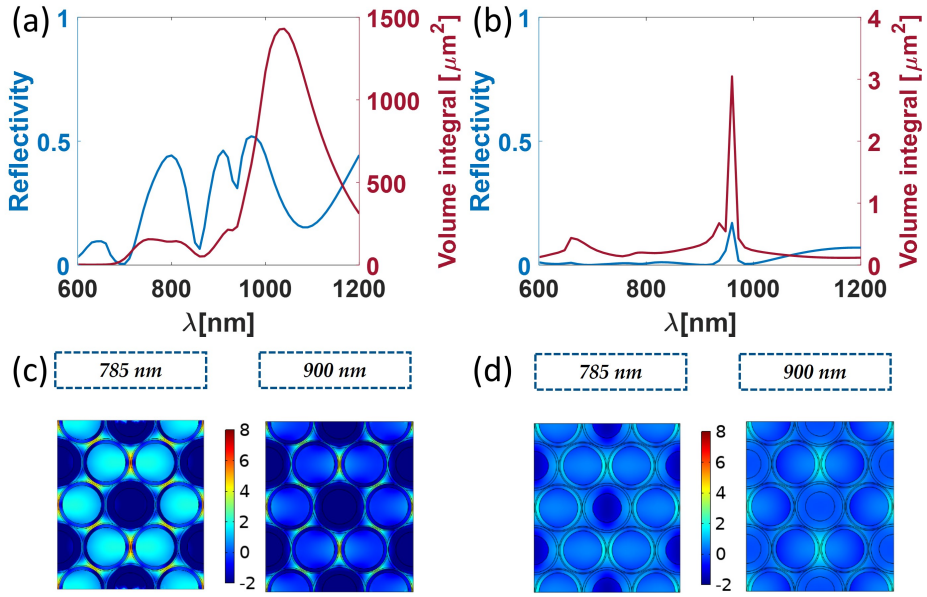

Figure 7.10. Numerical reflectivity and volume integral for SERS active substrates HSN with: (a) Au, (b) NiGe; electromagnetic field distribution normalized to the incident light intensity along the xy cut plane with: (c) Au, (d) NiGe.

the NiGe substrate exhibits a thin peak with a maximum value of intensity equal to 3 μm^2. The NiGe HSN structure compared to NiGe CPA shown a decrease of performance. In figure 7.10 c and d , it is interesting to observe the electromagnetic fild distribution for Au-HSN and NiGe-HSN, respectively. Whereas the volume integral has a single peak around 3 μm^2 at 960 nm, while the for the rest of the band has a value lower than 0.5 μm^2, the field maps show hot spots with extraordinarily lower intensity than the maps of the Au-HSN. In the table 7.2 are listed the main characteristic of the above structure. The AVI of the Au-CPA structure results to be two times the AVI of the NiGe-CPA. Considering the figure 7.9, the highest response of the structure is located in the region before the wavelength 770 nm. Above the wavelength 770 nm, the performance appears to be worse than the Au-CPA. The NiGe-HSN structure show a lower performance respect the NiGe-CPA, exhibiting a AVI ratio equal to 0.02, against

the AVI Au ratio equal to 5.39. The overall performance of the analyzed materials (TiN and NiGe) is quite poor compared to gold. Keeping in mind that the working range of nickel germanide is the medium infrared, considering that the structure used for comparative analysis represents the optimal structure with gold, despite the obtuse performance, the materials are to be deepened in the study. In fact, in future objectives are part of the study of materials expanding/varying the range of wavelengths in the medium infrared and verify that the performance of other structures HSN (varying diameters) with the above materials. In other words, thanks to the study of geometries, field maps and volume integral, the aim will be to try to effect resonance tuning for Nige (the most promising material). By carrying out an in-depth study and fine tuning of the characteristic resonances, the potential expressed in part by the analysed structures can be fully exploited.

Table 7.2. SERS performance estimation for CPA and HSN substrate in terms of Average Volume Integral for Au and NiGe.

Name	D_B $[nm]$	δ	Material	AVI $[10^{-17}]$	$\frac{AVI_{HSN}}{AVI_{CPA}}$
CPA	757	-	Au	21.41	-
CPA	757	-	NiGe	11.89	-
HSN	757	0.48	Au	116.08	5.396
HSN	757	0.48	NiGe	0.23	0.02

Chapter 8

Conclusions

In the previous chapters a numerical and experimental analysis related to the hierarchical structures based on nanospheres, as economic SERS-active substrates, was presented. The hierarchical architecture allows to increase the number and overall spatial density of hot spots, taking advantage of additional hot spots formed in the off-plane dimension. A large set of substrates, varying geometric parameters were considered for the study of the electromagnetic field, with particular attention to the contribution made to the enhancement SERS in a limited region near the surface of gold (of thickness 10 nm). As a simple method to easily compare different SERS substrates from the point of view of performance in the fingerprint region, AVI was used. The general conditions necessary to obtain a performance enhancement (compared to the classical CPA structure) are defined by numerical analysis. A regular nanogaps model with intense hot spots is achieved thanks to the provided geometric constraints. To provide a regular model of HSN substrates two experimental approaches have been studied in detail. Morphological analysis shows that it is possible to obtain HSN structures with a regular pattern with intense and dense hot spots, taking advantage of a convenient fabrication path. Beside, SERS spectroscopic analysis revealed that HSN function as active SERS substrates. In addition, compared to the simpler CPA substrates, a performance enhancement of HSN structures was observed in terms of average SERS intensity, of even a factor 3. The numerical model predicted that there are structures with even higher enhancement than those obtained experimentally.

However, the inherent variability in the initial nanospheres diameters prevents the achievement of even more intense hot spots. In fact, this intrinsic variability leads to random fluctuations in nanogaps between nanospheres and contributes to rather uneven SERS responses. By reducing manufacturing tolerances in terms of nanospheres diameters, further enhancement could be achieved. To overcome the limitations associated with fairly small nanogaps variability, alternatively, pointed an-isotropic structures could be used. The numerical and experimental survey reported, hopes that it can provide guidance to improve the performance of existing SERS substrates and overcome them by creating new substrates with better performance. To exploit the regularity of the model used as a substrate for SERS, a hierarchical structure should be conceived with judgment. The bottom layer of the basic structure can serve as a model for creating an additional top layer of hot spots. By increasing the number of hot spots or creating a series of more intense hot spots, the hierarchical top layer of hot spots can work to completely surpass the performance of previous ones structures. Simultaneously, a comparative preliminary analysis of the performance of hierarchical binary structure, considering two alternative materials: nickel germanides (NiGe) and titanium nitrides (TiN) was implemented. Considering that the gold is not compatible with CMOS process lines, obstacles were posed in the development of cost-effective and large-scale SERS devices. Efforts have been dedicated to find an alternative to blending metals with non-metals, to overcome the above limitations. In this context, nickel germanides and titanium nitrides play a crucial role offering a solution. The outcomes of the preliminary numerical analysis performed stand on this way, identifing the nickel germanides as promising material. In the future, a numerical study will certainly have to be carried out to synchronize the response due to the optical properties of the material and the influence of the geometry to obtain the best structure with the nickel germanides.

Bibliography

[1] J. Dong, C. Yang, H. Wu, Q. Wang, Y. Cao, Q. Han, W. Gao, Y. Wang, J. Qi, and M. Sun, "Two-dimensional self-assembly of au@ag core–shell nanocubes with different permutations for ultrasensitive sers measurements," *ACS Omega*, vol. 7, pp. 3312 – 3323, 2022.

[2] Y. H. Lee, C. L. Lay, W. Shi, H. K. Lee, Y. Yang, S. Li, and X. Y. Ling, "Creating two self-assembly micro-environments to achieve supercrystals with dual structures using polyhedral nanoparticles," *Nature Communications*, vol. 9, 2018.

[3] X. Xin, Y. Li, L. Yu, W. Li, J. Li, and R. Lu, "Facile synthesis of ag@c@ag hybrid nanoparticles as sers substrate," *Analytical and Bioanalytical Chemistry*, vol. 413, pp. 5767 – 5777, 2021.

[4] A. R. Kosiorek, W. Kandulski, H. Glaczynska, and M. Giersig, "Fabrication of nanoscale rings, dots, and rods by combining shadow nanosphere lithography and annealed polystyrene nanosphere masks.," *Small*, vol. 1 4, pp. 439–44, 2005.

[5] X. Fu, Z. Wang, J. Li, S. Ma, G. Fu, W. Jin, W. Bi, and Y. Dong, "Microcavity fiber sers probe coated with ag nanoparticles for detecting antibiotic in milk," *IEEE Photonics Journal*, vol. 13, pp. 1–13, 2021.

[6] L. Zha, X. Fang, Y. Han, and X. Zhang, "Controlled fiber core mode and surface mode interaction for enhanced sers performance.," *Optics express*, vol. 30 25, pp. 44827–44836, 2022.

[7] B. Huang, K. Yang, Y. Zhu, and J. Zhang, "Microfluidic integrated d-shaped optical fiber sers probe with high sensitivity and ability of multimolecule detection," *Optics Express*, 2023.

[8] Y. Long, H. Li, Z. Du, M. Geng, and Z. Liu, "Confined gaussian-distributed electromagnetic field of tin(ii) chloride-sensitized surface-enhanced raman scattering (sers) optical fiber probe: From localized surface plasmon resonance (lspr) to waveguide propagation.," *Journal of colloid and interface science*, vol. 581 Pt B, pp. 698–708, 2020.

[9] A. Kohut, V. Horváth, Z. Pápa, B. Vajda, J. Kopniczky, G. Galbács, and Z. Geretovszky, "One-step fabrication of fiber optic sers sensors via spark ablation," *Nanotechnology*, vol. 32, 2021.

[10] J. A. Kim, D. J. Wales, A. J. Thompson, and G. Yang, "Fiber-optic sers probes fabricated using two-photon polymerization for rapid detection of bacteria," *Advanced Optical Materials*, vol. 8, 2020.

[11] V. S. Tiwari, R. R. Kalluru, F.-Y. Yueh, J. P. Singh, and S. K. Khijwania, "Designing of a prototype fiber optic raman sensor," 2005.

[12] R. M. Willes H. Weber, *Raman Scattering in Materials Science*. Springer Berlin, Heidelberg, 2013.

[13] J. Kneipp, H. Kneipp, and K. D. Kneipp, "Sers–a single-molecule and nanoscale tool for bioanalytics.," *Chemical Society reviews*, vol. 37 5, pp. 1052–60, 2008.

[14] A. Jaworska, S. Fornasaro, V. Sergo, and A. Bonifacio, "Potential of surface enhanced raman spectroscopy (sers) in therapeutic drug monitoring (tdm). a critical review," *Biosensors*, vol. 6, 2016.

[15] N. E. Markina, S. N. Ustinov, A. M. Zakharevich, and A. V. Markin, "Copper nanoparticles for sers-based determination of some cephalosporin antibiotics in spiked human urine.," *Analytica chimica acta*, vol. 1138, pp. 9–17, 2020.

[16] S. Lee, S. Kim, J. Choo, S. Y. Shin, Y. H. Lee, H. Y. Choi, S. Ha, K. Kang, and C. H. Oh, "Biological imaging of hek293 cells expressing plcgamma1 using surface-enhanced raman microscopy.," *Analytical chemistry*, vol. 79 3, pp. 916–22, 2007.

[17] S. Dong, D. He, Q. Zhang, C. Huang, Z. Hu, C. Zhang, L. Nie, K. Wang, W. Luo, J. Yu, B. Tian, W. Wu, X. Chen, F. Wang, J. Hu, and X. Xiao, "Early cancer detection by serum biomolecular fingerprinting spectroscopy with machine learning," *eLight*, vol. 3, 2023.

[18] Z. Huang, G. Meng, Q. Huang, B. Chen, Y. Lu, Z. Wang, X. Zhu, and K. Sun, "Surface-enhanced raman scattering from plasmonic ag-nanocube@au-nanospheres core@satellites," *Journal of Raman Spectroscopy*, vol. 48, pp. 217–223, 2017.

[19] M. Pisco and F. Galeotti, "Nano- and micropatterning on optical fibers by bottom-up approach: The importance of being ordered," *Applied Sciences*, vol. 11, p. 3254, 2021.

[20] F. L. Yap, P. Thoniyot, S. Krishnan, and S. Krishnamoorthy, "Nanoparticle cluster arrays for high-performance sers through directed self-assembly on flat substrates and on optical fibers.," *ACS nano*, vol. 6 3, pp. 2056–70, 2012.

[21] J. Ko, S. Park, S. Lee, X. Wang, C. Mun, S. Kim, D.-H. Kim, and J. Choo, "Culture-free detection of bacterial pathogens on plasmonic nanopillar arrays using rapid raman mapping.," *ACS applied materials & interfaces*, vol. 10 8, pp. 6831–6840, 2018.

[22] B. Xu, J. He, B. Du, X. Xiao, X. Xu, C. Fu, J. He, C. Liao, and Y. Wang, "Femtosecond laser point-by-point inscription of an ultra-weak fiber bragg grating array for distributed high-temperature sensing.," *Optics express*, vol. 29 20, pp. 32615–32626, 2021.

[23] D. Jonker, L. J. Kooijman, Y. Pordeli, B. Y. van der Wel, E. J. W. Berenschot, B. T. Borgelink, H. Le-The, M. D. Boer, J. C. T. Eijkel, R. J. E. Hueting, R. M. Tiggelaar, A. van Houselt, H. Gardeniers, and N. R. Tas, "Wafer-scale fabrication and modification of silicon nano-pillar arrays for nanoelectronics, nanofluidics and beyond," *International Journal of Nanotechnology*, 2020.

[24] A. Sharma, A. Jaiswal, and R. P. Jaiswal, "Fabrication of a tailorable polystyrene nanoscale mesh of honeycomb morphology using nano sphere lithography," *Thin Solid Films*, 2022.

[25] M. Pisco, F. Galeotti, G. Quero, G. Grisci, A. Micco, L. V. Mercaldo, P. D. Veneri, A. Cutolo, and A. Cusano, "Nanosphere lithography for optical fiber tip nanoprobes," *Light, Science & Applications*, vol. 6, 2016.

[26] S. Managò, G. Quero, G. Zito, G. Tullii, F. Galeotti, M. Pisco, A. C. D. Luca, and A. Cusano, "Tailoring lab-on-fiber sers optrodes towards biological targets of different sizes," *Sensors and Actuators B: Chemical*, 2020.

[27] J. Luo, C. Wen, Z. H. Zhu, and J. Zhang, "Low loss ultra-smooth gold films for two-dimensional material plasmonic devices," in *Other Conferences*, 2021.

[28] H. Pu, W. Xiao, and D. Sun, "Sers-microfluidic systems: A potential platform for rapid analysis of food contaminants," *Trends in Food Science and Technology*, vol. 70, pp. 114–126, 2017.

[29] T.-S. Kang, Y. Cho, K. M. Yuk, C. Y. Yu, S. H. Choi, and K. M. Byun, "Fabrication and characterization of novel silk fiber-optic sers sensor with uniform assembly of gold nanoparticles," *Sensors (Basel, Switzerland)*, vol. 22, 2022.

[30] M. Moskovits, "Surface-enhanced spectroscopy," *Rev. Mod. Phys.*, vol. 57, pp. 783–826, Jul 1985.

[31] A. M. M. Fleischmann, P.J. Hendra, "Raman spectra of pyridine adsorbed at a silver electrode," *Chemical Physics Letters*, vol. 26, pp. 163–166, 1974.

[32] J. W. Strutt, "Xv. on the light from the sky, its polarization and colour," *Philosophical Magazine Series 1*, vol. 41, pp. 107–120, 1871.

[33] R. S. Krishnan and R. K. Shankar, "Raman effect: History of the discovery," *Journal of Raman Spectroscopy*, vol. 10, pp. 1–8, 1981.

[34] C. V. S. Raman and K. S. Krishnan, "A new type of secondary radiation," *Nature*, vol. 121, pp. 501–502, 1928.

[35] G. W. Auner, S. K. Koya, C. Huang, B. Broadbent, M. Trexler, Z. Auner, A. Elias, K. C. Mehne, and M. A. Brusatori, "Applications of raman spectroscopy in cancer diagnosis," *Cancer Metastasis Reviews*, vol. 37, pp. 691 – 717, 2018.

[36] R. P. V. Duyne, D. L. R. Jeanmaire, and D. F. Shriver, "Mode-locked laser raman spectroscopy. new technique for the rejection of interfering background luminescence signals," *Analytical Chemistry*, vol. 46, pp. 213–222, 1974.

[37] T. D. O. H. J. Toporski, *Confocal Raman Microscopy*, vol. 158. Springer Series in Optical Sciences, 2011.

[38] S. Ding, E.-M. You, Z. qun Tian, and M. Moskovits, "Electromagnetic theories of surface-enhanced raman spectroscopy.," *Chemical Society reviews*, vol. 46 13, pp. 4042–4076, 2017.

[39] J. Langer, D. J. de Aberasturi, J. Aizpurua, R. A. Álvarez-Puebla, B. Auguié, B. Auguié, J. J. Baumberg, G. C. Bazan, S. E. J. Bell, A. Boisen, A. G. Brolo, J. Choo, D. Cialla-May, D. Cialla-May, V. Deckert, V. Deckert, L. Fabris, K. Faulds, F. J. G. de Abajo, R. Goodacre, D. Graham, A. J. Haes, C. L. Haynes, C. Huck, T. Itoh, M. Käll, J. Kneipp, N. A. Kotov, H. Kuang, E. C. L. Ru, E. C. L. Ru, H. K. Lee, J. feng Li, X. Y. Ling, S. A. Maier, T. G. Mayerhöfer, T. G. Mayerhöfer, M. Moskovits, K. Murakoshi, J. Nam, S. Nie, Y. Ozaki, I. Pastoriza-Santos, J. Pérez-Juste, J. Popp, J. Popp, A. Pucci, S. Reich, B. Ren, G. C. Schatz, T. O.

Shegai, S. Schlücker, L. Tay, K. G. Thomas, Z. qun Tian, R. P. V. Duyne, T. Vo-Dinh, Y. Wang, K. A. Willets, C. Xu, H. Xu, Y. Xu, Y. S. Yamamoto, B. Zhao, L. M. Liz-Marzán, and L. M. Liz-Marzán, "Present and future of surface-enhanced raman scattering," *ACS Nano*, vol. 14, pp. 28 – 117, 2019.

[40] H. K. Katrin Kneipp, Martin Moskovits, *Surface-Enhanced Raman Scattering*. Springer Berlin, Heidelberg, 2010.

[41] J.-P. Su, Y.-T. Lee, S.-Y. Lu, and J. S. Lin, "Chemical mechanism of surface-enhanced raman scattering spectrum of pyridine adsorbed on ag cluster: Ab initio molecular dynamics approach," *Journal of Computational Chemistry*, vol. 34, pp. 2806 – 2815, 2013.

[42] Y. Zhao, X. Liu, D. Y. Lei, and Y. Chai, "Effects of surface roughness of ag thin films on surface-enhanced raman spectroscopy of graphene: spatial nonlocality and physisorption strain.," *Nanoscale*, vol. 6 3, pp. 1311–7, 2014.

[43] J. M. Brockman, B. P. Nelson, and R. M. Corn, "Surface plasmon resonance imaging measurements of ultrathin organic films.," *Annual review of physical chemistry*, vol. 51, pp. 41–63, 2003.

[44] S. Zeng, D. Baillargeat, H. Ho, and K. Yong, "Nanomaterials enhanced surface plasmon resonance for biological and chemical sensing applications.," *Chemical Society reviews*, vol. 43 10, pp. 3426–52, 2014.

[45] G. Du, T. Mori, M. Suzuki, S. hachiro Saito, H. Fukuda, and M. Takahashi, "Evidence of localized surface plasmon enhanced magneto-optical effect in nanodisk array," *Applied Physics Letters*, vol. 96, p. 081915, 2010.

[46] B. Li, S. Liu, L. Huang, M. Jin, and J. Wang, "Nanohybrid sers substrates intended for food supply chain safety," *Coordination Chemistry Reviews*, 2023.

[47] J. P. Marton and B. D. Jordan, "Optical properties of aggregated metal systems: Interband transitions," *Physical Review B*, vol. 15, pp. 1719–1727, 1977.

[48] T. A. Klar, A. V. Kildishev, V. P. Drachev, and V. M. Shalaev, "Negative-index metamaterials: Going optical," *IEEE Journal of Selected Topics in Quantum Electronics*, vol. 12, pp. 1106–1115, 2006.

[49] H.-K. Yuan, U. K. Chettiar, W. Cai, A. V. Kildishev, A. Boltasseva, V. P. Drachev, and V. M. Shalaev, "A negative permeability material at red light.," *Optics express*, vol. 15 3, pp. 1076–83, 2006.

[50] T. W. Ebbesen, T. W. Ebbesen, H. J. Lezec, H. F. Ghaemi, T. Thio, P. A. Wolff, and P. A. Wolff, "Extraordinary optical transmission through sub-wavelength hole arrays," *Nature*, vol. 391, pp. 667–669, 1998.

[51] S. A. Maier, *Plasmonics: Fundamentals and Applications*. 2007.

[52] P. Tobiska, O. Hugon, A. Trouillet, and H. Gagnaire, "An integrated optic hydrogen sensor based on spr on palladium," *Sensors and Actuators B-chemical*, vol. 74, pp. 168–172, 2001.

[53] V. P. Drachev, U. K. Chettiar, A. V. Kildishev, H.-K. Yuan, W. Cai, and V. M. Shalaev, "The ag dielectric function in plasmonic metamaterials.," *Optics express*, vol. 16 2, pp. 1186–95, 2008.

[54] S. K. So, H. H. Fong, and N. H. H. Cheung, "Growth and characterization of semicontinuous metal films by pulsed laser ablation," *MRS Proceedings*, vol. 672, 2001.

[55] A. K. Sarychev and V. M. Shalaev, "Electrodynamics of metamaterials," 2007.

[56] G. H. Chan, J. R. Zhao, E. M. Hicks, G. C. Schatz, and R. P. V. Duyne, "Plasmonic properties of copper nanoparticles fabricated by nanosphere lithography," *Nano Letters*, vol. 7, pp. 1947–1952, 2007.

[57] C. Langhammer, M. Schwind, B. Kasemo, and I. Zorić, "Localized surface plasmon resonances in aluminum nanodisks.," *Nano letters*, vol. 8 5, pp. 1461–71, 2008.

[58] J. H. Mokkath, "Localized surface plasmon resonances in a hybrid structure consisting of a mono-layered al sheet and ti3c2f mxene.," *Physical chemistry chemical physics : PCCP*, 2022.

[59] M. Xuelin, Z. Xiaoyong, H. Limin, H. Zhanzhong, and Y. Shengli, "A multi-response aluminum metal-organic frameworks for fluorescence sensing of fe3+, sr2+, sio32-and toluene.," *Methods and applications in fluorescence*, 2021.

[60] Y.-L. Chang, C.-J. Su, L.-C. Lu, and D. Wan, "Aluminum plasmonic nanoclusters for paper-based surface-enhanced raman spectroscopy.," *Analytical chemistry*, 2022.

[61] G. V. Naik, V. M. Shalaev, and A. Boltasseva, "Alternative plasmonic materials: Beyond gold and silver," *Advanced Materials*, vol. 25, 2013.

[62] J. M. McMahon, G. C. Schatz, and S. K. Gray, "Correction: Plasmonics in the ultraviolet with the poor metals al, ga, in, sn, tl, pb, and bi.," *Physical chemistry chemical physics : PCCP*, vol. 17 29, pp. 19670–1, 2015.

[63] A. Ahmadivand, R. Sinha, B. Gerislioglu, M. Karabiyik, N. Pala, and M. S. Shur, "Transition from capacitive coupling to direct charge transfer in asymmetric terahertz plasmonic assemblies.," *Optics letters*, vol. 41 22, pp. 5333–5336, 2016.

[64] G. H. Chan, J. R. Zhao, G. C. Schatz, and R. P. V. Duyne, "Localized surface plasmon resonance spectroscopy of triangular aluminum nanoparticles," *Journal of Physical Chemistry C*, vol. 112, pp. 13958–13963, 2008.

[65] M. E. King, M. F. Guzman, and M. B. Ross, "Material strategies for function enhancement in plasmonic architectures.," *Nanoscale*, 2022.

[66] E. Dumiszewska, P. Caban, I. Jóźwik, P. Ciepielewski, and J. M. Baranowski, "Mocvd growth of gallium and indium microparticles for sers applications," *Journal of Materials Science: Materials in Electronics*, vol. 32, pp. 8958 – 8964, 2021.

[67] Y. Kumamoto, A. Taguchi, N. I. Smith, and S. Kawata, "Deep uv resonant raman spectroscopy for photodamage characterization in cells," *Biomedical Optics Express*, vol. 2, pp. 927 – 936, 2011.

[68] J. S. Biggins, S. Yazdi, and E. Ringe, "Magnesium nanoparticle plasmonics.," *Nano letters*, vol. 18 6, pp. 3752–3758, 2018.

[69] J. Toudert and R. Serna, "Interband transitions in semi-metals, semiconductors, and topological insulators: A new driving force for plasmonics and nanophotonics," *arXiv: Optics*, 2017.

[70] S. A. Kovalenko, "Optical properties of thin metal films," *Semiconductor physics, quantum electronics and optoelectronics*, vol. 2, pp. 13–20, 1999.

[71] X. Ling, L. Xie, Y. Fang, H. Xu, H. Zhang, J. Kong, M. S. Dresselhaus, J. Zhang, and Z. Liu, "Can graphene be used as a substrate for raman enhancement?," *Nano letters*, vol. 10 2, pp. 553–61, 2010.

[72] A. W. Musumeci, D. J. Gosztola, T. L. Schiller, N. M. Dimitrijević, V. Mujica, D. J. Martin, and T. Rajh, "Sers of semiconducting nanoparticles (tio(2) hybrid composites).," *Journal of the American Chemical Society*, vol. 131 17, pp. 6040–1, 2009.

[73] X. Du, L. Zhao, X. He, H. Chen, W. Li, and W. Fang, "Tio 2 hierarchical pores/nanorod arrays composite film as photoanode for quantum dot-sensitized solar cells," 2019.

[74] U. Guler, V. M. Shalaev, and A. Boltasseva, "Nanoparticle plasmonics: going practical with transition metal nitrides," *Materials Today*, vol. 18, pp. 227–237, 2015.

[75] G. V. Naik, J. Kim, and A. Boltasseva, "Oxides and nitrides as alternative plasmonic materials in the optical range [invited]," *Optical Materials Express*, vol. 1, pp. 1090–1099, 2011.

[76] A. Agrawal, R. W. Johns, and D. J. Milliron, "Control of localized surface plasmon resonances in metal oxide nanocrystals," *Annual Review of Materials Research*, vol. 47, pp. 1–31, 2017.

[77] X. Ye, J. Fei, B. T. Diroll, T. Paik, and C. B. Murray, "Expanding the spectral tunability of plasmonic resonances in doped metal-oxide nanocrystals through cooperative cation-anion codoping.," *Journal of the American Chemical Society*, vol. 136 33, pp. 11680–6, 2014.

[78] W. van der Stam, S. Gradmann, T. Altantzis, X. Ke, M. Baldus, S. Bals, and C. de Mello Donegá, "Shape control of colloidal cu2–xs polyhedral nanocrystals by tuning the nucleation rates," *Chemistry of Materials*, vol. 28, pp. 6705 – 6715, 2016.

[79] I. Kriegel, C. yang Jiang, J. Rodríguez-Fernández, R. D. Schaller, D. V. Talapin, E. da Como, and J. Feldmann, "Tuning the excitonic and plasmonic properties of copper chalcogenide nanocrystals.," *Journal of the American Chemical Society*, vol. 134 3, pp. 1583–90, 2012.

[80] L. Wang, C. Clavero, K. Yang, E. Radue, M. T. Simons, I. Novikova, and R. A. Lukaszew, "Bulk and surface plasmon polariton excitation in ruo2 for low-loss plasmonic applications in nir.," *Optics express*, vol. 20 8, pp. 8618–28, 2012.

[81] G. Sun, N. Li, D. Wang, G. Xu, X. Zhang, H. Gong, D. Li, Y. Li, H. Pang, M. Gao, and X. Liang, "A novel 3d hierarchical plasmonic functional cu@co3o4@ag array as intelligent sers sensing platform with trace droplet rapid detection ability for pesticide residue detection on fruits and vegetables," *Nanomaterials*, vol. 11, 2021.

[82] J. Rathod, S. S. B. Moram, B. Chandu, P. H. Albrycht, and V. R. Soma, "Single-step fabrication of hybrid germanium-gold/silver nanoentities by femtosecond laser ablation and applications in sers-based sensing," *Nanotechnology*, vol. 34, 2023.

[83] A. Nemilentsau, T. Low, and G. W. Hanson, "Anisotropic 2d materials for tunable hyperbolic plasmonics.," *Physical review letters*, vol. 116 6, p. 066804, 2015.

[84] J. S. DuChene, G. Tagliabue, A. J. Welch, W. Cheng, and H. A. Atwater, "Hot hole collection and photoelectrochemical co2 reduction with plasmonic au/p-gan photocathodes.," *Nano letters*, vol. 18 4, pp. 2545–2550, 2018.

[85] J. S. DuChene, G. Tagliabue, A. J. Welch, X. Li, W. Cheng, and H. A. Atwater, "Optical excitation of a nanoparticle cu/p-nio photocathode improves reaction selectivity for co2 reduction in aqueous electrolytes.," *Nano letters*, 2020.

[86] C. Krafft and J. Popp, "4.13 – raman-based technologies for biomedical diagnostics," 2014.

[87] J. B. Razvan Stoian, *Ultrafast Laser Nanostructuring: The Pursuit of Extreme Scales*. 2023.

[88] L. B. He, Y. L. Wang, X. Xie, M. Han, F. Q. Song, B. J. Wang, W. L. Cheng, H. X. Xu, and L. T. Sun, "Systematic investigation of the sers efficiency and sers hotspots in gas-phase deposited ag nanoparticle assemblies.," *Physical chemistry chemical physics : PCCP*, vol. 19 7, pp. 5091–5101, 2017.

[89] Y. Huang, Q. Zhou, M. Hou, L. Ma, and Z. Zhang, "Nanogap effects on near- and far-field plasmonic behaviors of metallic nanoparticle dimers.," *Physical chemistry chemical physics : PCCP*, vol. 17 43, pp. 29293–8, 2015.

[90] S. Wang, B. Sun, H. Jiang, Y. Jin, J. Feng, F. An, H. Wang, and W. Xu, "Facile and robust fabrication of hierarchical au nanorods/ag nanowire sers substrates for the sensitive detection of dyes and pesticides.," *Analytical methods : advancing methods and applications*, 2022.

[91] X.-B. Huang, S.-H. Wu, H. Hu, and J. jun Sun, "Aunanostar@4-mba@au core-shell nanostructure coupled with exonuclease iii-assisted cycling amplification for ultrasensitive sers detection of ochratoxin a.," *ACS sensors*, 2020.

[92] Y. Ran, P. Strobbia, V. Cupil-Garcia, and T. Vo-Dinh, "Fiber-optrode sers probes using plasmonic silver-coated gold nanostars," *Sensors and Actuators B: Chemical*, 2019.

[93] P. Wang, M. Xia, O. Liang, K. Sun, A. F. Cipriano, T. Schroeder, H. H. Liu, and Y. Xie, "Label-free sers selective detection of dopamine and serotonin using graphene-au nanopyramid heterostructure.," *Analytical chemistry*, vol. 87 20, pp. 10255–61, 2015.

[94] K. Tsui, X. Li, J. K. H. Tsoi, S.-F. Leung, T. Lei, W. Y. Chak, C. Zhang, J. Chen, G. S.-P. Cheung, and Z. Fan, "Low-cost, flexible, disinfectant-free and regular-array three-dimensional nanopyramid antibacterial films for clinical applications.," *Nanoscale*, vol. 10 22, pp. 10436–10442, 2018.

[95] H. Q. Wang, K. Li, C. Xu, S. Xu, and G. Li, "Large-scale solvothermal synthesis of ag nanocubes with high sers activity," *Journal of Alloys and Compounds*, 2019.

[96] L. Liu, W. Yizhi, N. Yin, H. Zhang, and H. Ma, "Silver nanocubes with high sers performance," *Journal of Quantitative Spectroscopy & Radiative Transfer*, vol. 240, p. 106682, 2020.

[97] C. Kuttner, M. Mayer, M. Dulle, A. Moscoso, J. M. López-Romero, S. Förster, A. Fery, J. Pérez-Juste, and R. Contreras-Cáceres, "Seeded growth synthesis of gold nanotriangles: Size control, saxs analysis, and sers performance.," *ACS applied materials & interfaces*, vol. 10 13, pp. 11152–11163, 2018.

[98] C. Wu, E. Z. Chen, and J. Wei, "Surface enhanced raman spectroscopy of rhodamine 6g on agglomerates of different-sized silver truncated nanotriangles," *Colloids and Surfaces A: Physicochemical and Engineering Aspects*, vol. 506, pp. 450–456, 2016.

[99] X. Geng, W. Leng, N. A. Carter, P. J. Vikesland, and T. Z. Grove, "Protein-aided formation of triangular silver nanoprisms with enhanced sers performance.," *Journal of materials chemistry. B*, vol. 4 23, pp. 4182–4190, 2016.

[100] S. Roy, C. M. Ajmal, S. Baik, and J. Kim, "Silver nanoflowers for single-particle sers with 10 pm sensitivity," *Nanotechnology*, vol. 28, 2017.

[101] V. Kariuki, J. C. Hoffmeier, I. Yazgan, and O. A. Sadik, "Seedless synthesis and sers characterization of multi-branched gold nanoflowers using water soluble polymers.," *Nanoscale*, vol. 9 24, pp. 8330–8340, 2017.

[102] H. Chen, M.-H. Lin, C.-Y. Wang, Y.-M. Chang, and S. Gwo, "Large-scale hot spot engineering for quantitative sers at the single-molecule scale.," *Journal of the American Chemical Society*, vol. 137 42, pp. 13698–705, 2015.

[103] W. Zhang, X. liang Qiao, and J. Chen, "Synthesis of silver nanoparticles—effects of concerned parameters in water/oil microemulsion," *Materials Science and Engineering B-advanced Functional Solid-state Materials*, vol. 142, pp. 1–15, 2007.

[104] H. Chiba, H. Suzuki, and M. Futamata, "Highly sensitive raman spectroscopy using a gap mode plasmon under an attenuated total reflection geometry," *Vibrational Spectroscopy*, vol. 73, pp. 19–23, 2014.

[105] J. Yang, I.-J. Hwang, M. G. Cha, H.-I. Kim, D. Yim, D. H. Jeong, Y.-S. Lee, and J. Kim, "Reaction kinetics-mediated control over silver nanogap shells as surface-enhanced raman scattering nanoprobes for detection of alzheimer's disease biomarkers.," *Small*, vol. 15 19, p. e1900613, 2019.

[106] X. Sun and H. Li, "A review: Nanofabrication of surface-enhanced raman spectroscopy (sers) substrates," *Current Nanoscience*, vol. 12, pp. 175–183, 2016.

[107] S. O. Martínez-Chapa, A. Salazar, and M. J. Madou, "Two-photon polymerization as a component of desktop-integrated manufacturing platforms," *Three-Dimensional Microfabrication Using Two-Photon Polymerization*, 2020.

[108] K. Sivashanmugan, J. D. Liao, J. W. You, and C.-L. Wu, "Focused-ion-beam-fabricated au/ag multilayered nanorod array as sers-active substrate for virus strain detection," *Sensors and Actuators B-chemical*, vol. 181, pp. 361–367, 2013.

[109] Y. Mandelbaum, R. Mottes, Z. Zalevsky, D. Zitoun, and A. Karsenty, "Design of surface enhanced raman scattering (sers) nanosensor array," *Sensors (Basel, Switzerland)*, vol. 20, 2020.

[110] H. Wang, G. M. Laws, S. Milicic, P. M. Boland, A. Handugan, M. Pratt, T. C. Eschrich, S. Myhajlenko, J. A. Allgair, and B. D. Bunday, "Low temperature zep-520a development process for enhanced critical dimension realization in reactive ion etch etched polysilicon," *Journal of Vacuum Science & Technology B*, vol. 25, pp. 102–105, 2007.

[111] H. Ahmed, M. Wu, and M. Stepanova, "Fabrication of plasmonic au nanostructures on dielectric supports using 10 kev electron beam lithography and tests for sers biodetection," *Journal of Vacuum Science & Technology B*, 2023.

[112] A. Das, U. Pant, C. Cao, R. S. Moirangthem, and H. B. Kamble, "Fabrication of plasmonic nanopyramidal array as flexible sers substrate for biosensing application," *Nano Research*, vol. 16, pp. 1132–1140, 2022.

[113] R. A. Álvarez-Puebla, B. Cui, J. P. Bravo-Vasquez, T. Veres, and H. Fenniri, "Nanoimprinted sers-active substrates with tunable surface plasmon resonances," *Journal of Physical Chemistry C*, vol. 111, pp. 6720–6723, 2007.

[114] H. Kang, S. Cho, J. Ryu, J. Choi, H. Ahn, H. Joo, and H. Jung, "Multiarray nanopattern electronic nose (e-nose) by high-resolution top-down nanolithography," *Advanced Functional Materials*, vol. 30, 2020.

[115] Q. Zhang, Y. H. Lee, I. Y. Phang, C. K. Lee, and X. Y. Ling, "Hierarchical 3d sers substrates fabricated by integrating photolithographic microstructures and self-assembly of silver nanoparticles.," *Small*, vol. 10 13, pp. 2703–11, 2014.

[116] S. Luo, K. Sivashanmugan, J. D. Liao, C.-K. Yao, and H. Peng, "Nanofabricated sers-active substrates for single-molecule to virus detection in vitro: a review.," *Biosensors & bioelectronics*, vol. 61, pp. 232–40, 2014.

[117] C. S. S. R. Kumar, "Raman spectroscopy for nanomaterials characterization," *Raman Spectroscopy for Nanomaterials Characterization*, 2012.

[118] X. Yang, N. Ileri, C. C. Larson, T. C. Carlson, J. A. Britten, A. S. Chang, C. Gu, and T. C. Bond, "Nanopillar array on a fiber facet for highly sensitive surface-enhanced raman scattering.," *Optics express*, vol. 20 22, pp. 24819–26, 2012.

[119] S. Kim, C. Mun, D. geun Choi, H. S. Jung, D.-H. Kim, S. Kim, and S. Park, "Quasi-3d plasmonic nanowell array for molecular enrichment and sers-based detection," *Nanomaterials*, vol. 10, 2020.

[120] X. Huang, Y. Liu, J. Barr, J. Song, Z. He, Y. Wang, Z. Nie, Y. Xiong, and X. Chen, "Controllable self-assembled plasmonic vesicle-based three-dimensional sers platform for picomolar detection of hydrophobic contaminants.," *Nanoscale*, vol. 10 27, pp. 13202–13211, 2018.

[121] J. C. Hulteen and R. P. V. Duyne, "Nanosphere lithography: A materials general fabrication process for periodic particle array surfaces," *Journal of Vacuum Science and Technology*, vol. 13, pp. 1553–1558, 1995.

[122] S. Luo, A. Mancini, E. C. Lian, W. Xu, R. Berté, and Y. Li, "Large area patterning of highly reproducible and sensitive sers sensors based on 10-nm annular gap arrays," *Nanomaterials*, vol. 12, 2022.

[123] S. Spaziani, G. Quero, S. Managò, G. Zito, D. Terracciano, P. E. Macchia, F. Galeotti, M. Pisco, A. C. D. Luca, and A. Cusano, "Sers assisted sandwich immunoassay platforms for ultrasensitive and selective detection of human thyroglobulin.," *Biosensors & bioelectronics*, p. 115322, 2023.

[124] G. Quero, G. Zito, S. Managò, F. Galeotti, M. Pisco, A. C. D. Luca, and A. Cusano, "Nanosphere lithography on fiber: Towards engineered lab-on-fiber sers optrodes," *Sensors (Basel, Switzerland)*, vol. 18, 2018.

[125] X. Zhang, X. Xiao, Z. Dai, W. Wu, X. Zhang, L. Fu, and C. Jiang, "Ultrasensitive sers performance in 3d "sunflower-like" nanoarrays decorated with ag nanoparticles.," *Nanoscale*, vol. 9 9, pp. 3114–3120, 2017.

[126] X. Zhao, J. Wen, M. Zhang, D. Wang, Y. Wang, L. Chen, Y. Zhang, J. Yang, and Y. Du, "Design of hybrid nanostructural arrays to manipulate sers-active substrates by nanosphere lithography.," *ACS applied materials & interfaces*, vol. 9 8, pp. 7710–7716, 2017.

[127] X. Xu, Q. Yang, N. Wattanatorn, C. Zhao, N. Chiang, S. J. Jonas, and P. S. Weiss, "Multiple-patterning nanosphere lithography for fabricating periodic three-dimensional hierarchical nanostructures.," *ACS nano*, vol. 11 10, pp. 10384–10391, 2017.

[128] K. S. Lee, Z. Landry, F. C. Pereira, M. Wagner, D. Berry, W. E. Huang, G. T. Taylor, J. Kneipp, J. Popp, M. Zhang, J. Cheng, and R. Stocker, "Raman microspectroscopy for microbiology," *Nature Reviews Methods Primers*, vol. 1, 2021.

[129] C.-S. Ho, N. Jean, C. A. Hogan, L. Blackmon, S. S. Jeffrey, M. Holodniy, N. Banaei, A. A. E. Saleh, S. Ermon, and J. A. Dionne, "Rapid identification of pathogenic bacteria using raman spectroscopy and deep learning," *Nature Communications*, vol. 10, 2019.

[130] K. Liu, Q. Zhao, B. Li, and X. Zhao, "Raman spectroscopy: A novel technology for gastric cancer diagnosis," *Frontiers in Bioengineering and Biotechnology*, vol. 10, 2022.

[131] L. Kassa-Baghdouche and E. Cassan, "Mid-infrared refractive index sensing using optimized slotted photonic crystal waveguides," *Photonics and Nanostructures: Fundamentals and Applications*, vol. 28, pp. 32–36, 2018.

[132] L. Kassa-Baghdouche and E. Cassan, "Sensitivity analysis of ring-shaped slotted photonic crystal waveguides for mid-infrared refractive index sensing," *Optical and Quantum Electronics*, vol. 51, 2019.

[133] L. Guerrini, E. García-Rico, A. O'Loghlen, V. Giannini, and R. A. Álvarez-Puebla, "Surface-enhanced raman scattering (sers) spectroscopy for sensing and characterization of exosomes in cancer diagnosis," *Cancers*, vol. 13, 2021.

[134] J. Zhang, S. Chen, T. Gong, X. lei Zhang, and Y. Zhu, "Tapered fiber probe modified by ag nanoparticles for sers detection," *Plasmonics*, vol. 11, pp. 743–751, 2016.

[135] T. Gong, Y. Cui, D. W. Goh, K. K. Voon, P. P. Shum, G. Humbert, J.-L. Auguste, X. Q. Dinh, K. Yong, and M. Olivo, "Highly sensitive sers detection and quantification of sialic acid on single cell using photonic-crystal fiber with gold nanoparticles.," *Biosensors & bioelectronics*, vol. 64, pp. 227–33, 2015.

[136] D. Gao, X. Yang, P. Teng, Z. Liu, J. Yang, D. Kong, J. Zhang, M. Luo, Z. Li, F. Tian, and L. Yuan, "Optofluidic in-fiber integrated surface-enhanced raman spectroscopy detection based on a hollow optical fiber with a suspended core.," *Optics letters*, vol. 44 21, pp. 5173–5176, 2019.

[137] S. E. J. Bell, G. Charron, E. Cortés, J. Kneipp, M. L. de la Chapelle, J. Langer, M. Procházka, V. Tran, and S. Schlücker, "Towards reliable and quantitative surface-enhanced raman scattering (sers): From key parameters to good analytical practice," *Angewandte Chemie (International Ed. in English)*, vol. 59, pp. 5454 – 5462, 2020.

[138] J. Wang, W. Ahmad, M. M. Hassan, M. Zareef, A. Viswadevarayalu, M. Arslan, H. Li, and Q. Chen, "Landing microextraction sediment phase onto surface enhanced raman scattering to enhance sensitivity and selectivity for chromium speciation in food and environmental samples.," *Food chemistry*, vol. 323, p. 126812, 2020.

[139] S. L. Kitaw, H. F. Darge, K. D. Addisu, D. Thankachan, Y. W. Ahmed, Y. S. Chen, H. Tegenu, A. Candra, T.-Y. Wu, Y. Gou, and H. Tsai, "Fabrication of ag nanostar and pei-based sers substrate for sensitive and rapid detection of so2: Application for detection of sulfite residues in beer.," *Spectrochimica acta. Part A, Molecular and biomolecular spectroscopy*, vol. 302, p. 123113, 2023.

[140] Q. Tao, S. Li, C. yu Ma, K. Liu, and Q.-Y. Zhang, "A highly sensitive and recyclable sers substrate based on ag-nanoparticle-decorated zno nanoflowers in ordered arrays.," *Dalton transactions*, vol. 44 7, pp. 3447–53, 2015.

[141] A. Lucotti and G. Zerbi, "Fiber-optic sers sensor with optimized geometry," *Sensors and Actuators B-chemical*, vol. 121, pp. 356–364, 2007.

[142] A. Foti, C. D'Andrea, F. Bonaccorso, M. Lanza, G. Calogero, E. Messina, O. M. Maragò, B. Fazio, and P. G. Gucciardi, "A shape-engineered surface-enhanced raman scattering optical fiber sensor working from the visible to the near-infrared," *Plasmonics*, vol. 8, pp. 13–23, 2013.

[143] Y. Qiu, C. Kuang, X. Liu, and L. Tang, "Single-molecule surface-enhanced raman spectroscopy," *Sensors (Basel, Switzerland)*, vol. 22, 2022.

[144] L. Siksou, P. Rostaing, J. P. Lechaire, T. Boudier, T. Ohtsuka, A. Fejtová, H.-T. Kao, P. Greengard, E. D. Gundelfinger, A. Triller, and S. Marty, "Three-dimensional architecture of presynaptic terminal cytomatrix," *The Journal of Neuroscience*, vol. 27, pp. 6868 – 6877, 2007.

[145] C. H. Viets and W. Hill, "Comparison of fibre-optic sers sensors with differently prepared tips," *Sensors and Actuators B-chemical*, vol. 51, pp. 92–99, 1998.

[146] M. Principe, M. Consales, A. Micco, A. Crescitelli, G. Castaldi, E. Esposito, V. L. Ferrara, A. Cutolo, V. Galdi, and A. Cusano, "Optical fiber meta-tips," *Light, Science & Applications*, vol. 6, 2016.

[147] Y. Lin, Y. Zou, Y. Mo, J. Guo, and R. G. Lindquist, "E-beam patterned gold nanodot arrays on optical fiber tips for localized surface plasmon resonance biochemical sensing," *Sensors (Basel, Switzerland)*, vol. 10, pp. 9397 – 9406, 2010.

[148] Y. Liu, Z. Huang, F. Zhou, X. Lei, B. Yao, G. Meng, and Q. Mao, "Highly sensitive fibre surface-enhanced raman scattering probes fabricated using laser-induced self-assembly in a meniscus.," *Nanoscale*, vol. 8 20, pp. 10607–14, 2016.

[149] J. Li, H. Yan, X. Tan, Z. Lu, and H. Han, "Cauliflower-inspired 3d sers substrate for multiple mycotoxins detection.," *Analytical chemistry*, vol. 91 6, pp. 3885–3892, 2019.

[150] C. Wang, C. Wang, X. Wang, K. Wang, Y. Zhu, Z. Rong, W. Wang, R. Xiao, and S. Wang, "Magnetic sers strip for sensitive and simultaneous detection of respiratory viruses.," *ACS applied materials & interfaces*, vol. 11 21, pp. 19495–19505, 2019.

[151] P. A. Mosier-Boss, "Review of sers substrates for chemical sensing," *Nanomaterials*, vol. 7, 2017.

[152] X. Zhang, K. Zhang, H. von Bredow, C. J. Metting, G. Atanasoff, R. M. Briber, and O. Rabin, "Remote chemical sensing by sers with self-assembly plasmonic nanoparticle arrays on a fiber," 2022.

[153] G. Quero, G. Zito, S. Managò, F. Galeotti, M. Pisco, A. C. D. Luca, and A. Cusano, "Lab-on-fiber sers substrates for biomolecular recognition," 2019.

[154] Y. Long, H. Li, W. Wang, X. Yang, and Z. Liu, "Ultrasensitive detection of cr(vi) using a novel sers optical fiber probe modified by dual-functional methimazole," *Journal of Alloys and Compounds*, 2022.

[155] T. B. Pham, T. H. C. Hoang, V. C. Nguyen, D. C. Vu, H. Bui, and V. H. Pham, "Improved versatile sers spheroid end-facet optical fiber substrate based on silver nano-dendrites directly planted with gold nanoparticles using dual-laser assisted for pesticides detection," *Optical Materials*, 2022.

[156] X. Wang, Y. Wu, X. Wen, J. Zhu, X. Bai, Y. Qi, and H. Yang, "Surface plasmons and sers application of au nanodisk array and au thin film composite structure," *Optical and Quantum Electronics*, vol. 52, pp. 1–11, 2020.

[157] T. Li, Z. L. Yu, Z. Wang, Y. Zhu, and J. Zhang, "Optimized tapered fiber decorated by ag nanoparticles for raman measurement with high sensitivity," *Sensors (Basel, Switzerland)*, vol. 21, 2021.

[158] P. C. Lee and D. C. Meisel, "Adsorption and surface-enhanced raman of dyes on silver and gold sols," *The Journal of Physical Chemistry*, vol. 86, pp. 3391–3395, 1982.

[159] A. Kohut, A. Kéri, V. Horváth, J. Kopniczky, T. Ajtai, B. Hopp, G. Galbács, and Z. Geretovszky, "Facile and versatile substrate fabrication for surface enhanced raman spectroscopy using spark discharge generation of au/ag nanoparticles," *Applied Surface Science*, 2020.

[160] Q. Geng, D. Wang, P. Chen, and S. C. Chen, "Ultrafast multi-focus 3-d nano-fabrication based on two-photon polymerization," *Nature Communications*, vol. 10, 2019.

[161] A. Zhang, Z. Wang, H. Ouyang, W. Lyu, J. Sun, Y. Cheng, and B. Fu, "Recent progress of two-dimensional materials for ultrafast photonics," *Nanomaterials*, vol. 11, 2021.

[162] E. Avci, M. Grammatikopoulou, and G.-Z. Yang, "Laser-printing and 3d optical-control of untethered microrobots," *Advanced Optical Materials*, vol. 5, 2017.

[163] J. Williams, H. Chandrahalim, J. S. Suelzer, and N. G. Usechak, "Two-photon nanomachining of a micromechanically enhanced optical cavity sensor on an optical fiber tip," *Advanced Photonics Research*, vol. 3, 2022.

[164] *COMSOL Multiphysics v. 6.1.*

[165] P. B. Johnson and R. W. Christy, "Optical constants of the noble metals," *Physical Review B*, vol. 6, pp. 4370–4379, 1972.

[166] Z. Zhang, G. Yi, P. Li, X. Zhang, Z. Wan, X. Wang, C. Zhang, and Y. Zhang, "Recent advances in binary colloidal crystals for photonics and porous material fabrication.," *The journal of physical chemistry. B*, 2021.

[167] F. S. Diba, A. Boden, H. Thissen, M. Bhave, P. Kingshott, and P.-Y. Wang, "Binary colloidal crystals (bccs): Interactions, fabrication, and applications.," *Advances in colloid and interface science*, vol. 261, pp. 102–127, 2018.

[168] Z. Dai, Y. Li, G. Duan, L. Jia, and W. Cai, "Phase diagram, design of monolayer binary colloidal crystals, and their fabrication based on ethanol-assisted self-assembly at the air/water interface.," *ACS nano*, vol. 6 8, pp. 6706–16, 2012.

[169] E. J. Smythe, M. D. Dickey, J. Bao, G. M. Whitesides, and F. Capasso, "Optical antenna arrays on a fiber facet for in situ surface-enhanced raman scattering detection.," *Nano letters*, vol. 9 3, pp. 1132–8, 2009.

[170] E. C. L. Ru, E. J. Blackie, M. Meyer, and P. G. Etchegoin, "Surface enhanced raman scattering enhancement factors: A comprehensive study," *Journal of Physical Chemistry C*, vol. 111, pp. 13794–13803, 2007.

[171] F. Benz, C. Tserkezis, L. O. Herrmann, B. de Nijs, A. Sanders, D. O. Sigle, L. Pukenas, S. Evans, J. Aizpurua, and J. J. Baumberg, "Nanooptics of molecular-shunted plasmonic nanojunctions," *Nano Letters*, vol. 15, pp. 669 – 674, 2014.

[172] Y. Yokota, K. Ueno, and H. Misawa, "Essential nanogap effects on surface-enhanced raman scattering signals from closely spaced gold nanoparticles.," *Chemical communications*, vol. 47 12, pp. 3505–7, 2011.

[173] C. Zhang, S. Chen, Z. Jiang, Z. Shi, J. Wang, and L. Du, "Highly sensitive and reproducible sers substrates based on ordered micropyramid array and silver nanoparticles.," *ACS applied materials & interfaces*, 2021.

[174] P. Biagioni, D. Brida, M. Ortolani, and D. J. Paul, "Integrating mid-ir plasmonics with cmos sensing devices," *Spie Newsroom*, 2016.

Author's publications

1. M. A. Cutolo , F. Galeotti, S. Spaziani, G. Quero, V. Calcagno, A. Micco, A. Irace, G. Breglio, M. Pisco, A. Cusano. Self Assembled Hierarchical nanostructures: Towards Engineered SERS active platform. Under submission

2. Sofia Principe, Martino Giaquinto, Alberto Micco, Maria Alessandra Cutolo, Michele Riccio, Giovanni Breglio, Andrea Irace, Armando Ricciardi, Andrea Cusano, Thermo-plasmonic lab-on-fiber optrodes, Optics & Laser Technology,Volume 132, 2020, 106502, ISSN 0030-3992. https://doi.org/10.1016/j.optlastec.2020.106502.

3. Cutolo, A., Carotenuto, A.R., Cutolo, M.A. et al. Ultrasound waves in tumors via needle irradiation for precise medicine. Sci Rep 12, 6513 (2022). https://doi.org/10.1038/s41598-022-10407-5

4. Maria Alessandra Cutolo, Giovanni Breglio, (INVITED)Interferometric Fabry-Perot sensors for ultrasound detection on the tip of an optical fiber, Results in Optics, Volume 6, 2022, 100209, ISSN 2666-9501, https://doi.org/10.1016/j.rio.2021.100209.

5. Cutolo, M.A., Cafiero, C., Califano, L. et al. Feasibility analysis of an ultrasound on line diagnostic approach for oral and bone surgery. Sci Rep 12, 905 (2022). https://doi.org/10.1038/s41598-022-04857-0

6. Barbara Rossi, Maria Alessandra Cutolo, Martino Giaquinto, Advanced Lab-on-Tip ultrasound detectors: A numerical analysis, Results in Optics, Volume 9, 2022, 100312, ISSN 2666-9501. https://doi.org/10.1016/j.rio.2022.100312.

7. Cutolo A, Bernini R, Berruti GM, Breglio G, Bruno FA, Buontempo S, Catalano E, Consales M, Coscetta A, Cusano A, et al. Innovative Photonic

Sensors for Safety and Security, Part II: Aerospace and Submarine Applications. Sensors. 2023; 23(5):2417. https://doi.org/10.3390/s23052417

8. Minardo, A.; Bernini, R.; Berruti, G.M.; Breglio, G.; Bruno, F.A.; Buontempo, S.; Campopiano, S.; Catalano, E.; Consales, M.; Coscetta, A.; et al. Innovative Photonic Sensors for Safety and Security, Part I: Fundamentals, Infrastructural and Ground Transportations. Sensors 2023, 23, 2558. https://doi.org/10.3390/s23052558

9. Breglio, G.; Bernini, R.; Berruti, G.M.; Bruno, F.A.; Buontempo, S.; Campopiano, S.; Catalano, E.; Consales, M.; Coscetta, A.; Cutolo, A.; et al. Innovative Photonic Sensors for Safety and Security, Part III: Environment, Agriculture and Soil Monitoring. Sensors 2023, 23, 3187. https://doi.org/10.3390/s23063187